Combined Electrostatic/Electromagnetic MEMS Actuators

by

Ayman Alneamy

A thesis
presented to the University of Waterloo
in fulfillment of the
thesis requirement for the degree of
Master of Applied Science
in
Systems Design Engineering

Waterloo, Ontario, Canada, 2016

© Ayman Alneamy 2016

I hereby declare that I am the sole author of this thesis. This is a true copy of the thesis, including any required final revisions, as accepted by my examiners.

I understand that my thesis may be made electronically available to the public.

Abstract

In this work, one and two degrees of freedom (DOF) lumped mass models of Micro-Electro-Mechanical System (MEMS) actuators are introduced, investigated, and compared to experimental results. A one degree of freedom system representing the actuators out-of-plane bending motion under the electrostatic excitation is demonstrated. The capacitive gap between the movable plate and stationary electrode decreases when the microplate inclination angle is accounted for in the model.

We investigate experimentally the primary, superharmonic of order two, and subharmonic of order one-half resonances of an electrostatic MEMS actuator under direct excitation. We identify the parameters of a 1-DOF generalized Duffing oscillator, model that represents it. The experiments were conducted in soft vacuum in order to reduce squeeze-film damping and the actuator response was measured optically using a laser vibrometer. The predictions of the identified model were found to be in close agreement with the experimental results. We also identified the power level of process (actuation voltage) and measurement noise.

A one DOF model of the actuator's torsional motion under the electrostatic torque is also introduced. It was found that utilizing electrostatic actuation in torsional motion is not effective. The maximum angle obtained was 0.04 degrees at high voltage. Finally, a novel two DOF model of the MEMS actuator's torsion and bending under electrostatic and electromagnetic excitation was demonstrated analytically and compared to experimental results. Torsional motions were driven by a torque arising from a Lorentz force. It succeeded in generating a large torsion angle, 1 degree at 1.35 T magnetic field density, and a current of 3.3 mA.

Acknowledgements

All praises are due to Allah for providing me the guidance, strength, and patience to fulfill this thesis work and the MASc degree successfully.

I would like to express my deep grateful to my supervisors at the University of Waterloo, Prof. Eihab Abdel-Rahman and Prof. Glenn Heppler for the true guidance, inspiration, and endless support throughout my master studies. I really consider my relationship with my supervisors as one of the most achievements contribution while in Waterloo. In fact, no words can truly express my gratitude to my supervisors.

I would like to thank members of the examining committee, namely, Prof. Mustafa Yavuz and Prof. Nasser Azad from the University of Waterloo who have taken time to review my thesis and their constructive comments, which helped me in improving the final presentation of this work.

I am especially thankful to Dr. Mahmoud Khater and Dr. Sangtak Park. They provided detailed comments and suggestions to improve my thesis. A special thanks to Dr. Ayman Nada for having several discussions with me, especially during my last year; his suggestions have led me to unexpected detections.

I am very grateful to my colleagues Ridha Almikhlafi, Abdullatif Alwasel, Majed Algamdi, Mohammed Rasit and Alaa-Aldin for their cooperations and comments through this work.

I would also like to thank Mr. Ali Yagup, Mr. Asem Mokali, Mr. Zailay Mohammed, Mr. Ahmed Mokali, Mr. Ali Mokali, Mr. Ahmed Gharama, Mr. Ali Qaseem and Mr. Ibrahim Qaseem.

Finally, I have to express my very profound gratitude to my parents for providing me with unconditional support and continuous encouragement throughout my years of study and through the process of researching and writing this thesis. Moreover, I would like to thank my lovely wife, Hadel, for her patience, encouragement and understanding during my master studies as well as my lovely daughter Hutaf. Also, a big thank goes to my brothers and sisters.

This work was financially supported by Jazan University, Saudi Arabia.

Dedication

To my parents (Mohammed & Lila)

To my brothers (Mosa & Abdul-Majed)

To my sisters (Sara, Somaia, Seham, Samah & Solaf)

To my beloved wife (Hadel)

To my beloved daughter (Hutaf)

with respect and love

Table of Contents

List of Tables viii

List of Figures ix

Nomenclature xiii

1 Introduction 1

1.1 Motivation 2

1.2 Thesis Organization 2

1.3 Thesis's Contribution 3

1.3.1 Journal papers 3

1.3.2 Conference papers 3

2 Literature Review 4

2.1 Microsensing 5

2.2 Microactuation 5

3 Electrostatic MEMS Actuator 15

3.1 The Actuator 15

3.2 Analytical Model 16

3.2.1 Lumped Elements 20

3.2.2 Equation of Motion 22

3.3 Static Analysis 24
3.4 Eigenvalue Analysis 26
3.5 Dynamic Analysis 29

4 Parameter Identification of the Electrostatic Actuator 32

4.1 Analytical Model 32
4.2 Primary Resonance 36
4.3 Superharmonic Excitation 42
4.4 Subharmonic Excitation 46
4.5 Activation of Subharmonic Resonance 49

5 Electrostatic/Electromagnetic MEMS Actuator 56

5.1 The Actuator 56
5.1.1 Actuator Operation Process 57
5.2 Analytical Model 59
5.3 Static Analysis 65
5.4 Eigenvalue Analysis 67
5.5 Dynamic Analysis 70
5.6 Actuator Calibration 71

6 Conclusions and Future Work 75

6.1 Conclusions 75
6.2 Future Work 77

Bibliography 78

List of Tables

2.1 Comparison of Actuation Mechanisms in MEMS 14

3.1 Dimensions of the Actuator 16

3.2 Material Properties 17

3.3 Electrostatic Force Components 31

4.1 Subharmonic Forcing Levels and the Instability Region 53

5.1 Peak magnitudes of the model predicted and experimentally measured velocity for (a) $V_{dc} = 1\,\mathrm{V}$, (b) $V_{dc} = 2\,\mathrm{V}$, (c) $V_{dc} = 3\,\mathrm{V}$, (d) $V_{dc} = 4\,\mathrm{V}$, (e) $V_{dc} = 5\,\mathrm{V}$ and (f) $V_{dc} = 6\,\mathrm{V}$. 73

List of Figures

2.1 *A schematic drawing of an electrostatic actuator.* 6

2.2 *A schematic drawing of a parallel plate capacitor.* 7

2.3 *Equilibrium points of an electrostatic actuator lumped-mass model for three voltage values: (a) $V < V_{pin}$, (b) $V = V_{pin}$ and (c) $V > V_{pin}$.* 9

3.1 *A schematic drawing of the electrostatic actuator.* 16

3.2 *A schematic of a spring-mass-damper model.* 17

3.3 *A side view of the electrostatic actuator. (a) The initial position of the microplate, (b) the electrostatic force lumped as a point force at the center of the microplate and (c) the translated electrostatic force and end moment at the tip of the cantilever beam.* 18

3.4 *(a) A schematic drawing of a microplate in the initial position and (b) microplate position after the actuation voltage is applied.* 18

3.5 *A schematic drawing of the actuator deformation due to the electrostatic force. (a) inaccurate (flat microplate) model and (b) accurate (inclined microplate) model.* 19

3.6 *A schematic drawing of the microplate bending angle under the effect of the electrostatic force.* 19

3.7 *A schematic drawing of cantilever beams as (a) parallel springs and (b) an equivalent spring .* 20

3.8 *(a) A 3D scan of the actuator using white a white light profilometer and (b) a picture of the actuator.* 22

3.9 *Comsol setup using steps 1-4.* 25

3.10 *The meshing size element of the actuator.* 26

3.11 *Model predicted stable (solid blue line) and unstable (dashed red line) equilibria. Stable FEM predicted equilibria are marked with green ⋄ symbols.* 27

3.12 *(a) The first mode shape obtained from the FEM and (b) a comparison of the corresponding natural frequency results to the applied voltage that obtained from the lumped-mass model (red line) and FEM (blue ⋄ symbols).* 28

3.13 *The frequency-response curves of the actuator in the (a) absence and (b) presence of squeeze-film damping.* 29

3.14 *The frequency-response curves of the actuator in the (a) absence and (b) presence of squeeze-film damping.* 31

4.1 *The FFT of the actuator's velocity under thermal noise excitation and chamber pressure of* 53 *mTorr.* 34

4.2 *The first six mode shapes and natural frequencies of the actuator obtained from FEM.* 35

4.3 *Model predicted (solid red line) and experimental (blue ⋄) FFTs of the actuator velocity under primary resonance excitation* $f = 32.8\,kHz$. 37

4.4 *Model predicted time-histories of the: (a) displacement, (b) velocity and (c) corresponding phase portrait under primary resonance,* $f = 32.8\,kHz$. . . . 38

4.5 *(a) The experimental time-histories of the displacement (yellow line) and velocity (blue line) and (b) the corresponding phase portrait of the actuator captured from the oscilloscope under primary resonance,* $f = 32.8\,kHz$. . . 39

4.6 *FFT of the experimentally measured velocity at the primary resonance* $f = 32.8\,kHz$. 40

4.7 *The predicted frequency-response curve of the electrostatic actuator near primary resonance. Forward sweep in blue line and backward sweep red dashed line.* 41

4.8 *Model predicted (solid red line) and experimental (blue ⋄) FFTs of the actuator velocity under superharmonic resonance,* $f = 16.4\,kHz$. 42

4.9 *The model predicted time-histories of the: (a) displacement, (b) velocity and (c) corresponding phase portrait under superharmonic resonance,* $f = 16.4\,kHz$. 43

4.10 *(a) The experimental time-histories of the displacement (yellow line) and velocity (blue line) and (b) the corresponding phase portrait of the actuator captured from the oscilloscope under superharmonic resonance, $f = 16.4\,kHz$.* . . . 44

4.11 *FFT of the experimentally measured velocity at the superharmonic resonance $f = 16.4\,kHz$.* . . . 45

4.12 *The predicted frequency-response curve of the electrostatic actuator near superharmonic resonance. Forward sweep in blue line and backward sweep red dashed line.* . . . 46

4.13 *The model predicted (solid red line) and experimental (blue $\diamond$) FFTs of the actuator velocity under subharmonic resonance excitation $f = 65.6\,kHz$.* . . . 47

4.14 *The model predicted time-histories of the: (a) displacement , (b) velocity and (c) the corresponding phase portrait under subharmonic resonance, $f = 65.6\,kHz$.* . . . 48

4.15 *(a) The experimental time-histories of the displacement (yellow line) and velocity (blue line) and (b) the corresponding phase portrait of the actuator captured from the oscilloscope under subharmonic resonance, $f = 65.6\,kHz$.* 49

4.16 *FFT of the experimentally measured velocity at the subharmonic resonance $f = 65.6\,kHz$* . . . 50

4.17 *The predicted frequency-response curve of the electrostatic actuator near subharmonic resonance. Forward sweep in blue line and backward sweep red dashed line.* . . . 51

4.18 *The model predicted FFTs for $\Omega = 2\omega_{nb}$ and (a) 500 V_{dc} and 500 V_{ac}, (b) 542 V_{dc} and 400 V_{ac}, (c) 550 V_{dc} and 378 V_{ac}, (d) 558 V_{dc} and 353 V_{ac}, (e) 568 V_{dc} and 320 V_{ac} and (f) 580 V_{dc} and 270 V_{ac}.* . . . 52

4.19 *Model predicted frequency-response curves for the waveforms: (a) $V_{dc} = 500\,mV$ and $V_{ac} = 500\,mV$, (b) $V_{dc} = 542\,mV$ and $V_{ac} = 400\,mV$, (c) $V_{dc} = 550\,mV$ and $V_{ac} = 378\,mV$, (d) $V_{dc} = 558\,mV$ and $V_{ac} = 353\,mV$, (e) $V_{dc} = 568\,mV$ and $V_{ac} = 320\,mV$, and (f) $V_{dc} = 580\,mV$ and $V_{ac} = 270\,mV$.* . . . 54

4.20 *The relationship between the forcing amplitude and the size of the trivial solution instability region.* . . . 55

5.1 *A schematic diagram of the electrostatic/electromagnetic MEMS actuator.* 57

5.2 *A schematic of the actuation scheme of the electrostatic/electromagnetic actuator. The excitation current $\vec{i}(t)$ passes through the cantilever beams. An external magnetic field $\vec{B}$ crosses the current resulting in Lorentz force $\vec{F}_L$ acting on the beams.* . . . 58

5.3 *The dimensions of the combined electrostatic/electromagnetic actuator.* . . . 59

5.4 *The microplate in the intial position.* . . . 60

5.5 *The microplate in piston motion under equal voltages.* . . . 61

5.6 *The microplate deflection and rotation due to the electrostatic forces and electrostatic and electromagnetic torques.* . . . 61

5.7 *Model predicted (red line) and measured ($\diamond$ symbols) (a) static torsion angle β_s vs. actuation voltage V_{dc} and (b) static torsion angle β_s vs. magnetic field B.* . . . 66

5.8 *A comparison of the corresponding natural frequency results to the applied voltage that obtained from the lumped-mass model (red line) and FEM (blue $\diamond$ symbols).* . . . 68

5.9 *Comparison of the first torsional mode shape obtained by (a) FEM at 198 kHz and (b) experimentally at 182 kHz.* . . . 69

5.10 *The FFTs of the measured ($\diamond$ symbols) and the model predicted edge velocity at the edge (red line) in (a) the absence ($B = 0\,mT$) and (b) presence ($B = 27.8\,mT$) of an external magnetic field where $f = 182\,kHz$.* . . . 71

5.11 *(a) The electrostatic/electromagnetic actuator mounted inside the test chamber. (b) A vibrometer multi-scan grid showing point A where edge displacement and velocity are measured.* . . . 72

5.12 *The measured ($\diamond$ symbols) and the predicted (red lines) FFTs of point A displacement and velocity. The actuator is excited electrostatically by $V_{ac_1} = V_{ac_2} = 2.5\ V$, $V_{dc} = 0$ and electromagnetically by $i = 3.3\,mA$ and $B = 64\,mT$ at a frequency of $f = 182\,kHz$.* . . . 73

5.13 *The experimental and model predicted FFTs for $B = 64\,mT$, $i = 3.3\,mA$, $V_{ac_1} = V_{ac_2} = 2.5\ V$, and $f = 182\,kHz$. The bias voltage is set set (a) $V_{dc} = 1\ V$, (b) $V_{dc} = 2\ V$, (c) $V_{dc} = 3\ V$, (d) $V_{dc} = 4\ V$, (e) $V_{dc} = 5\ V$ and (f) $V_{dc} = 6\ V$.* . . . 74

List of Nomenclature

The following notations are used throughout the text and other notations are used at their relevant positions:

Q_e	Applied voltage
AMR	Anisotropic magneto resistance
L_b	Beam length
h_b	Beam thickness
b_b	Beam width
C	Capacitance
DOF	Degree of freedom
Q_e	Electrical charging
F_{es}	Electrostatic force
S_v	Electrical noise spectral density
FFT	Fast Fourier Transfer
d	Gap
S_m	Measurement noise spectral density
M	Moment
L_p	Plate length

h_p	Plate thickness
b_p	Plate width
U_c	Potential energy
V_{pin}	Pull in voltage
T	Time scaling

Chapter 1

Introduction

This thesis focuses on developing a new design and operation method for micro actuators that combines electrostatic and electromagnetic actuation. The static and dynamic behavior of electrostatic actuators and electromagnetic actuators have been investigated analytically and experimentally.

Electrostatic MEMS actuators are broadly classified into parallel plate or comb-finger drives. Recent research in Micro Electro Mechanical System (MEMS) technology has shown the advantages of using electrical excitation with mechanical structures. This new technology has enhanced the performance of many systems by replacing large electrical components with MEMS components. However, it has limitations that reduce the overall performance.

The electrostatic actuator under study shows a high resonance frequency and a large deformation under low excitation voltages in bending mode. However, it does not produce a large torsional angle under the same excitation force. Electromagnetic excitation caused by interaction between current flowing in the actuator and an external permanent magnet field, in addition to the electrostatic excitation, leads to a better performance in the torsional mode.

In this research, a simple technique is used to identify the parameters of a 1-DOF generalized Duffing oscillator. Also, it introduces a lumped mass model for a novel electrostatic/electromagnetic MEMS actuator. The results showed a significant change in the actuator performance.

A parallel plate microactuator was modeled, characterized, and tested experimentally under electrostatic excitation and combined electrostatic and electromagnetic excitation.

An analytical model was developed to predict the static and dynamic responses of the actuator. Experimental results were used to verify the accuracy of the model prediction.

1.1 Motivation

There are many advantages of using MEMS electrostatic actuators and MEMS electromagnetic actuators. However, electrostatic excitation has limitations resulting in the pull-in phenomenon which limits the displacement of the microstructure and leads to instability. Introducing electromagnetic excitation can increase the displacement range of the actuator and reduce the required actuation voltage. The main benefit of using electromagnetic forcing is to control the pull-in voltage and increase the displacement of the microstructure. These proposed actuators do not require special magnetic materials which may result in fabrication difficulties.

1.2 Thesis Organization

This thesis contains five chapters as follows:

Chapter 2 reviews the literature on MEMS technology, MEMS sensors and MEMS actuators. In particular, it details the actuation mechanisms used to excite theses devices. The static and dynamic behaviors of nonlinear electrostatic MEMS actuator are also described.

Chapter 3 presents a mathematical model of a parallel plate electrostatic MEMS actuator and a method to identify the actuator dimensions, material properties and quadratic and cubic nonlinearities. This analytical model is used to predict the static and dynamic responses of the actuator under different electrostatic excitation forces. In addition, we investigate the effect of squeeze-film damping on the dynamic response of the actuator.

Chapter 4 presents a mathematical model and a parameter identification technique of 1 DOF generalized Duffing oscillator.

Chapter 5 describes a novel combined MEMS actuator based on electrostatic/electromagnetic actuation. It introduces a lumped-mass model and experimental techniques that are utilized to investigate the static and dynamic responses of the actuator.

Finally, **Chapter 6** contains the conclusions of this work and a discussion of future work.

1.3 Thesis's Contribution

The main contributions of this thesis focus on developing mathematical models that compared to the experimental results which reported by Park [67] and Alghmadi [69]. Dr.Park did the experimental work of the generalized Duffing oscillator and invetegated the primary and secondary resonances of the actuator. Mr. Alghamdi did a deep experimental investigation on the electrostatic/electromagnetic actuator. The results of my thesis have been published in the following papers:

1.3.1 Journal papers

M. S. Al-Ghamdi, **A. M. Alneamy**, S. Park, B. Li, M. E. Khater, E. M. Abdel-Rahman, G. R. Heppler., & M. Yavuz. Nonlinear Parameter Identification of a Resonant Electrostatic MEMS Actuator. International Journal of Nonlinear Dynamics and Control, (In press).

1.3.2 Conference papers

A. M. Alneamy, Mahmoud Khater, Sangtak Park, Eihab Abdel-Rahman, & Glenn Heppler. Electrostatic versus Electromagnetic Micromirrors Actuation. International Congress of Theoretical and Applied Mechanics, Montreal, August (21-26) 2016, (Published).

Chapter 2

Literature Review

Micro Electro Mechanical Systems (MEMS) are widely known as miniaturized electro-mechanical devices and structures that are made using microfabrication techniques [1]. Dimensions associated with MEMS devices can vary from one micron to several millimetres. When the critical feature size of devices and structures is in the sub-micron scale, they are often referred to Nano-Electro-Mechanical systems (NEMS). MEMS and NEMS are crucial to the revolution of consumer and industrial technologies due to their advantageous reductions of small size and low cost of production. In addition, they are able to provide significant improvements in terms of performance compared to large devices. Due to the diversity of their application fields, MEMS are prominent in a variety of industries such as automotive, communications, medical and electronics.

MEMS device fabrication is based on the integrated circuit semiconductors fabrication processes [2]. Most MEMS devices are fabricated by using bulk micromachining, surface micromachining and lithography processes [3]. Micromachining has become a fundamental technology to fabricate MEMS devices such as sensors and actuators [1, 2].

Most MEMS devices are transducers that serve as sensors or actuators. A transducer is a device that transfers signals from one physical domain to another for purposes of measurement or control [4]. Electro-mechanical transducers have been commonly encountered in the last decade. However, MEMS transducers that use electro-thermal or thermo-mechanical interactions to convert heat into electrical signals or mechanical vibrations also exist. Optical and biochemical MEMS transducers are under investigation and development [5]. MEMS have many applications, such as gas sensors, accelerometers, biosensors, gyroscopes, micromirrors, atomic force microscope probes and magnetic sensors [1, 2, 6].

MEMS transducers are also classified into sensors and actuators. A MEMS sensor is a

device that is used to convert a physical quantity in the surrounding environment, such as temperature, into an an electrical signal that can be read by an observer [1]. On the other hand, a MEMS actuator is a device that converts energy, such as electrical energy, into a motion like an electrostatic actuator [1]. MEMS sensors can be based on electrostatic, piezoelectric, piezoresistive or electromagnetic mechanisms. Moreover, MEMS actuators use electrostatic, electromagnetic and electrothermal excitation mechanisms to produce motion.

2.1 Microsensing

In the sensing scenario, a physical quantity, such as pressure or temperature, is working as an external input that is applied to the transducer and results in a change in electrical properties, for example by changing the capacitance between a movable and a stationary electrode. The most important types of the MEMS sensors are discussed in the following paragraphs.

In piezoelectric sensors, an applied force results in mechanical strain and a potential difference across a piezoelectric crystal [7, 8]. That electric signal can be used for sensing. It has a relatively low operational voltage and low power consumption. In addition, piezoelectric materials, such as aluminum nitride, zirconium titanate and zinc oxide, have been utilized in many micro system applications such as pressure and temperature sensors [9].

A capacitor is a device that relates the charge to the voltage. It consists of two conductors that are separated by a nonconducting material [10]. Most MEMS capacitive sensors consist of two layers where one is able to move and is called the movable plate and the other is not free to move and is called the stationary plate (electrode).

2.2 Microactuation

One of the most useful features of MEMS devices is their ability to generate mechanical motion at the micro scale. There are three common mechanisms that are used to drive these devices: electrothermal, electrostatic and electromagnetic actuation. Each one of these actuation mechanisms has advantages and disadvantages with respect to power consumption, motion range, and response time. A brief overview of each driving mechanism is presented in the following.

Electrothermal Actuation

Electrothermal actuation can be utilized to actuate MEMS devices. It is based on thermal expansion caused by Joule heating [11]. As a voltage source supplies an electrical current passing through a flexible microstructure, it also acts as a heater. Thermal expansion of the microstructure, due to temperature rise, produces displacement. Electrothermal actuation is simple in terms of fabrication but it tends to consumes high power and large time constants [11, 12].

Electrostatic Actuation

The most common actuation method in MEMS devices is electrostatic actuation. It can be found in either parallel-plate or comb finger forms. The electrostatic actuator most commonly used is a variable capacitor consisting of a fixed and a moving electrode that is driven by voltage difference between the two electrodes as shown in the Fig. 2.1. The

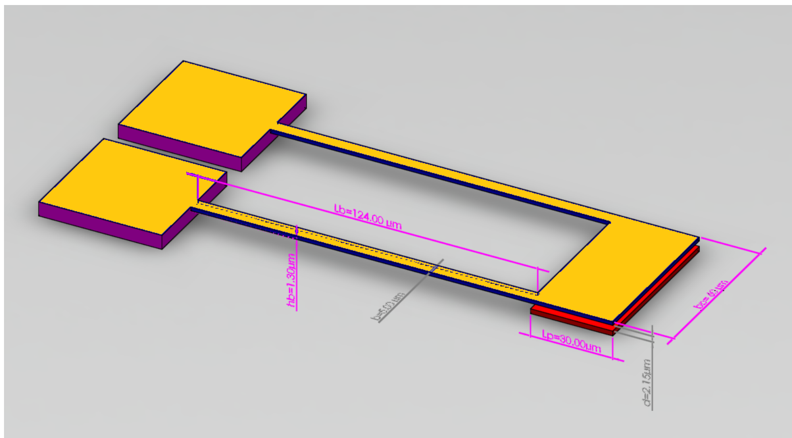

Figure 2.1: *A schematic drawing of an electrostatic actuator.*

position of the moving electrode is determined by the balance of the mechanical restoring force and the electrostatic force. When the two forces are equal a bifurcation point called (pull-in) occurs [13]. This point limits the deflection of the moving plate [13]. Electrostatic MEMS devises are simple to fabricate using surface micromachining. An important advantage of electrostatic actuation is their low power consumption.

Electrostatic actuation is based on the attractive force between the two plates of a capacitor. To understand the electrostatic force, we consider a popular form of electrostatic

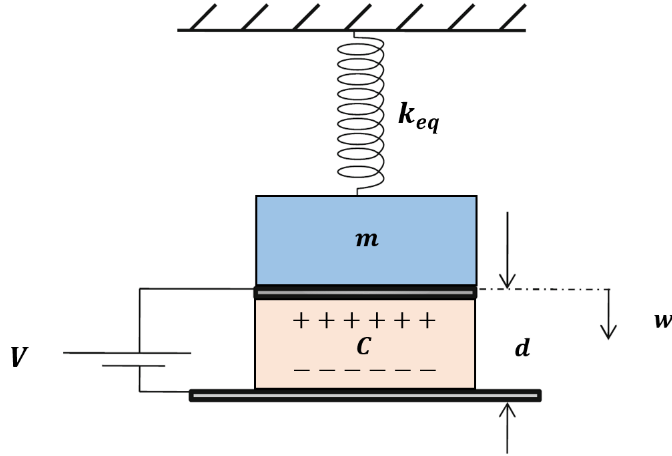

Figure 2.2: *A schematic drawing of a parallel plate capacitor.*

actuators consisting of two parallel plate electrodes, one of which cannot move, called the fixed electrode, and another able to move toward or away from the fixed electrode by a displacement $w(t)$, as illustrated in Fig. 2.2. The force acting on the movable plate depends on the voltage difference V between the two plates. The two plates hold equal and opposite amounts of charge given by [6]

$$Q_e = C\ V \tag{2.1}$$

where C is the capacitance defined by

$$C = \frac{\epsilon\ A}{d - w} \tag{2.2}$$

ϵ is free space permittivity, A is the two plates common area, and d is the initial (un-actuated) capacitor gap. The stored potential energy in the capacitor can be expressed as

$$U_c = \frac{1}{2} C\ V^2 \tag{2.3}$$

The electrostatic force can be derived using Castigliano's Theorem as the negative derivative of the potential energy with respect to the deflection $\hat{w}$.

$$F_{es} = -\frac{\partial\ U}{\partial\ w} = \frac{\epsilon\ A\ V^2}{2(d - w)^2} \tag{2.4}$$

Electrostatic actuation typically requires higher actuation voltages compared to other actuation techniques. The electrostatic actuation force is nonlinear which leads to nonlinear

phenomena in MEMS devices, such as pull-in. Fig. 2.2 shows a schematic of an electrostatic parallel plate actuator. In the equilibrium position, the electrostatic force is equal to the restoring force of the microstructure. When voltage is applied to the capacitor, the electrostatic force works to reduce the capacitor plates separation distance $(d-w)$. At small voltages, the electrostatic force is balanced by the restoring mechanical force $F_{em} = k_{eq}\ w$ and the electro-mechanical equilibrium condition is given by

$$k_{eq}\ w = \frac{\epsilon\ A\ V^2}{2\ (d-w)^2} \tag{2.5}$$

where k_{eq} is the effective stiffness of the mechanical structure.

The equilibrium equation can also be written as a third-order polynomial

$$-2\ k_{eq}\ w^3 - 4\ d\ k_{eq}\ w^2 - 2\ d^2\ k_{eq}\ w = \epsilon\ A\ V^2 \tag{2.6}$$

At different values of voltage V, the polynomial has three solutions, one solution represents a displacement value larger than the capacitor gap which is unphysical. The other two solutions represent stable and unstable equilibrium points within the capacitor gap [6]. Fig. 2.3 shows all possible relationships between the electrostatic force F_{es} and the mechanical force F_{em} acting on the parallel plate actuator. For low voltage values, the case shown in Fig. 2.3(a) represents the relationship between the two forces F_{es} and F_{em}. The stable and unstable equilibrium points appear at the intersection of the two curves. As voltage increases, the electrostatic force increases and eventually the case shown in Fig. 2.3(b) occurs where the mechanical restoring force F_{em} line is tangent to the electrostatic force F_{es} curve. In that case, the stable and unstable equilibrium points meet at the tangent point. This is called the pull-in condition and the corresponding voltage is called the pull-in voltage V_{pin}. For voltage values larger than V_{pin}, the case shown in Fig. 2.3(c) applies. The lack of intersection points indicates that no equilibrium points exist. For voltages values larger than the pull-in voltage there are no stable equilibria and the two capacitor plates come into contact.

Many recent applications require electrostatic microactuators that combine large stroke and low actuation voltage. The counter proportional relationship between the electrostatic force and the square of the capacitive gap, and therefore the stroke, precludes the option of increasing the gap size. Many studies have concentrated on design, modelling and characterization of electrostatic MEMS actuators to improve their performance by increasing the displacement limit at pull-in and decreasing the actuation voltage [14, 15, 16].

Literature has examined methods to obtain large static displacements from electrostatic actuators as well as methods to generate large orbit oscillations. Examples of large

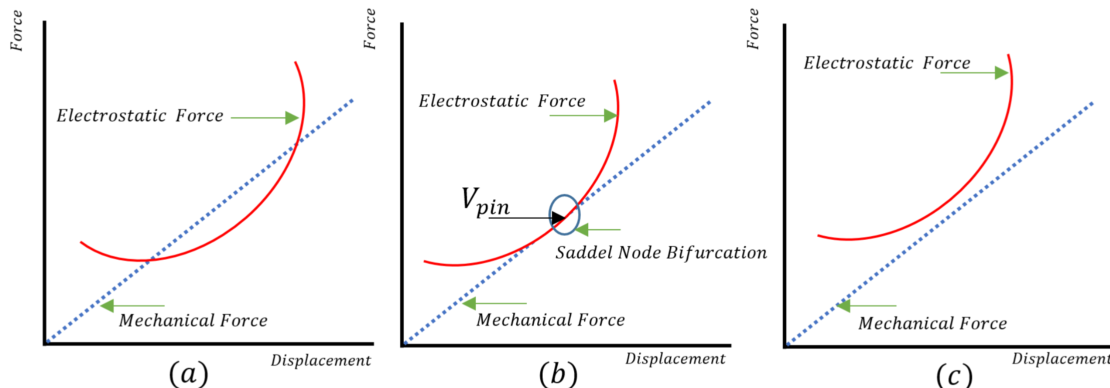

Figure 2.3: *Equilibrium points of an electrostatic actuator lumped-mass model for three voltage values: (a) $V < V_{pin}$, (b) $V = V_{pin}$ and (c) $V > V_{pin}$.*

stroke actuators include the Digital Light Processor (DLP), MEMS switches, and probes of atomic force microscopes. On the other hand, scanning micromirrors represent oscillatory actuators.

Static and dynamic electrostatic MEMS actuators encounter several nonlinearities that include electrical and mechanical quadratic and cubic nonlinearities in addition to a pull-in instability. It is important to accurately account for these nonlinearities when designing MEMS actuators in order to accurately predict the onset of bifurcations and instabilities as well as to obtain desirable device performance.

In the following, we discuss actuation mechanisms proposed to move electrostatic actuators through large stable displacements under V_{dc} voltage actuation. Chatrjee and Pohit [17] investigated an electrostatic micro cantilever with a large gap between the movable and stationary electrodes. In their analysis, they studied the effect of electrostatic force and geometric nonlinearities on the cantilever beam deflection and frequency response. Moeenfard *et al.* [18] reported that a Casimir force acting on an electrostatically actuated torsional microstructure leads to significant reductions in pull in voltage and stable displacement limit.

He *et al.* [19] utilized an out-of-plane repulsive-force to realize a large stroke, translational electrostatic actuator. It consists of a central microplate supported by four beams and actuated by four repulsive rotational comb finger actuators. Once the voltage is applied, the actuators generate the same angle which results in a translation motion of the microplate. Experimental measurements showed that the actuator can achieve an out-of-

plane displacement of 86μm for a driving voltage of 200 V. Towfighian et al. [20] redesigned the comb drive electrostatic actuators to produce an out-of-plane displacement of 58 μm for actuation voltage of 25 V.

Another electrostatic MEMS actuator with a large out-of-plane stroke was demonstrated by Hu *et al.* [21]. The actuator is designed to eliminate the effect of the pull-in instability and to enhance the microstructure deflection. It is fabricated in two layers. The top layer forms the actuator platform and support springs while the bottom layer is made of two sets of electrodes; one directly under the structure and another at an offset distance from it. A repulsive electrostatic force is generated when a voltage difference is applied between the structure and the offset electrodes. They reported that the actuator can achieve a displacement of 2.7 μm for a driving voltage of 50 V.

A novel electrostatic MEMS actuator based on electrostatic attractive and repulsive forces has been demonstrated by Hao *et al.* [22]. The actuator can be operated in attractive and repulsive modes to maximize the displacement and minimize the limitation of the pull-in instability. Experimental results showed that a displacement of 1.47 μm is obtained from the repulsive force mode at 130 V and a displacement of 0.63 μm is obtained from the attractive mode at 15 V. Using capacitive sensing, a feedback control utilized to magnify the stable displacement of a parallel plate actuator. The actuator achieved a displacement of ± 2 μm within a ± 2.25 μm gap with a range of actuation voltage from 0 to 10 V [23].

Some electrostatic actuators have used mechanical and electrical magnification techniques to achieve a large stroke. Hao *et al.* [24] designed an electrostatic actuator based on the lever principle to move a central mass out-of-plane. They found that, when the voltage is applied, a small downward displacement is observed on the short arm of the lever. This displacement is amplified by the lever to achieve a larger upward displacement on the central mass attached at the end of the long arms. Their design achieved a displacement of 1.45μm at 50 V which was larger than the displacement of the same structure without the lever mechanism. Trivedi *et al.* [25] showed that the static and dynamic travel ranges of beam actuators can be increased be applying shape optimization to the beam profile. Cheng *et al.* [26] demonstrated an actuator that achieves a low actuation voltage of 6 V using highly compliant support springs fabricated from Parylene-C.

Park *et al.* [27] investigated the actuation voltage of a parallel plate actuator driven by a resonant drive circuit that magnifies a frequency-modulated input signal. They found that this is an efficient method to reduce the actuator voltage requirements. Hu *et al.* [28] proposed the use of two-level electrodes and a curved down support spring to obtain a large stroke at a low actuation voltage. Their actuator achieved experimentally a 2 μm stroke at an actuation voltage of 10 V.

Structure and electrostatic force nonlinearities play an important role in the performance of dynamic electrostatic MEMS actuators [29, 30, 31]. To investigate these effects, many researchers have developed analytical models and experimental techniques to understand the system behavior. When a microstructure is excited electrostatically, two classes of resonances appear: primary and secondary resonances. Primary resonance occurs at an excitation frequency near to one of the structure's fundamental frequencies while secondary resonances occur at excitation frequencies that are integer multiples or submultiples of the natural frequencies [6, 32]. To enhance the performance of dynamic MEMS actuators, they frequently operate at resonance to maximize the response amplitude. The following summarizes recent work in the field of primary and secondary resonances of the electrostatic MEMS actuators.

Younis and Nayfeh [33] analytically investigated the primary resonance of an electrostatic microactuator. Abdel-Rahman and Nayfeh [34] theoretically predicted that exciting an electrostatic actuator near its subharmonic or superharmonic resonances will result in dynamic responses at the same order-of-magnitude as primary resonance. Primary, superharmonic, and subharmonic resonances of an electrostatic actuator were demonstrated experimentally by Younis and Alsaleem [35]. Also, they found that secondary resonances play an important role in MEMS actuation. It was theoretically found that when the actuator is being excited near to its superharmonic or subharmonic resonances, it exhibits a dynamic response of the same order of magnitude compared to primary resonance excitation.

Najar *et al.* [36] investigated the dynamic response of a microbeam electrostatic actuator by utilizing a discretization technique that combines the differential quadrature method and finite difference method. This technique was used to generate a wide range of frequency-response curves as well as to study the global behavior of the actuator near primary and secondary resonances.

Han *et al.* [37] developed a mathematical model that includes both the electrostatic force and cubic stiffness to investigate the nonlinear dynamic response of doubly clamped microbeams excited by two symmetric side electrodes. They found that the combination of the nonlinearities may lead the system response to be harding or softening. Alkharabsheh and Younis [38] experimentally and analytically investigated the dynamic response of curve microbeam actuator excited electrostatically near primary resonance and the superharmonic resonance of order two utilizing the shooting method. They found that nonideal boundary conditions have a significant effect on the static and dynamic response of MEMS actuators. The superharmonic and subharmonic resonances of micro-actuators with nonideal supports have also been studied analytically by Ekici and Boyaci [39] using the multiple scales method .

An electrostatic beam actuator with two side electrodes has been shown to achieve 3.8 times the maximum displacement at resonance compared to an actuator with one side electrode [40]. The proposed actuator uses a pull-pull drive mode where the side electrodes carry identical in-phase actuation signals. This mode of operation was found to retard pull-in and reduce nonlinearity in the actuator response.

Finally, MEMS devices encounter environmental noise which play a significant role in the performance of static and dynamic MEMS actuators. Noise is a stochastic process without a deterministic value in the time or frequency domains. However, it can be described by its power spectral density (PSD) measured over a wide frequency range [41]. Common types of noise in electrostatic MEMS include electrical noise, thermo-mechanical (Brownian) noise, and external disturbances [41, 42, 43]. The impact of electrical noise on electrostatic actuators is particularly prominent since it causes stochastic variations in the actuation voltage, representing process noise. The dominant sources of electrical noise are thermal noise due to Brownian motion and flicker noise due to random charge hold and release events between silicon dioxide (SiO_2) and silicon (Si) layers. Flicker noise dominates electrical noise at low frequencies while thermal noise dominates at high frequencies,[41, 42, 44].

Electromagnetic Actuation

Electromagnetic actuators come in several types: Lorentz force actuators, reluctance actuators and permanent magnet actuators [45, 46, 47, 48]. They have a high scalability, low power consumption and provide larger motion ranges than other actuation methods [49, 50]. Reluctance and permanent magnet actuators require magnetic materials during the fabrication process. However, many magnetic materials cannot be deposited with MEMS fabrication techniques which results in fabrication and material limitations [52]. To avoid these limitations, MEMS actuators based on a Lorentz force were introduced [53]. This force appears due to interaction between an excitation current that passes through a microstructure and a magnetic field. It does not require a specific magnetic material during fabrication. Lorentz force actuators can be fabricated using standard micromachining techniques [54]. They linearly depend on the magnitude of current passing through a current loop.

Miyajima *et al.* [55] used the Lorentz force to excite a one-axis (4.2×3) mm scanning micromirror for a commercial confocal laser scanning microscope. The mirror was shown to rotate from 0 to 16° at a driving current less than 20 mA using two 0.5 T permanent magnets.

Cho *et al.* [56] fabricated a two-axis micromirror actuated by a Lorentz force. By adjusting the direction of the applied current, the micromirror can selectively rotate around the x-axis or y-axis. The results show that the micromirror rotates $\pm 4.35^\circ$ around the x-axis at a DC current of 120 mA and $\pm 15.7^\circ$ around the y-axis at a current of 80 mA in the presence of an external magnetic field intensity of $B = 0.16$ T. Cho *et al.* [57] fabricated a three DOF Lorentz force actuated micromirror that can rotate around the x and y axes and deflect along the z axis to improve coupling among optical components. The micromirror rotates $\pm 4.2^\circ$ around the x-axis at a DC current of 115 mA and $\pm 9.2^\circ$ around the y-axis at a current of 120 mA. Also, it deforms 42 μm in the z axis where the actuation voltage sets to equal 3 V.

Ahn *et al.* [58] designed a similar two DOF scanning micromirror using Lorentz force actuation induced by AC current. The micromirror achieved $\pm 1.51^\circ$ at 20 mA while operating in resonance. Xingdong *et al.* [59] introduced a novel electromagnetic multiply-folded beam actuator to produce a displacement of 47 μm with a magnetic field of 0.3 T and a driving current of 8 mA.

Comparison of Actuation Mechanisms

To conclude this discussion, we note that electrothermal actuation has the advantage of simple fabrication. It is a useful mechanism to obtain large strokes, for instance in micromirrors. However, it consumes high power because of it relies on Joule heating. It also has a large time constant limiting it to relatively slow applications. Electrostatic actuation has much lower power consumption rates and a much smaller time constant. However, achieving a large stroke using an electrostatic force leads to high actuation voltages since it requires a large gap. Lorentz force actuation can be used to increase the stroke while maintaining a similar time constant to electrostatic actuation. It also limits the power consumption to a level less than those required for electrothermal actuation. Table 2.1 summarizes the advantages and disadvantages of each of the actuation methods described previously.

Table 2.1: Comparison of Actuation Mechanisms in MEMS

Actuation method	Advantages	Disadvantages
Electrothermal Actuation	Low actuation voltage Easy to fabricate	High power consumption Slow response time
Electrostatic Actuation	Low power consumption Fast response time Easy to fabricate	High actuation voltage Limitted by pull-in voltage
Electromagnetic Actuation	Low actuation voltage Large displacement	Difficulty to fabricate Large device size

Chapter 3

Electrostatic MEMS Actuator

In this chapter, we investigate the static and dynamic behavior of a one DOF microactuator under the effect of the electrostatic force and squeeze-film damping. The microstructure is mathematically modelled based on the lumped mass method and the results are verified using a finite element model (FEM)[1]. Euler-Bernoulli beam theory is utilized to determine the structural stiffness of the micro-beams.

3.1 The Actuator

The electrostatic MEMS actuator consists of a substrate electrode that sits underneath a microplate supported by two cantilever beams as shown in Fig. 3.1. The actuator is made of polysilicon using the PolyMUMPs fabrication process[2]. The physical dimensions of the actuator are summarized in Table 3.1. The material properties of polysilicon and air permittivity are listed in Table 3.2.

We consider a microactuator electrically actuated by an electrostatic force that consists of a static voltage component V_{dc} and a time-varying voltage component V_{ac}. The actuator is represented as a parallel plate capacitor which has two plates, one of which is stationary, called the electrode, and the other is a microplate which can move when the voltage changes between the electrode and the microplate.

[1] Comsol 4.4

[2] PolyMUMPs Fabrication Process is the standard process of MEMS devices

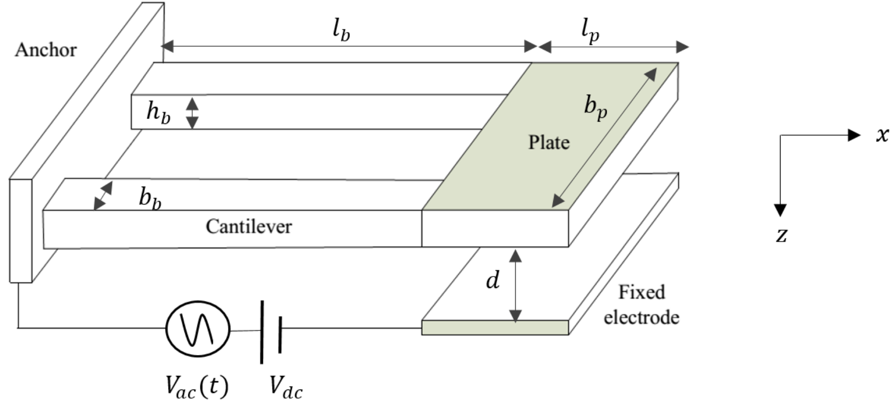

Figure 3.1: *A schematic drawing of the electrostatic actuator.*

Table 3.1: Dimensions of the Actuator

Description	Value (μm)
beam length (l_b)	124
width of the beam (b_b)	5
thickness of the beam (h_b)	1.3
length of the microplate (l_p)	30
width of the microplate (b_p)	60
thickness of the microplate (h_p)	1.3
gap (d)	2.15

3.2 Analytical Model

The term "lumped" refers to lumped-parameter analysis, as opposed to distributed-parameter analysis. The lumped element model applies certain assumptions to simply describe the behavior of spatially distributed physical systems. A typical system that is converted to the lumped-mass model consists of a point mass, a spring and a damper as shown Fig. 3.2. Lumped elements lead to ordinary differential equations describing the system's dynamic behavior while a distributed parameter system is described by partial differential equations. The other advantages of the lumped-mass model include enabling of static and dynamic analyses. On the other hand, lumped-mass methods have drawbacks such as, information

Table 3.2: Material Properties

Description	Value
Density (ρ)	2330 kg/m^3
Youngs Modulus (E)	160 Gpa
Yield strength (σ_y)	1.2 GPa
Poisson's ratio (ν)	0.22
Permittivity (ϵ)	8.854 $\times 10^{-12}$ F/m

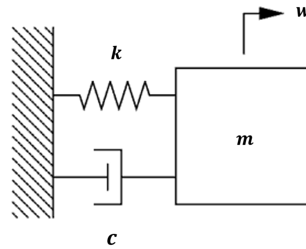

Figure 3.2: *A schematic of a spring-mass-damper model.*

loss due to the assumptions made during modelling. Another shortcoming is the inability to capture modal interactions in the system, only those modes explicitly considered in the model can be observed.

In lumped-mass modelling, we assume that the effective mass of the system is concentrated at the geometric center of the microplate. The microplate is assumed to be a rigid body, as illustrated in Fig. 3.2, consequently it does not contribute to the equivalent system stiffness. Further, the electrostatic force uniformly distributed on the microplate can be represented by a point force at the center of the microplate, Fig. 3.3(b). It can also be translated to the tip of the cantilever beam as a shear force and an end moment, Fig. 3.3(c).

The model considers the transverse deflection of the microplate due to the electrostatic force while ignoring the fringe field. During actuation, the microplate moves downward from its initial position toward the bottom electrode as shown in Fig. 3.4. In addition, the model accounts for the microplate inclination angle. It is assumed equal to the beam tip slope θ_b. This assumption changes the effective gap as shown in Fig. 3.5. The electrostatic force between the plates without accounting for the inclination angle is shown in Eq. (2.4).

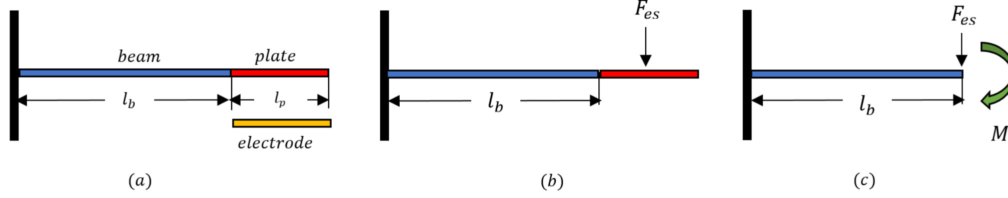

Figure 3.3: *A side view of the electrostatic actuator. (a) The initial position of the microplate, (b) the electrostatic force lumped as a point force at the center of the microplate and (c) the translated electrostatic force and end moment at the tip of the cantilever beam.*

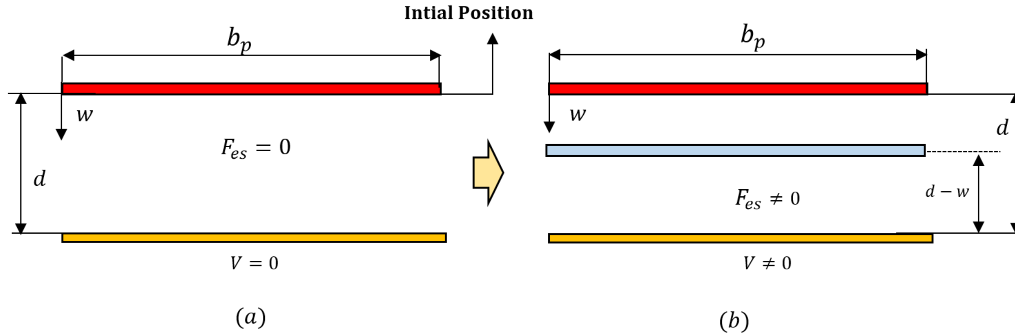

Figure 3.4: *(a) A schematic drawing of a microplate in the initial position and (b) microplate position after the actuation voltage is applied.*

The corrected form of the electrostatic force is

$$F_{es} = \frac{\epsilon\ A\ V^2}{2(d - w - n)^2} \tag{3.1}$$

where w is the displacement at the beam tip and n is the change in the microplate position due to the inclination angle. The change in the microplate height at its center n, Fig. 3.6, can be written as

$$\sin\theta_b = \frac{n}{l_p/2} \tag{3.2}$$

For small deformations, we can write

$$\sin\theta_b = \frac{w}{l_b} \tag{3.3}$$

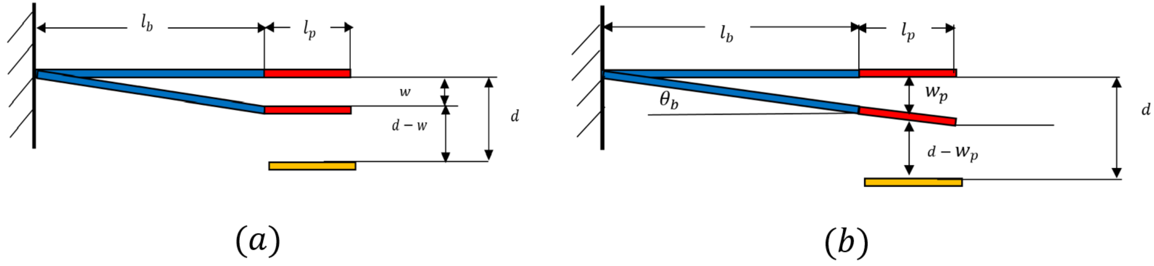

Figure 3.5: *A schematic drawing of the actuator deformation due to the electrostatic force. (a) inaccurate (flat microplate) model and (b) accurate (inclined microplate) model.*

Solving Eqs. (3.2) and (3.3) for n, we obtain

$$n = \frac{l_p}{2l_b} w = \gamma w \tag{3.4}$$

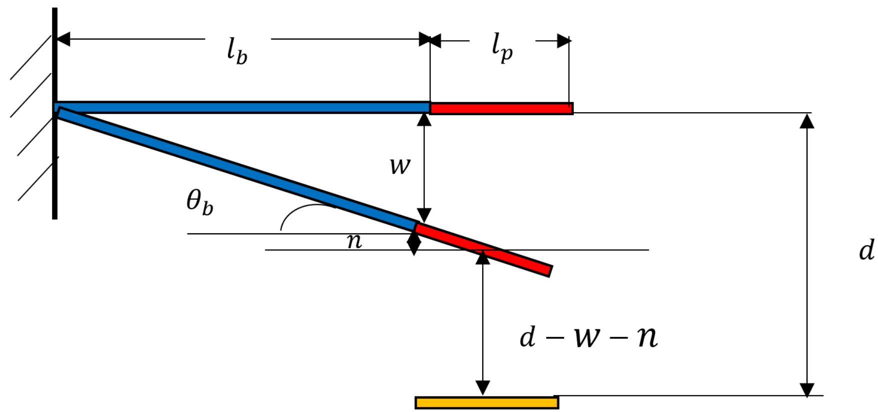

Figure 3.6: *A schematic drawing of the microplate bending angle under the effect of the electrostatic force.*

3.2.1 Lumped Elements

For a cantilever beam, we can compute the effective bending stiffness using the a formula which accounts only for an applied force at the tip of the cantilever [60]:

$$k = \frac{3EI}{{l_b}^3} \tag{3.5}$$

where E is Young's Modulus, I is the second moment of area and l_b is the length of the cantilever beam. The second moment of area is:

$$I = \frac{b_b \ {h_b}^3}{12} \tag{3.6}$$

where b_b and h_b are the microbeam width and thickness, respectively. The actuator consists of two parallel cantilevers. We model the equivalent bending stiffness of the system as shown in Fig. 3.7

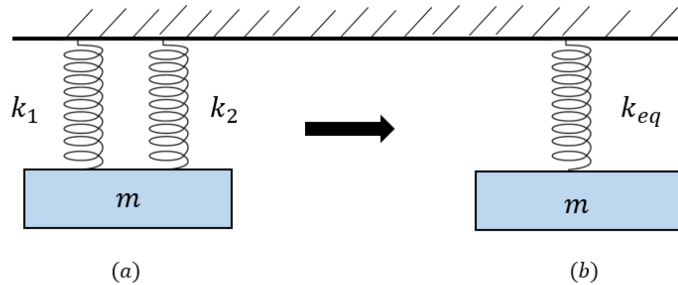

Figure 3.7: *A schematic drawing of cantilever beams as (a) parallel springs and (b) an equivalent spring .*

Equation (3.5) is not adequate in our case because of the presence of an end moment at the beam tip. The correct formula can be found by applying Euler-Bernoulli beam theory with the associated boundary conditions. Since the lumped-mass model assumed the electrostatic force as a point force at the center of the mass, lying at $\frac{l_p}{2}$ beyond the beam tip, the summation of moments at a beam section x distance from the support is

$$M_x - F_{es}(l_b + \tfrac{1}{2}l_p - x) = 0 \tag{3.7}$$

We can write the end moment as

$$M_p = F_{es}\frac{l_p}{2} \tag{3.8}$$

From Euler-Bernoulli beam theory, we write the section resistance to rotation as

$$M_x = EI\frac{\partial^2 w_b}{\partial x^2} \tag{3.9}$$

where w_b is the displacement of the beam.

Substituting Eq. (3.9) into Eq.(3.7), integrating over the beam span, and using the boundary support conditions $w_b(0) = 0$ and $\dot{w}_b(0) = 0$, the displacement of the beam can be found as

$$EIw_b = \frac{1}{2}\ F_{es}\ l_b\ x^2 + \frac{1}{4}\ F_{es}\ l_p\ x^2 - \frac{1}{6}\ F_{es}\ x^3 \tag{3.10}$$

The deformation of the tip can be found by substituting $x = l_b$ in Eq. (3.10) to obtain

$$EIw = \frac{1}{3}\ F_{es}\ l_b\ l_b^2 + \frac{1}{4}\ F_{es}\ l_p\ l_b^2 \tag{3.11}$$

and as a result

$$w = F_{es}\frac{\frac{1}{3}\ l_b^3 + \frac{1}{4}\ l_p\ l_b^2}{EI} \tag{3.12}$$

A linear spring force can be written as $F = k\ w_b$. Therefore, the equivalent stiffness of each beam is

$$k = \frac{E\ b_b\ h_b^3}{4\ l_b^3 + 3\ l_b^2\ l_p} \tag{3.13}$$

and the equivalent stiffness of the actuator is

$$k_{eq} = \frac{2E\ b_b\ h_b^3}{4\ l_b^3 + 3\ l_b^2\ l_p} \tag{3.14}$$

To calculate the microstructure mass of the actuator, we consider the plate mass

$$m_p = \rho\ l_p\ h_p\ b_p \tag{3.15}$$

and the two beams mass

$$m_b = \rho\ l_b\ h_b\ b_b \tag{3.16}$$

The microstructure equivalent mass can be write as [60]:

$$m_{eq} = 0.23\ m_p + 2\ m_b \tag{3.17}$$

3.2.2 Equation of Motion

Fig. 3.8 (a) shows a 3D scan of the microstructure using a white profilometer. Fig. 3.8 (b) presents a picture of the actuator obtained through an optical microscope. The measured dimensions of the microstructure in μm are shown in the picture. The governing equation of motion of the microstructure in bending is derived using the lumped spring mass model as

$$m_{eq}\ddot{w} + c\dot{w} + k_{eq}w = F_{es} \tag{3.18}$$

Substituting for the electrostatic force using Eq. (3.1) and for the microplate center height using Eq. (3.4), the equation of motion becomes

$$m_{eq}\ \ddot{w} + (c_v + c_s)\ \dot{w} + k_{eq}\ w = \frac{\epsilon\ A\ V^2}{2(d - w - \gamma w)^2} \tag{3.19}$$

where c_v is the viscous damping coefficient and c_s is the squeeze-film damping coefficient.

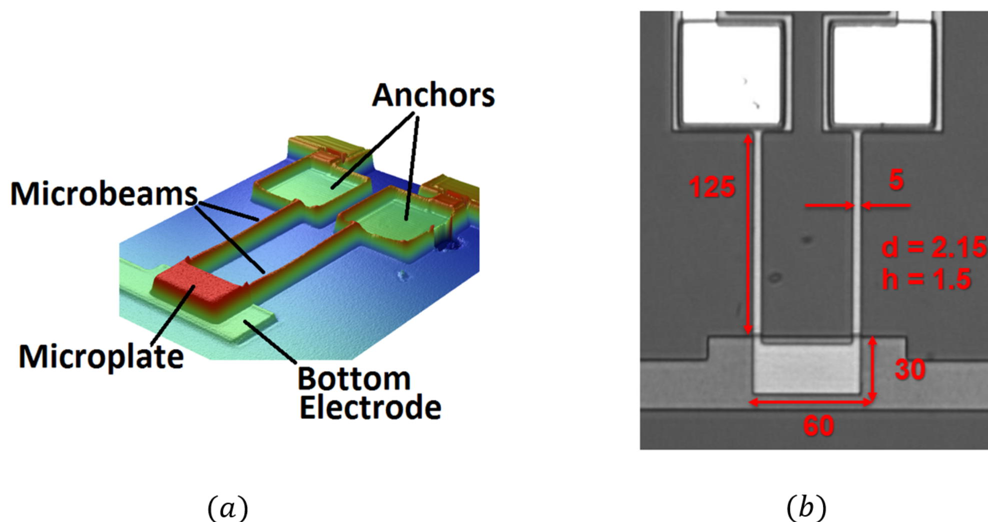

Figure 3.8: *(a) A 3D scan of the actuator using white a white light profilometer and (b) a picture of the actuator.*

For convenience, we introduce the following nondimensional variables to nondimensionalize the equation of motion

$$\hat{w} = \frac{w}{d}\ , \quad \hat{t} = \frac{t}{T} \tag{3.20}$$

where $T = \sqrt{\frac{m_{eq}}{k_{eq}}}$ is a time-scale. Consequently,

$$\dot{w} = \frac{\partial w}{\partial t} = \frac{d\ \partial \hat{w}}{\partial(\hat{t}T)} = \frac{d}{T}\dot{\hat{w}} \tag{3.21}$$

$$\ddot{w} = \frac{\partial \dot{w}}{\partial t^2} = \frac{d\partial \dot{\hat{w}}}{\partial(\hat{t}^2 T^2)} = \frac{d}{T^2}\ddot{\hat{w}} \tag{3.22}$$

Substituting Eqs. (3.20), (3.21) and (3.22) into Eq. (3.19), we obtain the nondimensional bending equation of motion as follows:

$$m_{eq}\ \frac{d}{T^2}\ \ddot{\hat{w}} + (c_v + c_s)\frac{d}{T}\ \dot{\hat{w}} + k_{eq}\ d\ \hat{w} = \frac{\epsilon\ A\ V^2}{2(d - d\ \hat{w} - d\gamma\hat{w})^2} \tag{3.23}$$

Dividing both sides by $(m_{eq}\ \frac{d}{T^2})$ and defining the parameters

$$\mu_1 = c_v \frac{T}{m_{eq}} \quad , \quad \mu_2 = c_s \frac{T}{m_{eq}} \quad , \quad \alpha\ = \frac{\epsilon\ A}{2\ d^3\ k_{eq}} \tag{3.24}$$

we can rewrite the equation of motion as

$$\ddot{\hat{w}} + (\mu_1 + \mu_2)\ \dot{\hat{w}} +\ \hat{w} = \alpha\ \frac{V^2}{(1 - \hat{w} - \gamma\hat{w})^2} \tag{3.25}$$

For the sake of brevity, we dispense with the over hat and rewrite the equation of motion as

$$\ddot{w} + (\mu_1 + \mu_2)\dot{w} +\ w = \alpha\ \frac{V^2}{(1 - w - \gamma w)^2} \tag{3.26}$$

Comparing Eq. (3.26) to the equation of motion for a spring-mass-damper system, we find that

$$\mu_1 = \frac{\omega_{nb}}{Q} \tag{3.27}$$

Further, by virtue of nondimensionalization, we note that $\omega_{ob} = 1$.

We adopt Bao's model [61] to model squeeze-film damping. This model analytically solves the linearized Reynolds equation with associated pressure boundary conditions. Assuming a uniform gap between two rigid plates, squeeze-film damping was found proportional to the cube of the distance between the movable plate and the substrate surface. In nondimensional form, it can be expressed as:

$$c_s = \frac{\beta\mu}{(1 - w)^3} \tag{3.28}$$

where β is a coefficient less than 1 related to the distance between the two rigid plates and μ is the fluid viscosity.

We will investigate the static and dynamic behavior of the electrostatic micro actuator. The lumped-mass model that was developed above is solved numerically for the static response of the actuator under a static V_{dc} load. The eigenvalue problem is solved in order to find the natural frequency of the actuator at a given static load. Moreover, the dynamic response is investigated under different excitation forces and the results are compared in the presence and absence of squeeze-film damping. Therefore, this section investigates three major phenomena in the electrostatic MEMS actuators:

- The pull-in voltage and the static stability of the actuator
- Eigenvalue analysis
- Dynamic response under various excitation forces

3.3 Static Analysis

Pull-in in electrostatic MEMS devices is an important phenomenon caused by a static bifurcation at a specific actuation voltage. At this voltage, the microplate suddenly sticks to the bottom electrode. This voltage is known as the pull-in voltage V_{pin}. The time-dependent acceleration and velocity terms in the equation of motion, Eq. (3.26), are set equal to zero and the actuation voltage is set a constant value V_{dc} to obtain the static equilibrium equation:

$$w_s = \alpha \, \frac{V_{dc}^2}{(1 - w_s - \gamma w_s)^2} \tag{3.29}$$

This algebraic equation is then solved numerically for the static equilibrium positions corresponding to V_{dc}.

The FEM package COMSOL Multiphysics 4.4 is also used to solve the Ordinary Differential Equations (ODEs) describing the static deflection of the support beams and end plate under electrostatic force. The following steps are performed to simulate the micro-actuator:

1. A 3D model is created using the dimensions of the actuator listed above.
2. Material properties are specified. In this model, two materials were defined: PolySilicon for the structure and air for the electrostatic field between the two electrodes.

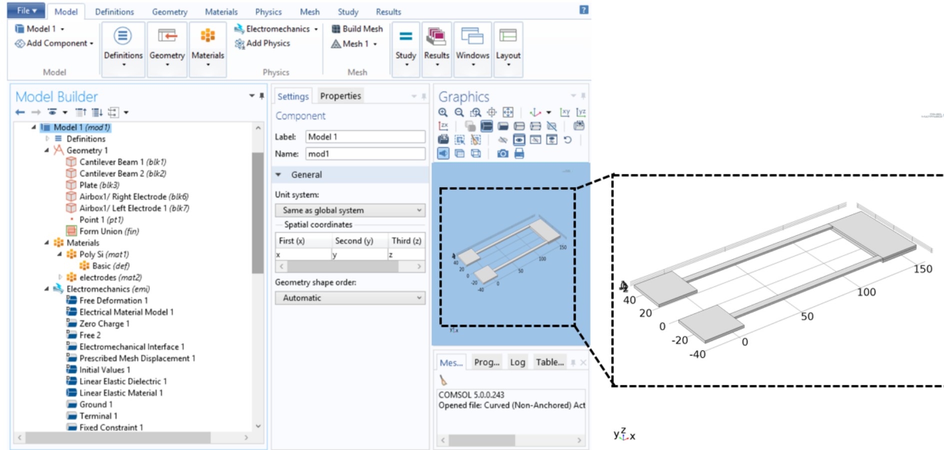

Figure 3.9: *Comsol setup using steps 1-4.*

3. Material behavior is defined as linearly elastic, the voltage of the bottom electrode is set to ground, the voltage of the microplate is set to V_{dc} and the boundary conditions of the support beams at the anchors are set fixed.
4. The Electromechanics module/physics is then used to analyze the model shown in Fig. 3.9 .
5. The mesh element size was set to Normal resulting in the mesh shown in Fig. 3.10.

The FEM model of the actuator geometry is build based on tetrahedral meshing with a maximum element size of (15.5μm) and a minimum element size of (2.97μm). The actuation voltage was initially set to $V_{dc} = 0$ and increased incrementally in steps of 0.3V over the range 0–13 V to capture the static pull in voltage. The voltage at which the solver diverged was noted. Voltage sweeps were then carried out with a smaller voltage step 0.1 V to refine our estimate of the pull-in voltage as that where the solver diverged again with the smaller step size.

The pull-in voltage was calculated as 9.5 V where the actuator losses stability. Fig. 3.11 shows the relationship between the microplate center deflection and V_{dc}. Deflection increases with V_{dc} until the saddle node bifurcation point. The stable (solid blue line) and unstable (dashed red line) branches of solutions collide and annihilate each other at the bifurcation point.

The actuator's stable equilibrium increases nonlinearly with the actuation voltage V_{dc}, Fig. 3.11, while the unstable equilibrium decreases with V_{dc}. At pull-in, a saddle-node

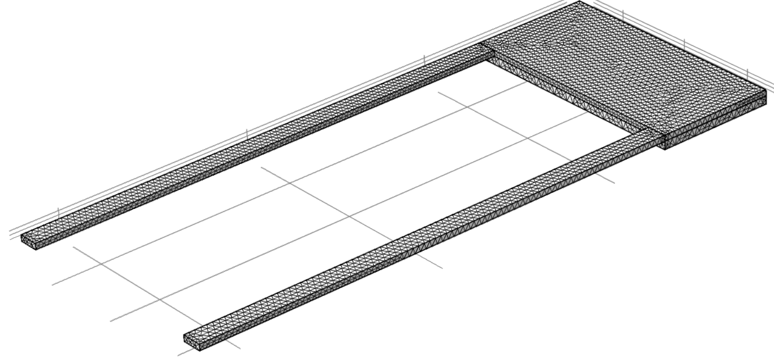

Figure 3.10: *The meshing size element of the actuator.*

bifurcation occurs where the stable and unstable equilibria meet which can be used as an indicator of pull-in. Beyond that voltage ($V_{dc} > V_{pin}$), no physical equilibrium solutions ($w_s \leq 1$) exist. The maximum stable deflection, at $V_{dc} = V_{pin}$, is called the pull-in deflection w_{pin}.

The numerical results of the model were verified by comparing them to the results of FEM simulations. The figure shows a good agreement between the lumped-mass model stable equilibria and those predicted by FEM.

3.4 Eigenvalue Analysis

We investigate the variation of the fundamental natural frequency as a function of the static load V_{dc}. Substituting with the expansion $w = w_d$, expanding the electrostatic force around zero in a Taylor series, ignoring the resulting nonlinear terms, and, we obtain:

$$\ddot{w}_d + \omega_{ob}^2 w_d = 2\ \frac{\alpha(1+\gamma)}{(1 - w_s - \gamma w_s)^2} V_{dc}^2 w_d \tag{3.30}$$

Substituting the harmonic solution $w_d = Ae^{i\omega_{nb}t}$ form into the linearized equation of motion, we obtain the undamped eigenvalue problem:

$$-\omega_{nb}^2 w_d + \omega_{ob}^2 w_d = \Big(2\ \frac{\alpha(1+\gamma)}{(1 - w_s - \gamma w_s)^2}\ V_{dc}^2\Big) w_d \tag{3.31}$$

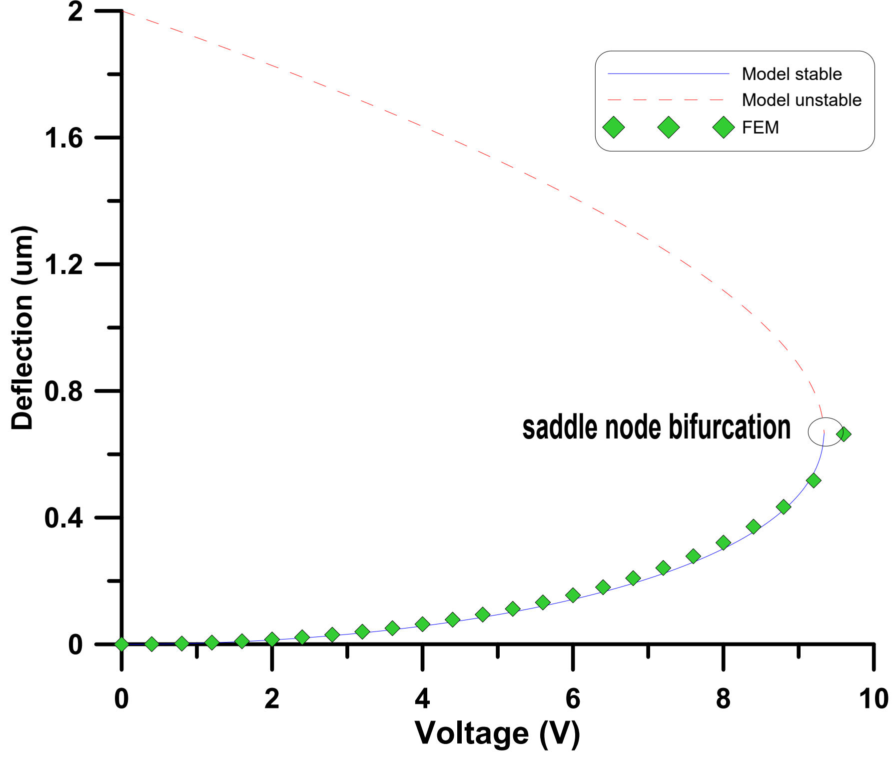

Figure 3.11: *Model predicted stable (solid blue line) and unstable (dashed red line) equilibria. Stable FEM predicted equilibria are marked with green ◇ symbols.*

Ignoring the static part, Eq. (3.31) can be written as

$$\omega_{nb}^2 = \omega_{ob}^2 - 2\ \frac{\alpha(1+\gamma)}{(1-w_s-\gamma w_s)^2}\ V_{dc}^2 \tag{3.32}$$

Assuming that the boundaries of electrostatic force are constant and static deflection is equal to zero (w_s=0), Eq. (3.32) reduced to

$$\omega_{nb}^2 = \omega_{ob}^2 - 2\ \alpha(1+\gamma)\ V_{dc}^2 \tag{3.33}$$

Thus, the first nondimenstional bending natural frequency can be expressed as

$$\omega_{nb} = \pm\sqrt{\omega_{ob}^2 - 2\ \alpha(1+\gamma)\ V_{dc}^2} \tag{3.34}$$

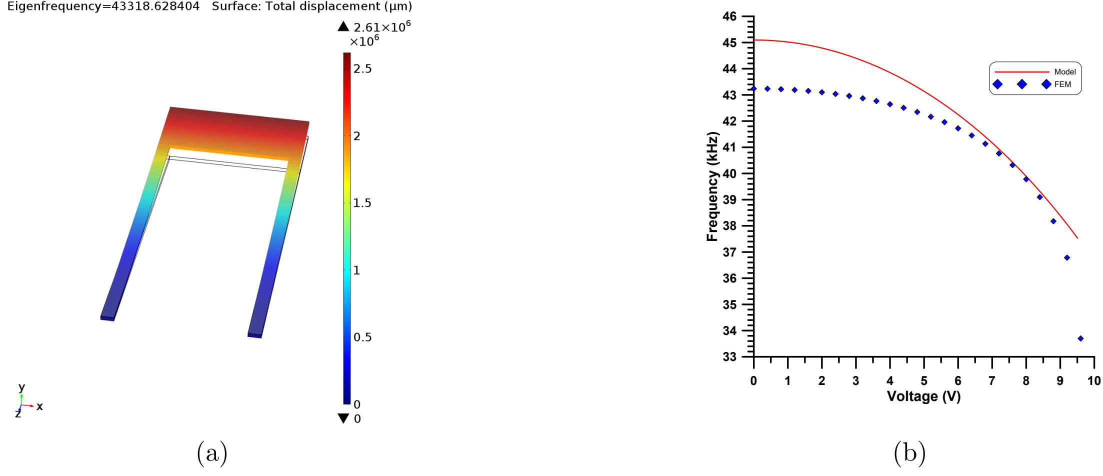

(a)

(b)

Figure 3.12: *(a) The first mode shape obtained from the FEM and (b) a comparison of the corresponding natural frequency results to the applied voltage that obtained from the lumped-mass model (red line) and FEM (blue ◇ symbols).*

The bending natural frequency can be written in Hz as

$$f_{nb} = \frac{\omega_{nb}}{2\pi T} \tag{3.35}$$

The first bending natural frequency of the actuator is calculated using the results of the static analysis described above to obtain w_s. The natural frequency of the first bending mode is obtained as $f_{ob} = 45.03\,\text{kHz}$ from the lumped-mass model and as 42.149 kHz from FEM. The difference in the natural frequency values is expected because the FEM is a multidegree of freedom model and will capture the natural frequencies more accurately than the single degree of freedom model. Fig. 3.12(a) shows the first mode shape that is observed from the FEM. The natural frequency of the first bending mode obtained from both models is depicted in Fig. 3.12(b) with respect to the input V_{dc}. Due to the increase of V_{dc}, the microstructure softens and that results in a frequency drop.

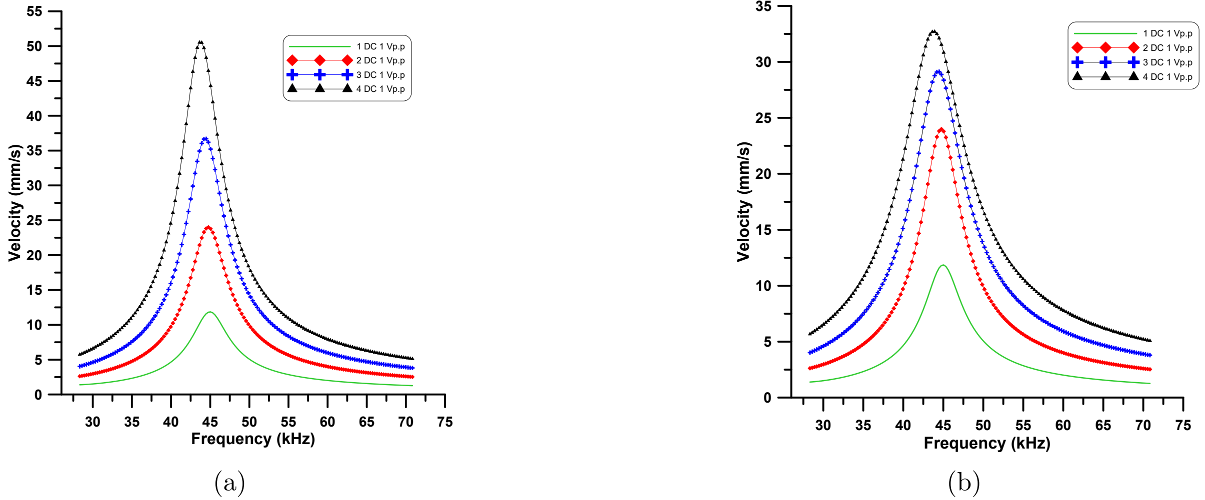

Figure 3.13: *The frequency-response curves of the actuator in the (a) absence and (b) presence of squeeze-film damping.*

3.5 Dynamic Analysis

In this section, we numerically investigate the nonlinear dynamics of the electrostatic actuator under time-varying excitation forces such that

$$V = V_{dc} + V_{ac}\cos(\Omega t) \tag{3.36}$$

where V_{ac} is the amplitude and Ω is the frequency of the excitation voltage in (rad/s) and f in Hz. Using this voltage in Equation (3.26), we obtain

$$\ddot{w} + (\mu_1 + \mu_2)\dot{w} + w = \alpha\,\frac{(V_{dc} + V_{ac}\cos(\Omega t))^2}{(1 - w - \gamma w)^2} \tag{3.37}$$

The quality factor was set Q=10, a typical value for this class of actuators. The frequency-response curves were obtained for the frequency range of 25–72 kHz in the vicinity of first bending natural frequency of the actuator ($f_{nb} = 45.3\,\text{kHz}$) for two different cases. Firstly, the voltage amplitude was set to be V_{ac}= 1 V while V_{dc} was varied from 1V to 4V. Fig. 3.13 shows the frequency response curves in the absence, Fig. 3.13(a), and presence, Fig. 3.13(b), of squeeze-film damping.

This analysis is carried out to determine the effect of various modes of damping on the dynamic response. Comparison of Fig. 3.13 (a) and (b) shows that as V_{dc} increases and

the distance between the microplate and the substrate becomes smaller the influence of squeeze-film damping increases resulting in significantly smaller response in sub-figure (b) compared to sub-figure (a) for the same waveform. To counter the effect of squeeze-film, the actuator was placed inside a vacuum chamber. When the static voltage $V_{dc} = 1\,\mathrm{V}$, the peak occurs at the resonance ($f_{nb} = 45.3\,\mathrm{kHz}$); however, if V_{dc} increases to 4 V the peak is shifted, and it occurs at 41.6 kHz indicating a softening system as shown in Fig. 3.13. These changes are caused by the nonlinearity of the electrostatic force.

Secondly, the electrostatic actuator was excited at different values of V_{ac} and at $V_{dc} = 2\mathrm{V}$ to study the resonances of the actuator. As V_{ac} increases, another resonance appears in the Fig. 3.14 at $\Omega = \frac{1}{2}\omega_{\circ b}$ in addition to that at $\Omega = \omega_{\circ b}$. These resonances come from the fact that the electrostatic force is a multi-frequency excitation. This can be seen by observing that the electrostatic force is proportional to the square of the voltage waveform

$$\begin{aligned} F_{es} \propto V(t)^2 &= (V_{dc} + V_{ac}\cos(\Omega t))^2 \\ &= V_{dc}^2 + 2V_{dc}V_{ac}\cos(\Omega t) + \frac{1}{2}V_{ac}^2 - \frac{1}{2}V_{ac}^2\sin(2\Omega t) \\ &= (V_{dc}^2 + \frac{1}{2}{V_{ac}}^2) + 2V_{dc}V_{ac}\cos(\Omega t) - \frac{1}{2}V_{ac}^2\sin(2\Omega t) \end{aligned} \tag{3.38}$$

Equation (3.38) shows that the electrostatic force consists of a static component proportional to $V_{dc}^2 + \frac{1}{2}V_{ac}^2$, a lower harmonic component at Ω proportional to $2V_{dc}V_{ac}$, and a higher harmonic component at 2Ω proportional to $\frac{1}{2}V_{ac}^2$. The higher harmonic excites primary resonance when the signal frequency is at $\Omega = \frac{1}{2}\omega_{\circ b}$. The lower harmonic excites primary resonance when the signal frequency is at $\Omega = \omega_{\circ b}$.

Table 3.3 shows the relative values of the electrostatic force lower and higher harmonic components for the voltage waveforms used in Fig. 3.14. As V_{ac} increases the excitation level of both components increase which amplifies the response at the signal frequencies $\Omega = \frac{1}{2}\omega_{\circ b}$ and $\Omega = \omega_{\circ b}$. The peak observed at $\Omega = \frac{1}{2}\omega_{\circ b}$ is due to primary resonance of the higher harmonic component while that observed at $\Omega = \omega_{\circ b}$ is due to primary resonance of the lower harmonic component. We note that the lower harmonic component for the waveform with $V_{ac} = 2\mathrm{V}$ has a similar magnitude to that of the higher harmonic component for the waveform with $V_{ac} = 4\mathrm{V}$.

Fig. 3.14 shows that the response of the lower harmonic at $\Omega = \omega_{\circ b}$ in the first case is similar in size to that of the higher harmonic at $\Omega = \frac{1}{2}\omega_{\circ b}$ in the second case. Further, comparison of Figs. 3.14 (a) and (b) to Figs. 3.13 (a) and (b) show the same effect for squeeze-film damping for variable dc and variable ac waveforms.

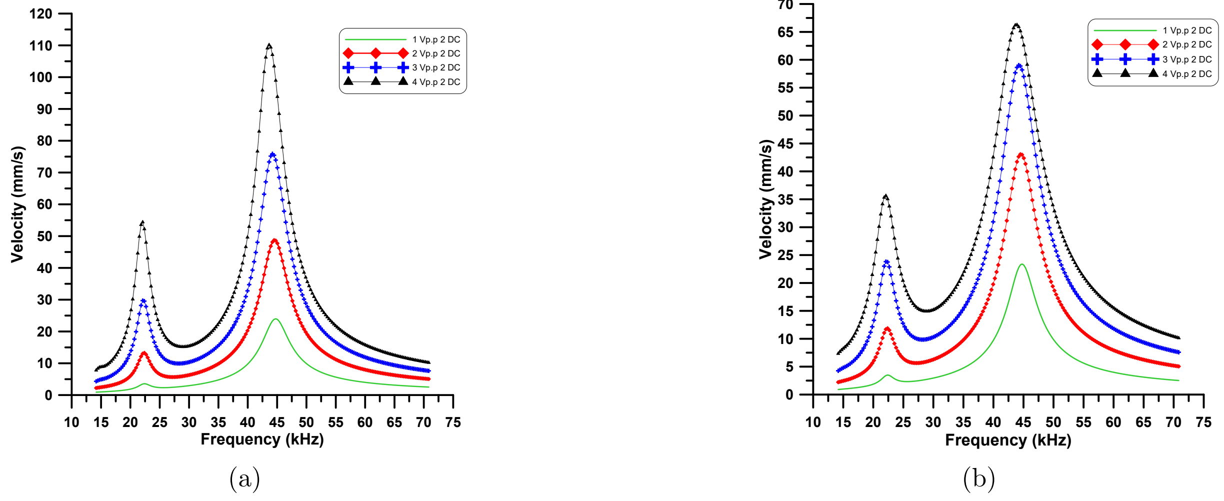

Figure 3.14: *The frequency-response curves of the actuator in the (a) absence and (b) presence of squeeze-film damping.*

Table 3.3: Electrostatic Force Components

V_{dc}	V_{ac}	Lower Harmonic $\propto 2V_{dc}V_{ac}$	Higher Harmonic $\propto \frac{1}{2}{V_{ac}}^2$
2	1	4	1/2
2	2	8	2
2	3	12	4.5
2	4	16	8

Chapter 4

Parameter Identification of the Electrostatic Actuator

We investigate the resonances of the electrostatic MEMS actuator and adopt a 1-DOF generalized Duffing oscillator model for the actuator and identify its parameters. Specifically, the primary, superharmonic of order-one-half, and subharmonic of order-two resonances of the actuator were experimentally investigated under direct electrostatic excitation. The experiments were conducted in soft vacuum by placing the actuator inside a vacuum chamber in order to reduce the effect of squeeze-film damping and amplify the response. The actuator response was measured using a laser vibrometer [62]. The model and the identified parameters were verified by comparing the velocity FFT predicted by the model to that obtained experimentally using a laser Doppler vibrometer[1].

4.1 Analytical Model

The actuator, described in section 3.1, is fabricated from polysilicon using the Poly2 layer in the PolyMUMPs fabrication process [54]. It features two support beams with nominal dimensions $125 \times 5 \times 1.5$ μm and an end microplate with the nominal dimensions $30 \times 60 \times 1.5$ μm as shown in Fig. 3.8(b). The beams are attached at the plate edges to maximize the torsional stiffness. Two gold pads are patterned at the roots of the support beams to

[1]Laser Doppler vibrometer :"a precision optical transducer used for determining vibration velocity and displacement at a fixed point. The technology is based on the Doppler-effect; sensing the frequency shift of back scattered light from a moving surface [62]."

apply a potential difference between the microplate and a substrate electrode at a distance d. A 3D scan of the actuator using a white light profilometer and schematic drawing are shown in Fig. 3.8(a).

The actuator is modeled as a 1-DOF lumped mass generalized Duffing oscillator. The model ignores the microplate inclination angle but accounts for the quadratic and cubic mechanical nonlinearities and the electrostatic force nonlinearity. The governing equation of motion is given by

$$m_{eq}\ddot{w} + (c_v + c_s)\dot{w} + k_{eq}w + k_2 w^2 + k_3 w^3 = \frac{\epsilon\ A\ V^2}{2(d-w)^2} \tag{4.1}$$

The quadratic and cubic stiffness coefficients are denoted by k_2 and k_3, respectively. The inclusion of quadratic and cubic stiffnesses is meant to enhance the lumped model by accounting for inherent nonlinearities.

Assuming that the support beams are identical, the microplate is rigid, and the distributed electrostatic force is lumped at the center of the microplate, the boundary conditions at the end of the support beams can be described as combined electrostatic shear and moment. The linear stiffness of the beams k_{eq} can then be derived as given in Eq. (3.14). The equation of motion (4.1) can be nondimensionaled using the variables defined in Eq. (3.20), as follows:

$$\ddot{\hat{w}} + (\mu_1 + \mu_2)\dot{\hat{w}} + \hat{w} + \alpha_2 \hat{w}^2 + \alpha_3 \hat{w}^3 = \alpha\ \frac{V^2}{(1-\hat{w})^2} \tag{4.2}$$

where

$$\mu_1 = c_v \frac{T}{m_{eq}} \quad , \quad \mu_2 = c_s \frac{T}{m_{eq}} \quad , \quad \alpha\ = \frac{\epsilon\ A}{2\ d^3\ k_{eq}} \quad , \quad \alpha_2 = \frac{k_2}{k_{eq}} d \quad , \quad \alpha_3 = \frac{k_3}{k_{eq}} d^2 \tag{4.3}$$

Since, the actuator was tested inside a vacuum chamber, we ignore squeeze-film damping and set $\mu_2 = 0$. For the sake of succinctness, we dispense with the over-hat and rewrite the equation of motion as

$$\ddot{w} + \mu_1 \dot{w} + w + \alpha_2 w^2 + \alpha_3 w^3 = \alpha\ \frac{V^2}{(1-w)^2} \tag{4.4}$$

The excitation voltage was supplied via the vacuum chamber's electric feed-through. The velocity of the microplate center point was measured using the VD-200 velocity decoder of the vibrometer. First, the fundamental natural frequency of the actuator was

found utilizing white (thermal noise) excitation at a chamber pressure of 53 mTorr. The FFT of the actuator velocity in dB-scale is shown in Fig. 4.1. The fundamental natural frequency is identified from the figure as $f_{nb} = 32.8\,\text{kHz}$. The support beams width and the structural layer thickness are estimated as $b_b = 4.4\,\mu\text{m}$ and $h_b = 1.15\,\mu\text{m}$, respectively, by matching the fundamental natural frequency of the model ($\sqrt{k_{eq}/m_{eq}}$) in the absence of an electrostatic field to the experimental value. The resulting effective linear stiffness and mass are $k_{eq} = 0.2305\,\text{N/m}$ and $m_{eq} = 5.5\,\text{ng}$. The capacitor gap is maintained at the nominal value $d = 2\ \mu\text{m}$.

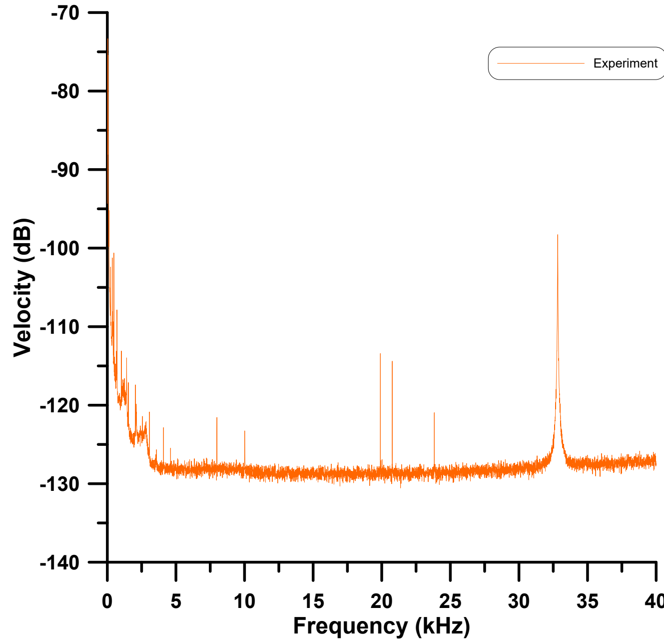

Figure 4.1: *The FFT of the actuator's velocity under thermal noise excitation and chamber pressure of* 53 *mTorr.*

Using the actuator's dimensions that have been identified, first six mode shapes and natural frequencies were obtained using FEM package described above as shown in Fig. 4.2. The mode shapes are (a) first out-of-plane bending mode, (b) first torsional mode, (c) first in-plane bending mode, (d) second out-of-plane bending mode, (e) second torsional mode, and (f) third out-of-plane bending mode.

Next, the actuator dynamic response was investigated under primary, subharmonic, and superharmonic excitations. The excitation signal, Eq. (3.36), was set to $V_{dc} = 500$

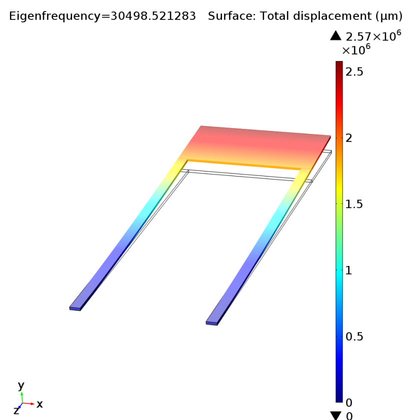

(a)

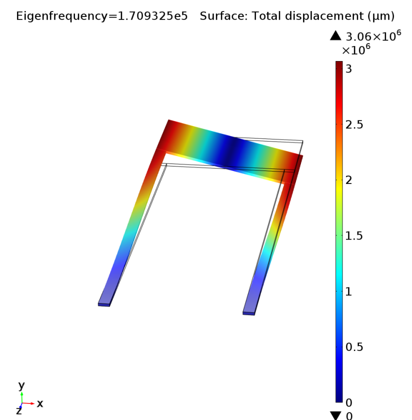

(b)

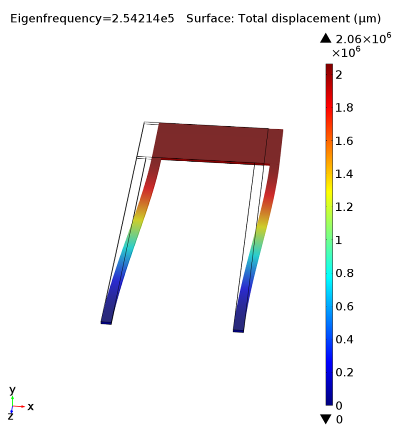

(c)

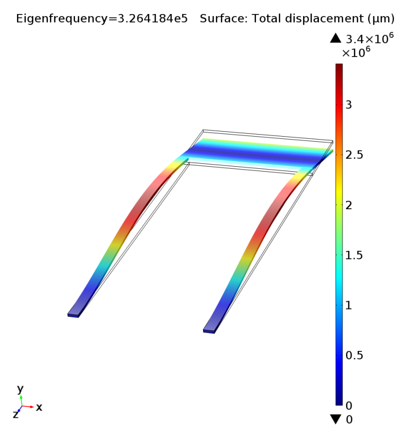

(d)

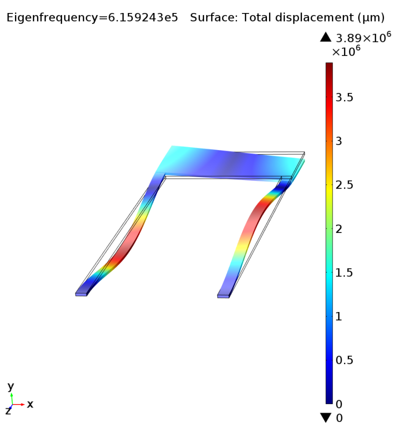

(e)

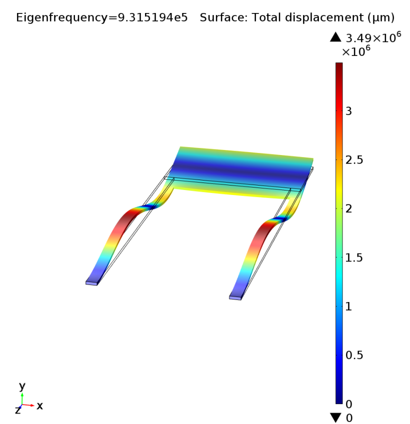

(f)

Figure 4.2: *The first six mode shapes and natural frequencies of the actuator obtained from FEM.*

mV and $V_{ac} = 500$ mV and the frequencies $\Omega = \omega_{ob}$, $\Omega = \frac{1}{2}\omega_{ob}$, and $\Omega = 2\omega_{ob}$. The experimental results in each case were compared to the steady-state response of the model obtained numerically by integrating Eq. (4.4) for 4000 T_s, where

$$T_s = \frac{2\pi}{\Omega}$$

is the signal period. A parameter identification technique was developed to estimate the actuator dimensions such that the differences between the numerical and experimental steady-state responses were minimized. The parameter identification technique is based on the actuator's parameters estimation that produce the same experimental results.

Because the experimental measurements contain noise, two sources of noise were introduced into the model. Process noise was added to the actuation signal

$$V(t) = V_{dc} + V_{ac}\cos(\Omega t) + S_v\sqrt{BW_v} \tag{4.5}$$

where S_v is the noise spectral density and BW_v is the bandwidth of the actuation signal. It accounts for electrical noise in the excitation signal which has a particular influence on the actuator response near resonance. Measurement noise was added to the model predicted velocity $\dot{w}$ to reproduce the experimentally measured velocity

$$\bar{\dot{w}} = \dot{w} + S_m\sqrt{BW_m} \tag{4.6}$$

where S_m is the noise spectral density and BW_m is the bandwidth of the detection signal. The laser Doppler vibrometer sampling rate was limited to 256 k sample/s and the measurement noise bandwidth was set to $BW_m = 100$ kHz.

4.2 Primary Resonance

As a first step to understanding the system dynamics, the actuator was excited in the vicinity of primary resonance of the first out-of-plane bending mode at $f_{nb} = 32.8$ kHz. The resulting electrostatic force is composed of a lower harmonic component at $\Omega = \omega_{nb}$ with an amplitude ($\propto 1/2$) and a higher harmonic component at 2Ω with an amplitude ($\propto 1/4$). The FFT of the actuator's velocity was evaluated using the vibrometer's software PSV[2]. It is shown as the blue diamonds in Fig. 4.3. Three distinct peaks are clearly seen in the FFT at the first, second, and third harmonics of the excitation signal Ω, 2Ω, and 3Ω, respectively.

[2]Polytec Scanning Vibrometers (PSV) is a measurement software.

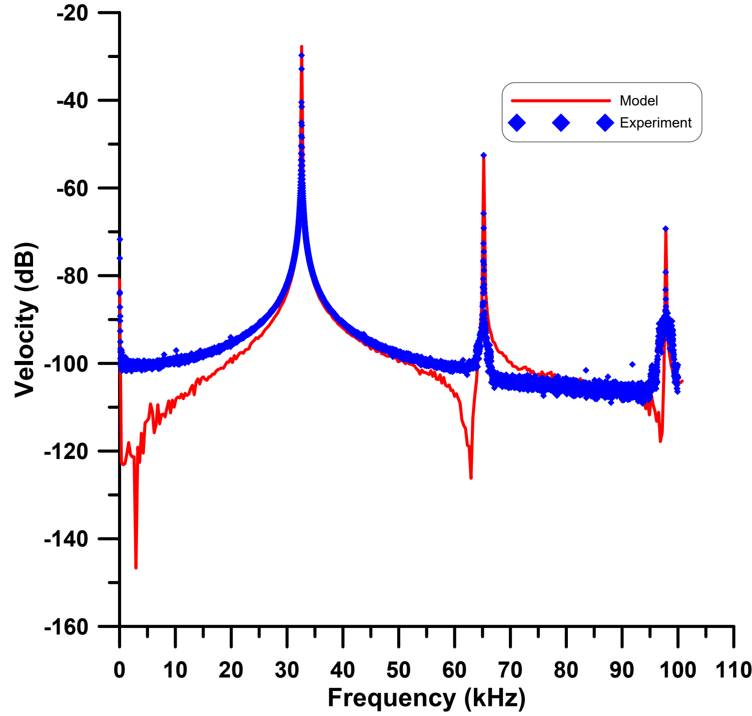

Figure 4.3: *Model predicted (solid red line) and experimental (blue $\diamond$) FFTs of the actuator velocity under primary resonance excitation $f = 32.8\,kHz$.*

The experimental measurement noise spectral density S_m was calculated from the experimental FFT using the formula [42]:

$$S_m = \frac{1}{q-p+1} \sum_{i=p}^{q} \dot{w}_i(f) \tag{4.7}$$

where $\dot{w}_i(f)$ is velocity in dB-scale and p and q are the FFT bin numbers limiting a region in the frequency spectrum away from resonances where the average spectral density is obtained. It represents the noise floor of the experimental FFT. We calculated $S_m = 5.7727\,\mu\text{m/s}/\sqrt{Hz}$ over the frequency range $[68, 80]\,\text{kHz}$. Measurement noise dominates the response in this frequency range as can be observed in Fig. 4.3.

The FFT of the numerically predicted velocity $\dot{w}$ was obtained from the last 400 signal periods in the time-history of the velocity $\dot{w}$. It is shown by the red line in Fig. 4.3. The values of the quadratic and cubic nonlinearities were estimated using the parameters

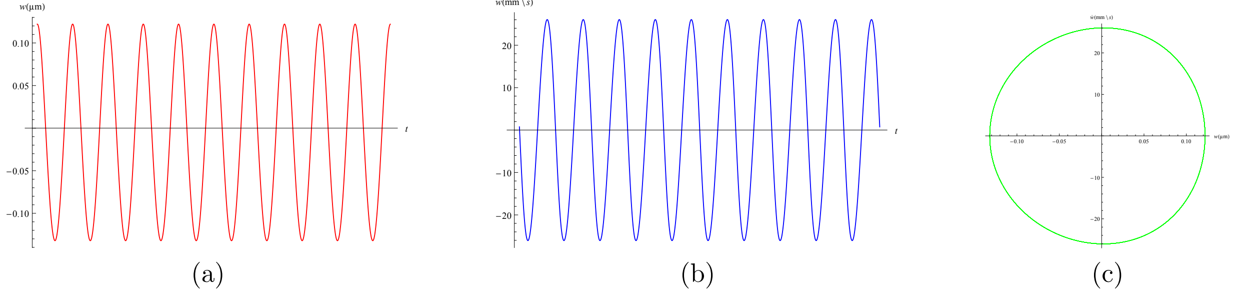

(a) (b) (c)

Figure 4.4: *Model predicted time-histories of the: (a) displacement, (b) velocity and (c) corresponding phase portrait under primary resonance,* $f = 32.8\,kHz$.

identification technique to match the locations of the second and third harmonic peaks in the model predicted FFT to that obtained experimentally. They were found to be $k_2 = 3.23$ N/m^2 and $k_3 = 0.189$ N/m^3.

The placement of the actuator inside the vacuum chamber elevated its quality factor which was estimated at $Q = 1300$ by matching the half-power bandwidth of the peaks in the experimental and numerically predicted FFTs, Fig. 4.3. Typically, the actuator settles down to steady-state response within a time period Q T$_n$, where T_n is the natural period. Our estimate of the quality factor is, therefore, consistent with our assumption that the actuator settles down to steady state response at $t = 3600T_s$.

To match the peak values of experimental and predicted FFTs, the process noise spectral density was set to $S_v = 0.063$ V $/\sqrt{Hz}$ over a bandwidth of $BW_v = 32.8\,$kHz. A measurement noise of $S_m =$ -104.278 dB $/\sqrt{Hz}$ was added to the model predicted velocity to match the skirt and noise floor of the experimental and predicted FFTs. The spectral density of the measurement noise was calculated from the model predicted FFT, Fig. 4.3, using Eq.(4.7) over the frequency range $[68, 80]$ kHz as $S_m = 6.13\,(\mu\text{m/s})/\sqrt{Hz}$. We note that the addition of measurement noise to the model allowed the predicted FFT to match the skirt of the peaks at Ω, 2Ω, and 3Ω and the noise floor of the experimental FFT. The close agreement between the experimental and model predicted FFTs in the vicinity of the peaks indicates that a generalized Duffing oscillator model, process noise, and the proposed identification procedure are adequate to capture the large-amplitude motions of the electrostatic actuator. On the other hand, it is necessary to include measurement noise in the model to capture the small-amplitude motions (away from resonances) of the actuator.

The time-histories of the microplate center displacement w and velocity $\dot{w}$ were calculated numerically by integrating Eq. (4.4) for $20000\,T_s$ to better reflect the steady-state

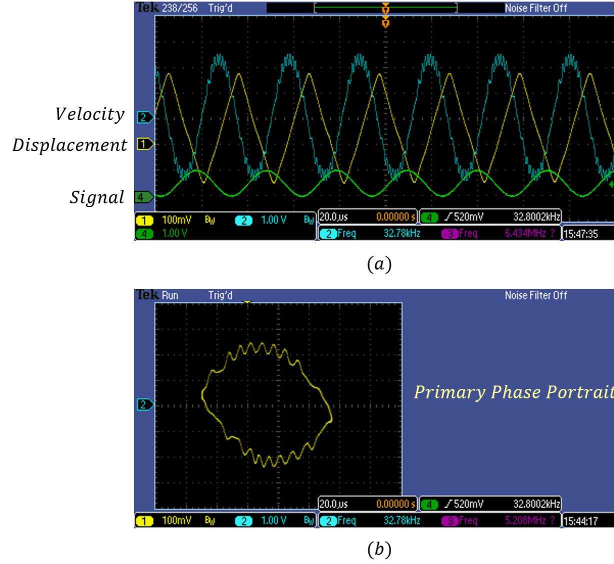

Figure 4.5: *(a) The experimental time-histories of the displacement (yellow line) and velocity (blue line) and (b) the corresponding phase portrait of the actuator captured from the oscilloscope under primary resonance,* $f = 32.8\,kHz$*.*

response. The last 10 signal periods of those time-histories are shown in Fig. 4.4(a) and (b), respectively. They were also measured optically using a laser Doppler vibrometer as shown in Fig. 4.5(a). The corresponding phase portraits are shown Figs. 4.4(c) and 4.5(b). The experimental results contain evidence of a significant response at the fifteenth harmonic of the natural frequency $15\omega_{nb}$ as shown in Fig. 4.5(b).

The FFT of the experimentally measured velocity, Fig. 4.6 , shows evidence of a 'mode' at $f_m = 490\,\text{kHz}$ and harmonics at $f_m + pf_{nb}$, where p is an integer, representing interaction between that mode and the fundamental mode. The peaks observed at even-valued p are significantly larger than those at odd-valued p. This is expected since the quadratic nonlinearity is stronger than the cubic nonlinearity. However, examining the first five modes of the actuator obtained from the FEM simulation, Fig. 4.2, produces no modes in that frequency range. Resolving this response requires further investigation in future work.

To investigate the dynamic response of the actuator, we subjected it to a frequency sweep test in the primary resonance regime. The excitation force was kept constant at ($V_{dc} = 500\,\text{mV}$ and $V_{ac} = 500\,\text{mV}$) while the excitation frequency was swept up and down the frequency range $[30.75, 33.8]\,\text{kHz}$. To obtain the frequency response curve, Eq. (4.4)

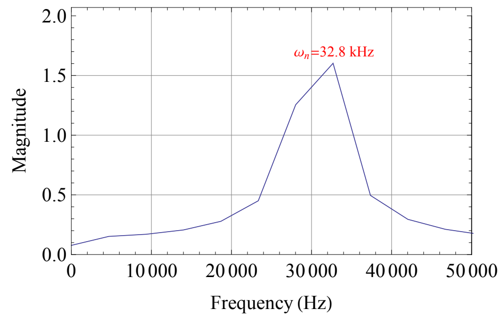

(a)

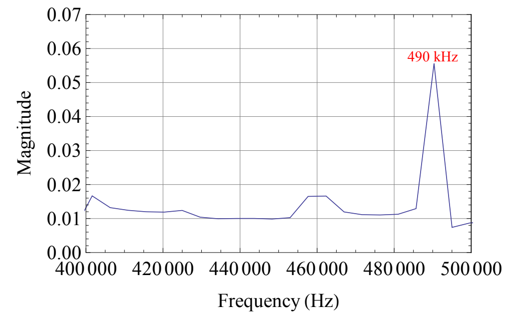

(b)

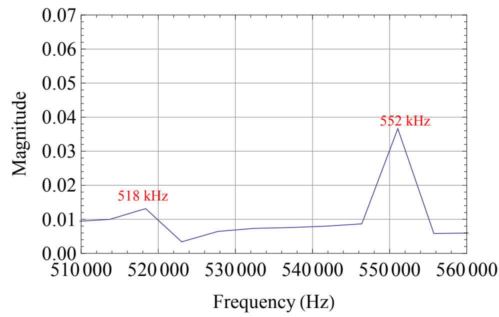

(c)

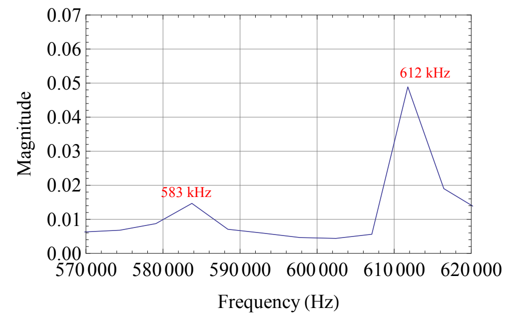

(d)

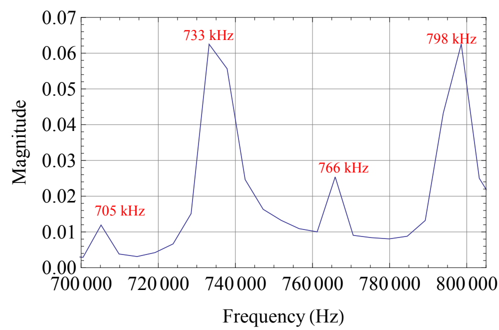

(e)

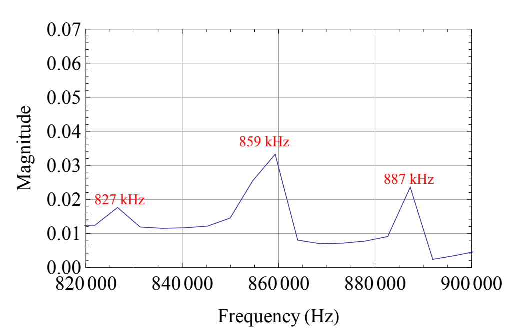

(f)

Figure 4.6: *FFT of the experimentally measured velocity at the primary resonance* $f = 32.8\,kHz$.

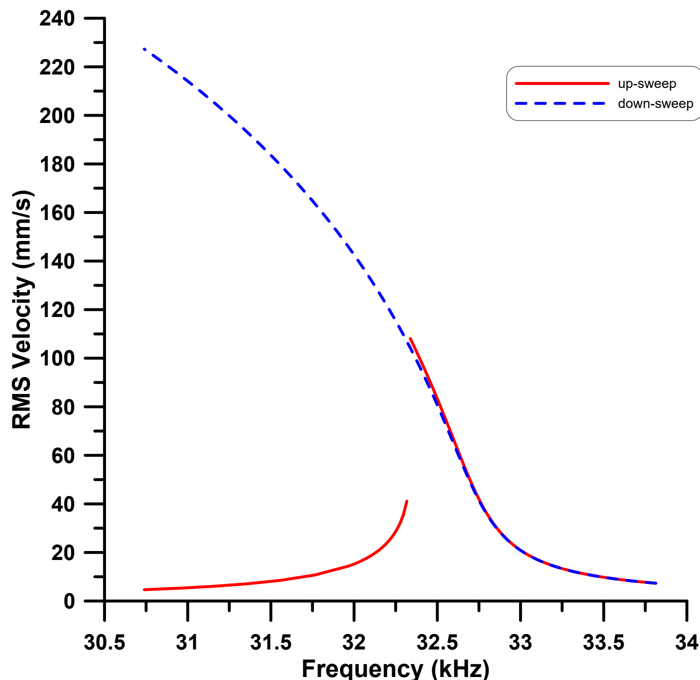

Figure 4.7: *The predicted frequency-response curve of the electrostatic actuator near primary resonance. Forward sweep in blue line and backward sweep red dashed line.*

was numerically integrated over a long-time period ($20000\,T_s$). The root-mean square (RMS) of the velocity was then evaluated over the last 100 signal periods to represent the steady-state response.

The frequency up-sweep is shown in red lines and the frequency down-sweep is shown in a dashed blue line in Fig. 4.7. Two branches of stable orbits appear in the frequency-response curve. The lower (left) branch terminates in a cyclic-fold bifurcation at $f = 32.33\,$kHz where the response jumps to the upper branch during a frequency up-sweep. The close agreement between the up and down sweeps along the upper branch shows that the numerical procedure described above is effective in approaching steady-state. The response on the upper (right) branch continues to grow as the frequency is swept-down. This is an artifact due to the absence of nonlinear damping in the model [63]. Results along this branch were arbitrarily limited to the lower-end of the frequency range of interest $f = 30.75\,$kHz. The increase in the response size for frequencies below the natural frequency ω_{nb} indicates a softening-type nonlinearity as noted by Younis [6]. Due

to the model limitations, it is not possible to comment on the size of the region in the frequency domain where co-existing responses (solutions) are present.

4.3 Superharmonic Excitation

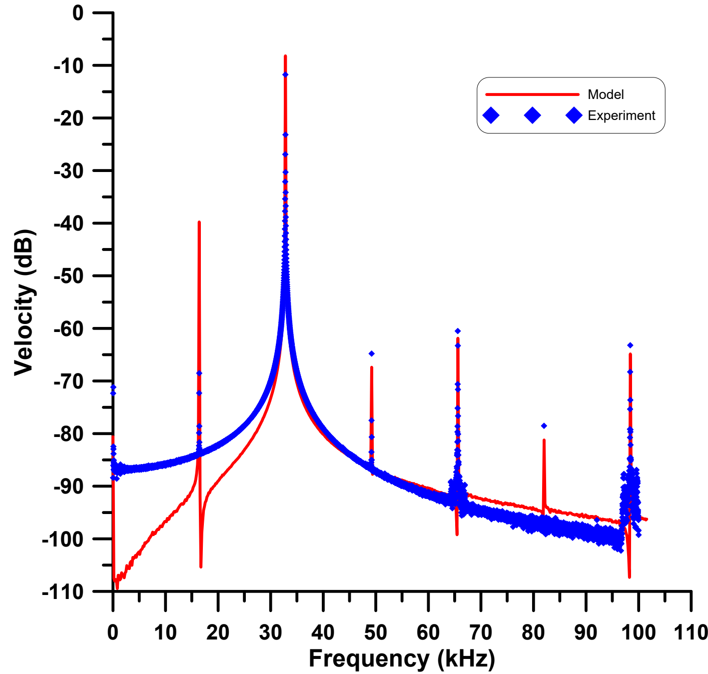

Figure 4.8: *Model predicted (solid red line) and experimental (blue ⋄) FFTs of the actuator velocity under superharmonic resonance, $f = 16.4\,kHz$.*

The same experimental procedure used for primary resonance was employed to investigate the superharmonic resonance. The FFT of the microplate center velocity $\dot{w}$ was obtained experimentally using the vibrometer for an excitation force of $V_{dc} = 500\,\text{mV}$ and $V_{ac} = 500\,\text{mV}$ and an excitation frequency of $\Omega = \frac{1}{2}\omega_{nb} = 16.4\,\text{kHz}$. The FFT marked by blue diamonds in Fig. 4.8 demonstrates evidence of superharmonic resonance of order two with peaks appearing at $\frac{1}{2}\Omega$, Ω, $\frac{3}{2}\Omega$, 2Ω, $\frac{5}{2}\Omega$, and 3Ω. We calculated the measurement noise spectral density of the experimental FFT as $S_m = 16.3038\ \mu\text{m/s}/\sqrt{Hz}$ from the noise floor of the experimental FFT observed in the frequency range $[68, 80]\,\text{kHz}$. The measurement frequency bandwidth was set $BW_m = 100\,\text{kHz}$.

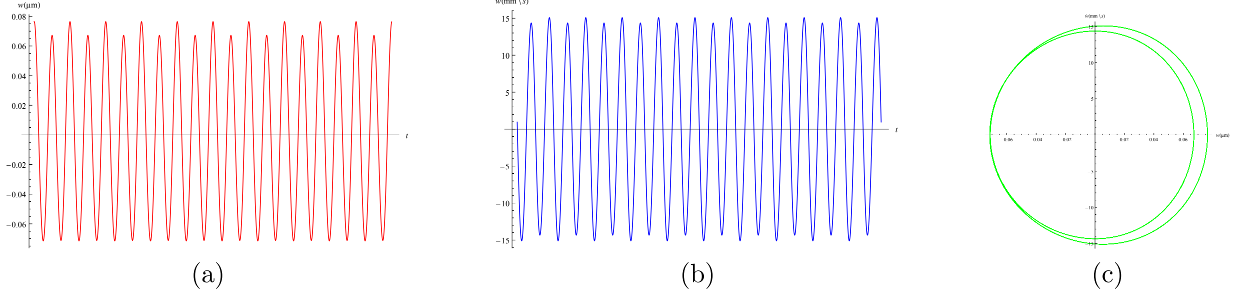

Figure 4.9: *The model predicted time-histories of the: (a) displacement, (b) velocity and (c) corresponding phase portrait under superharmonic resonance,* $f = 16.4\,kHz$*.*

The FFT of the numerically predicted velocity $\dot{w}$ was obtained by numerically integrating the equation of motion, Eq. (4.4), for $4000\,T_s$ and using the time-history in the last 400 signal periods. It is shown by the red line in Fig. 4.8. The same parameter values identified above were used in this case.

Close matching is observed between the experimental and model predicted FFTs except in the vicinity of $\frac{1}{2}\omega_{nb}$. In order to match the peak values of the model and experimental FFTs, we added a process noise of $S_v = 0.064\mathrm{V}/\sqrt{Hz}$ to the model excitation signal. Further, to match the skirt and noise floor of the model and experimental FFTs, we added a measurement noise of $S_m = -93.16\,\mathrm{dB}/\sqrt{Hz}$ to the model predicted velocity. The spectral density of the measurement noise was calculated in the model predicted FFT using Eq.(4.7) over the frequency range $[68, 80]$ kHz as $S_m = 21.97\,(\mu m/s)/\sqrt{Hz}$.

The time-histories of the microplate center displacement w and velocity $\dot{w}$ were calculated numerically by integrating Eq. (4.4) for $20000\,T_s$. Figs. 4.9 (a) and (b) show the last ten signal periods ($10T_s$) of the displacement and velocity time-histories, respectively. The sequence of a large oscillation followed by a slightly smaller oscillation is due to a combination of superharmonic resonance driven by the lower harmonic component ($\propto 1/2$), with a period T_s, and primary resonance driven by the higher harmonic component ($\propto 1/4$) of the excitation force, with a period $\frac{1}{2}T_s$. The time-histories were also measured optically using a laser Doppler vibrometer as shown in Fig. 4.10(a). The corresponding predicted and measured phase portraits are shown in Figs. 4.9(c) and 4.10(b), respectively. The two loops observed in the phase portrait are evidence of a superharmonic resonance of order two. Further the experimental results contain evidence of a significant response at the 32nd harmonic $32\omega_{nb}$ of the signal as shown in Fig. 4.10(b).

The FFT of the experimentally measured velocity, Fig. 4.11 , shows evidence of modal

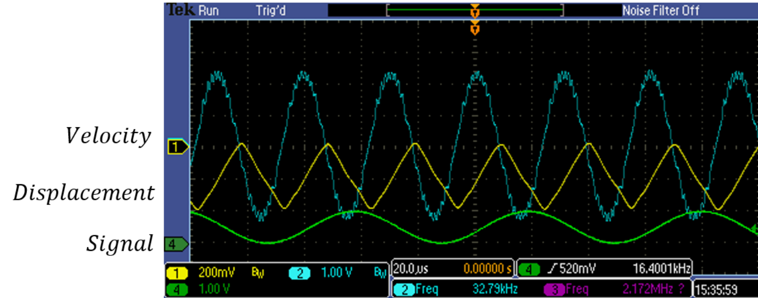

(*a*)

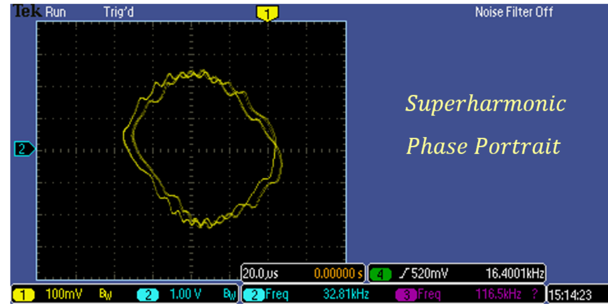

(*b*)

Figure 4.10: *(a) The experimental time-histories of the displacement (yellow line) and velocity (blue line) and (b) the corresponding phase portrait of the actuator captured from the oscilloscope under superharmonic resonance,* $f = 16.4\,kHz$*.*

interaction between a 'mode' at $f_m = 490\,\text{kHz}$ and the fundamental mode at f_{nb} indicated by harmonics at $f_m \pm p f_{nb}$, where p is an integer. This is consistent with the results for primary resonance described above.

The frequency-response curve of the actuator in the frequency range $[14.5, 18.5]\,\text{kHz}$ was created following the procedure described above. Fig. 4.12 shows two branches of response, lower and upper, and two cyclic-fold bifurcations in the frequency-response curve. One bifurcation is encountered along the lower branch during frequency up-sweep at $f = 16.25\,\text{kHz}$. It results in a jump to the upper branch. The other bifurcation is encountered in frequency down-sweep along the upper branch at $f = 15.41\,\text{kHz}$. It results in the response jumping down to the lower branch. As a result, hysteresis and multi-valuedness exist in the frequency range $[15.41, 16.25]\,\text{kHz}$ between the two bifurcation points. The upper branch terminates in a nonlinear resonance peak, unlike the case of primary resonance.

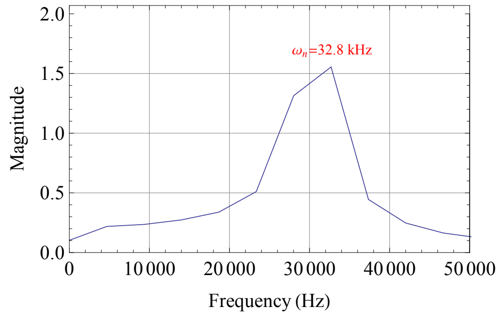

(a)

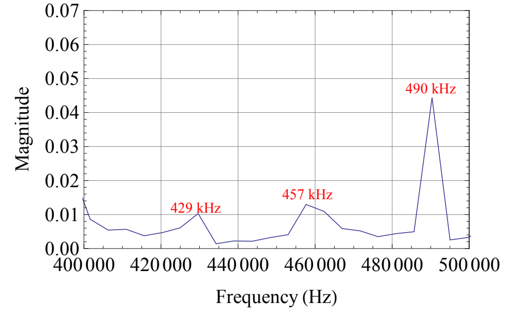

(b)

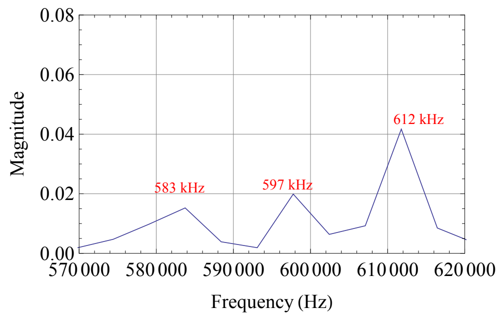

(c)

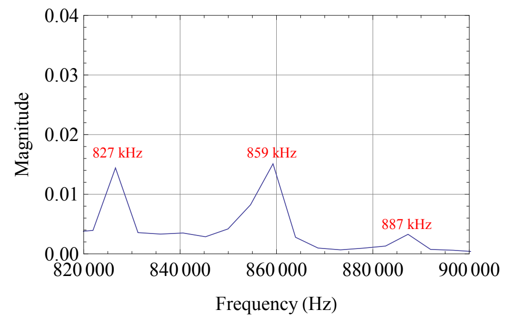

(d)

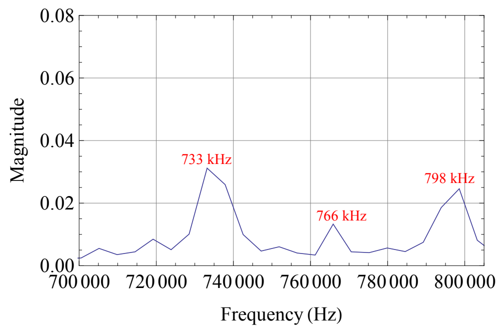

(e)

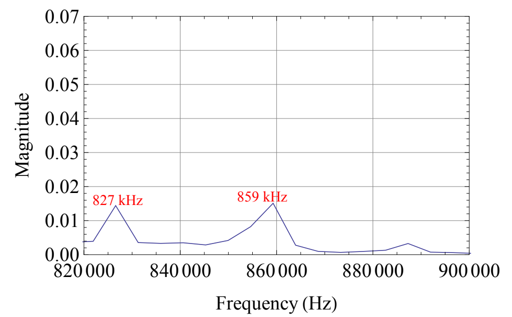

(f)

Figure 4.11: *FFT of the experimentally measured velocity at the superharmonic resonance* $f = 16.4\,kHz$.

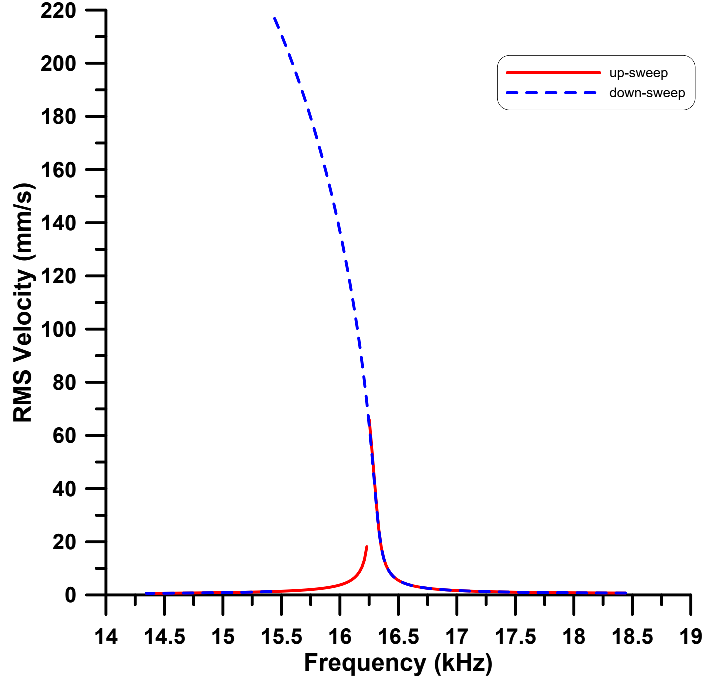

Figure 4.12: *The predicted frequency-response curve of the electrostatic actuator near superharmonic resonance. Forward sweep in blue line and backward sweep red dashed line.*

4.4 Subharmonic Excitation

The same experimental procedure was repeated to observe subharmonic resonance with a signal frequency of $f = 2f_{nb} = 65.6\,\text{kHz}$. The FFT of the microplate center velocity was obtained experimentally using the vibrometer and is shown by the blue diamond symbols in Fig. 4.13. The peaks appearing at Ω, 2Ω, and 3Ω are typical to the subharmonic resonance of order one-half. In addition, peaks are also observed at $\frac{1}{2}\Omega$, $\frac{3}{2}\Omega$, and $\frac{5}{2}\Omega$. We calculated the measurement noise spectral density of the experimental FFT as $S_m = 32.88\,(\mu m/s)/\sqrt{Hz}$ from the noise floor observed in the frequency range $[68; 80]$ kHz. The measurement frequency bandwidth was set $BW_m = 100\,\text{kHz}$. The FFT of the numerically predicted velocity $\dot{w}$ was obtained by numerically integrating Eq. (4.4) for 4000 T_s and using the time-history in the last 400 signal periods. It is shown by the red line in Fig. 4.13. The model parameters identification technique identified above were used in this case also except

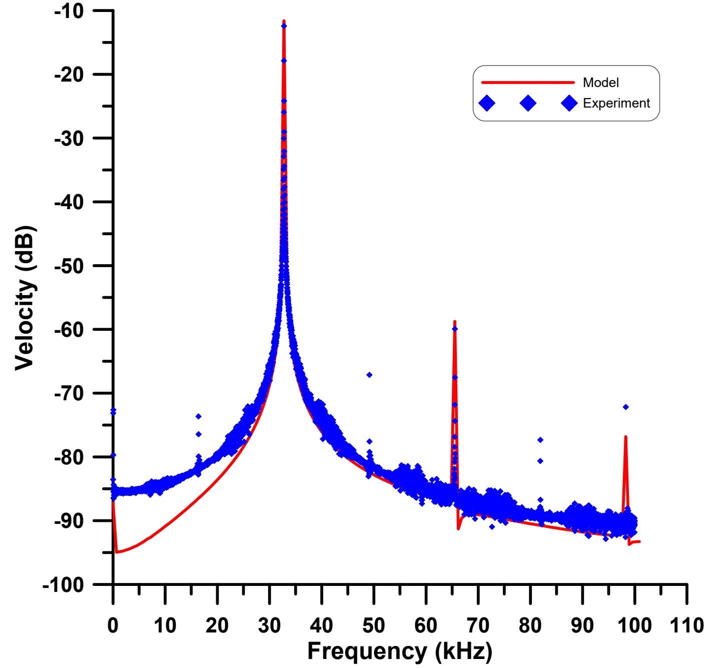

Figure 4.13: *The model predicted (solid red line) and experimental (blue $\diamond$) FFTs of the actuator velocity under subharmonic resonance excitation $f = 65.6\,kHz$.*

for the quadratic and cubic stiffness coefficients which were set to $k_2 = 0.1865$ N/m^2 and $k_3 = 0.1202$ N/m^3 to activate the subharmonic resonance and to match the peaks of the predicted and experimental FFTs. We note that the impact of the quadratic nonlinearity on the resonant peak at $\Omega = \omega_{nb}$ was more prominent than that of the cubic nonlinearity. The peaks at $\frac{1}{2}\Omega$, $\frac{3}{2}\Omega$, and $\frac{5}{2}\Omega$ are not present in the model predicted FFT.

To match the peak values of the experimental and model predicted FFTs, the spectral density of process noise was set in the model to $S_v = 0.062\,\text{V}\ /\sqrt{Hz}$ over a bandwidth of $BW_v = 65.6\,\text{kHz}$. We also added to the predicted velocity a measurement noise of S_m = -87.8 dB $/\sqrt{Hz}$. The spectral density of the measurement noise was calculated from the model predicted FFT using Eq.(4.7) over the frequency range $[68, 80]\,\text{kHz}$ as $S_m = 40.76\,\mu\text{m/s}/\sqrt{Hz}$. A good match is achieved between the model predicted and experimental FFTs at the integer harmonics Ω, 2Ω, and 3Ω but the harmonics $\frac{1}{2}\Omega$, $\frac{3}{2}\Omega$, and $\frac{5}{2}\Omega$ are absent from the model response and require more investigation.

The time-histories of the microplate center displacement w and velocity $\dot{w}$, Fig. 4.14 (a)

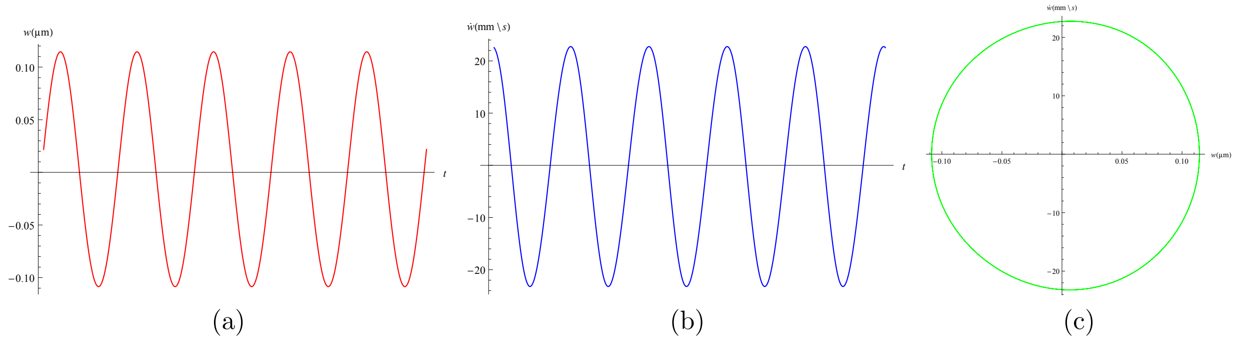

Figure 4.14: *The model predicted time-histories of the: (a) displacement , (b) velocity and (c) the corresponding phase portrait under subharmonic resonance, $f = 65.6\,kHz$.*

and (b), were calculated numerically using the same technique described above. The figures show the last ten signal periods ($10T_s$) of the displacement and velocity time-histories, respectively. The appearance of five periods only in the time-histories is evidence that the lower harmonic component, with a period T_s, has activated the subharmonic resonance of order one-half resulting in a resonant response with a period $2T_s$.

They time-histories were measured experimentally using a laser Doppler vibrometer as shown in Fig. 4.15(a). The corresponding predicted and measured phase portraits are shown in Fig. 4.14(c) and Fig. 4.15(b). The orbits appearing in the phase-portraits required two signal periods $2T_s$ to close, confirming the presence of subharmonic resonance of order one-half. Further the experimental results contain evidence of a significant response at the eighth harmonic of the signal 8Ω as shown in Fig. 4.15(b). Understanding this phenomenon requires further investigation in future work.

The FFT of the experimentally measured velocity, Fig. 4.16, shows evidence of a 'mode' at $f_m = 490\,\text{kHz}$ and harmonics at $f_m \pm p f_{nb}$, where p is an integer, representing interaction between that mode and the fundamental mode. This is consistent with the results for primary and superharmonic resonances reported above.

The frequency-response curve of the actuator in the frequency range $f = [65.35, 65.7]\,\text{kHz}$ was created following the procedure described above. Figure. 4.17 was constructed by a forward frequency-sweep (red lines) and a backward frequency-sweep (blue dashed line). Two branches of stable orbits appear in the frequency-response curve. During a frequency up-sweep, a cyclic-fold bifurcation occurs at $f = 65.132\,\text{kHz}$ where the response jumps from the lower left branch into the upper branch. Due to the absence of nonlinear damping in the model, the response on the upper branch continues to grow as the frequency

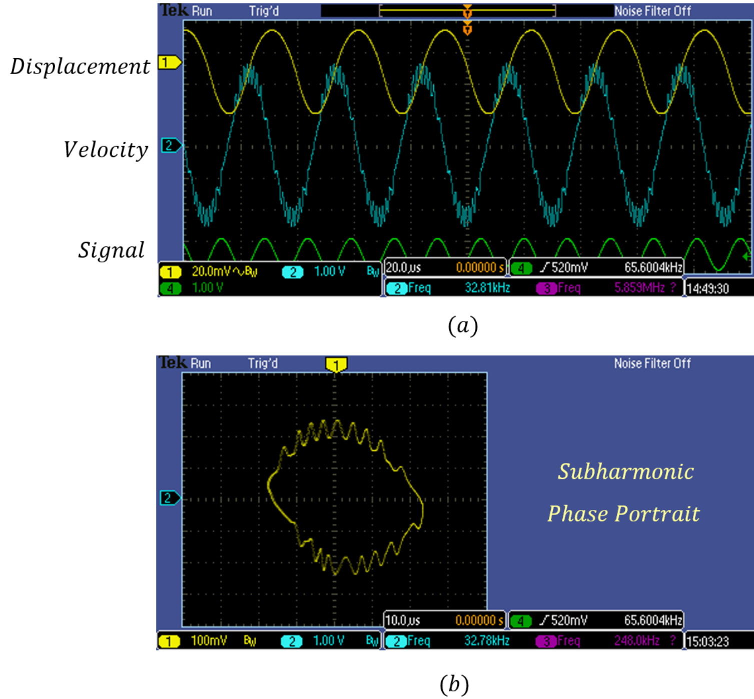

Figure 4.15: *(a) The experimental time-histories of the displacement (yellow line) and velocity (blue line) and (b) the corresponding phase portrait of the actuator captured from the oscilloscope under subharmonic resonance,* $f = 65.6\,kHz$.

is swept-down. A region of instability $[65.15, 65.24]\,\mathrm{kHz}$ appears between the ends of the lower left and right branches where the non-resonant (forced) response is unavailable.

4.5 Activation of Subharmonic Resonance

The appearance of subharmonic resonance requires the excitation force to exceed a threshold called the 'activation level'. Below this threshold, subharmonic resonance is not available and the branch of non-resonant responses is continuous, uninterrupted by instability. The electrostatic force with $V_{dc} = 500\,\mathrm{mV}$ and $V_{ac} = 500\,\mathrm{mV}$ ($V_{RMS} = 611.2\,\mathrm{mV}$) that was used in the previous section 4.4 was able to activate the subharmonic resonance of order one-half as shown in Fig. 4.13. In this section, we determine the actuator's activation level.

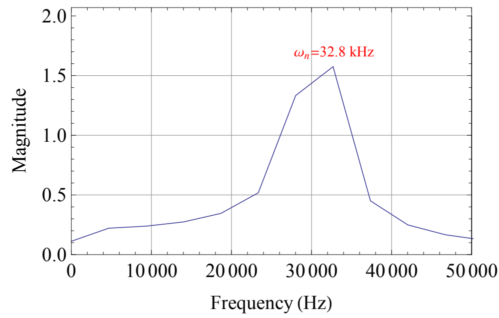

(a)

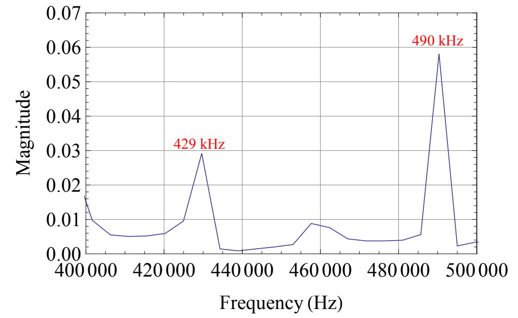

(b)

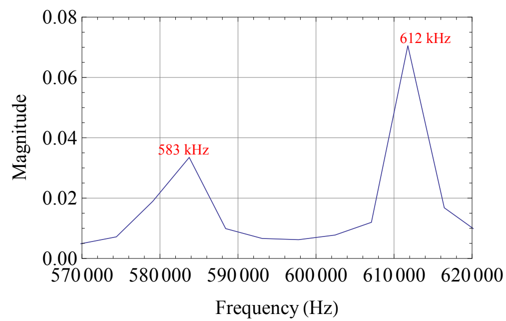

(c)

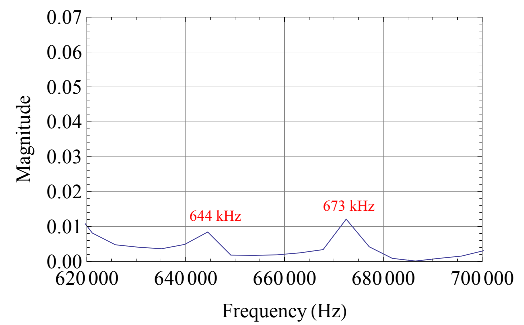

(d)

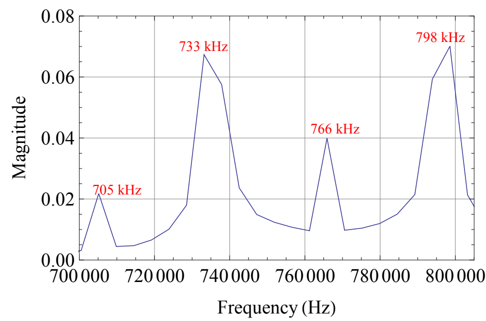

(e)

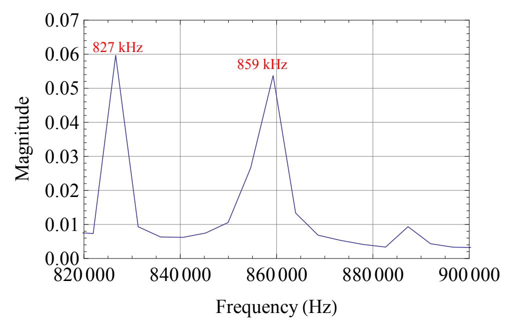

(f)

Figure 4.16: *FFT of the experimentally measured velocity at the subharmonic resonance* $f = 65.6\,kHz$

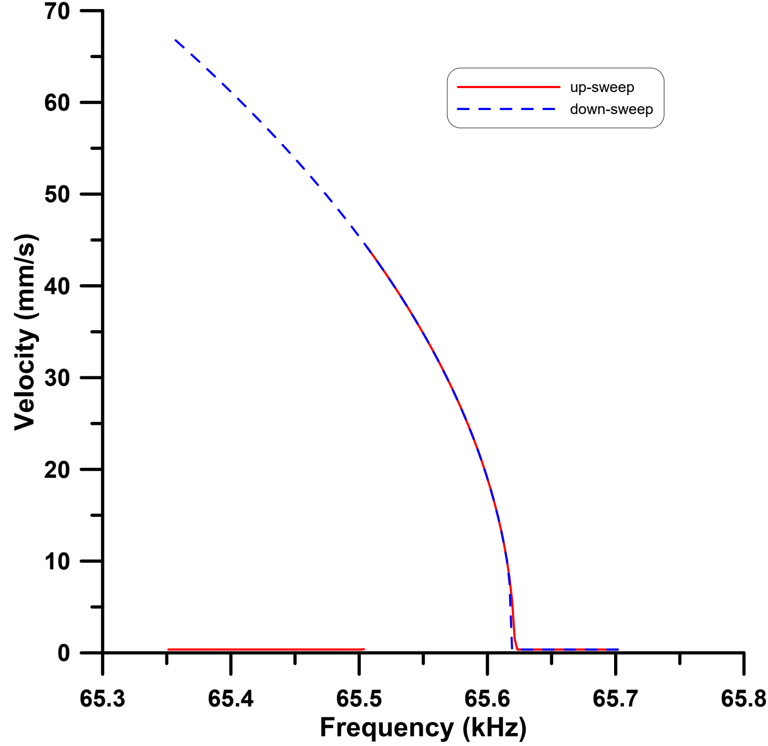

Figure 4.17: *The predicted frequency-response curve of the electrostatic actuator near subharmonic resonance. Forward sweep in blue line and backward sweep red dashed line.*

Since secondary resonances are a function of the system effective nonlinearity and the RMS of the actuation signal, we hold the RMS of the signal constant while reducing the amplitude of the lower harmonic of the excitation force until subharmonic resonance is deactivated. This is achieved by increasing V_{dc} and decreasing V_{ac} such that

$$\sqrt{V_{dc}^2 + \frac{1}{2}V_{ac}^2} = 611.2\,\text{mV}$$

Figures 4.18 show the FFTs of the actuator under an excitation frequency of $f = 2f_{nb} = 65.6\,\text{kHz}$ and $2V_{dc}V_{ac} = 500\,\text{mV}^2$, $433.6\,\text{mV}^2$, $415.8\,\text{mV}^2$, $393.95\,\text{mV}^2$, $363.52\,\text{mV}^2$, and $313.2\,\text{mV}^2$. Evidence of subharmonic resonance activation can be seen in Figs 4.18 (a), (b), (c), and (d) where energy is transmitted from the excitation frequency $\Omega = 2\omega_{nb}$ to the resonant frequency ω_{nb}. Subharmonic resonance is inactive in cases (e) and (f) and as a result no energy is present at ω_{nb}, Figs. 4.18 (e) and (f).

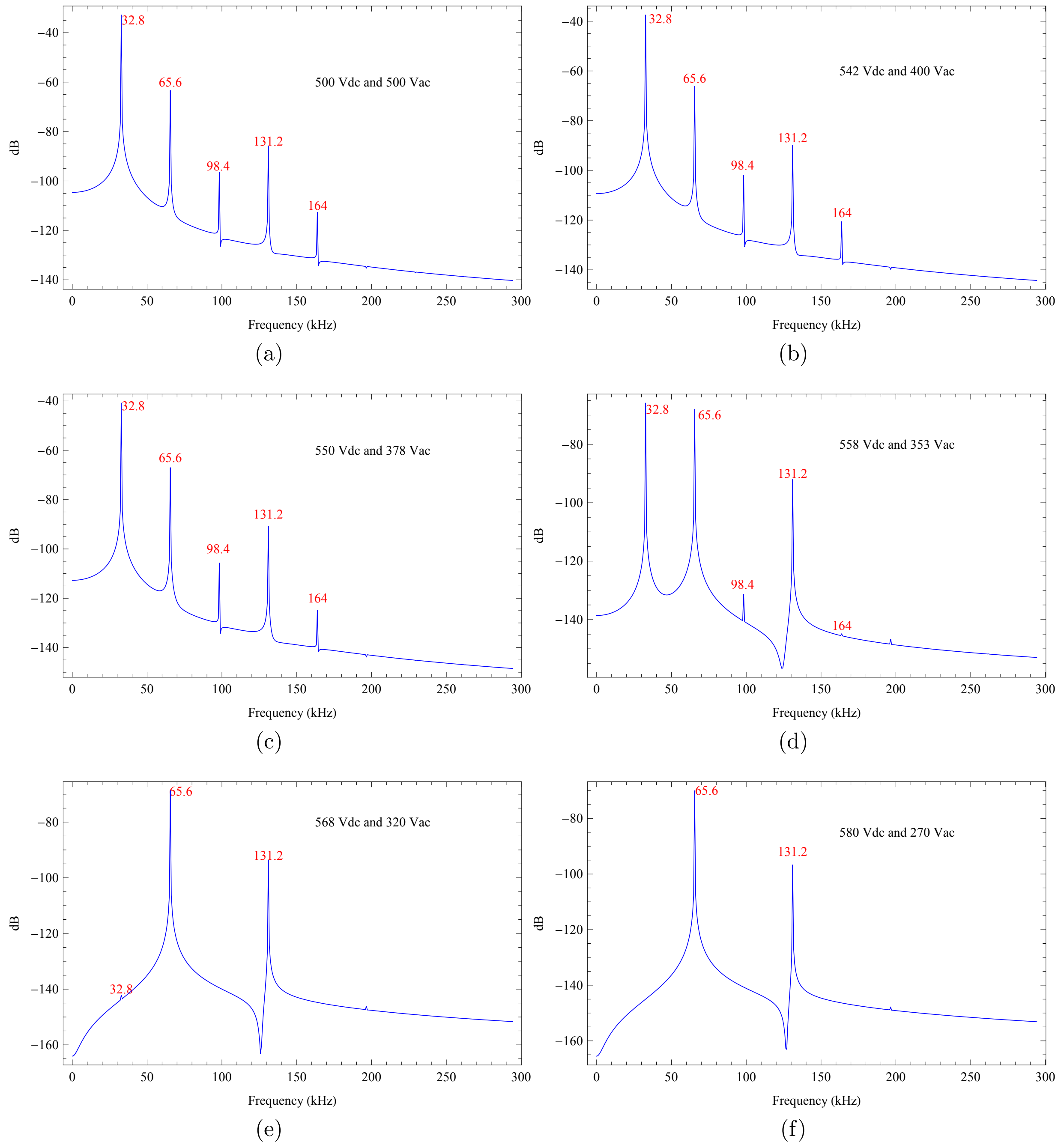

Figure 4.18: *The model predicted FFTs for* $\Omega = 2\omega_{nb}$ *and (a) 500* V_{dc} *and 500* V_{ac}*, (b) 542* V_{dc} *and 400* V_{ac}*, (c) 550* V_{dc} *and 378* V_{ac}*, (d) 558* V_{dc} *and 353* V_{ac}*, (e) 568* V_{dc} *and 320* V_{ac} *and (f) 580* V_{dc} *and 270* V_{ac}*.*

The frequency-response curves of the actuator in the frequency range $f = [65.35, 65.7]$ kHz were created following the procedure described above. Figure 4.17 was constructed from a frequency up-sweep (red lines) and a frequency down-sweep (blue dashed line). Two branches of non-resonant (small) stable orbits and one branch of resonant (large) stable orbits appear in the frequency-response curve. A subciritcal pitch-fork bifurcation occurs when the actuator response jumps from the stable lower left branch into the stable upper branch during a frequency up-sweep. The response on the upper branch continues to grow as the frequency is swept-down. This is a model artifact due to the absence of nonlinear damping.

A region of instability appears in the frequency-response curves between the ends of the lower left and right branches where the non-resonant (forced) response is unavailable. As we decrease the excitation amplitude $\propto 2V_{dc}V_{ac}$, the size of the instability region shrinks as shown in Figs. 4.19. In cases (a) to (d), the excitation frequency $\Omega = 2\omega_{nb}$ lies inside the instability region. However, it is outside that region in cases (e) and (f). The forcing level and the size of the instability region are listed on Table 4.1. The results indicate that once subharmonic resonance is activated, the response size grows fast with $2V_{dc}V_{ac}$ as shown in Fig. 4.19.

Table 4.1: Subharmonic Forcing Levels and the Instability Region

Case	$2V_{dc}V_{ac}$ (mV^2)	σ_1 (kHz)	σ_2 (kHz)	Instability Region (Hz)
a	500	65.503	65.623	119.54
b	433.6	65.514	65.613	100.99
c	415.8	65.516	65.610	94.81
d	393.95	65.520	65.606	86.56
e	363.52	65.524	65.602	78.32
f	313.2	65.534	65.58	59.77

The activation level of subharmonic resonance was derived for a generalized Duffing oscillator by Nayfeh [64]. He found that the trivial solution is stable if

$$\Gamma_2^2 F^2 < \omega_{nb}^2(\mu_1^2 + \frac{1}{4}\sigma^2) \tag{4.8}$$

Comparing our dimensional equation of motion Eq. (4.1) to Nayfeh's equation of motion, we obtain the following parameters:

$$F = \frac{\epsilon A V_{dc} V_{ac}}{2 m_{eq} d^2} \quad , \quad \Gamma_2 = \frac{2\alpha_2 + 3\omega_{nb}^2 \alpha_6}{6\omega_{nb}^2} \quad , \quad \mu_1 = \frac{\omega_{nb}}{2Q} \quad , \quad \alpha_6 = \frac{2}{d}$$

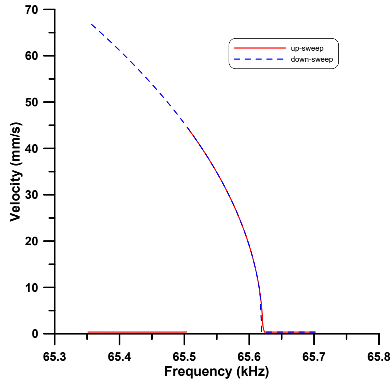

(a)

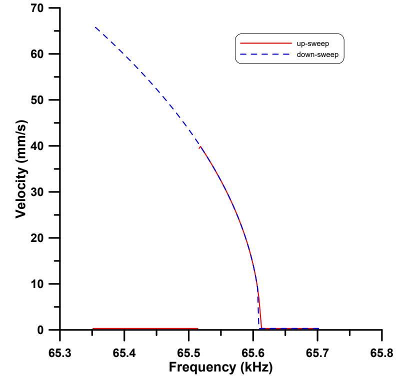

(b)

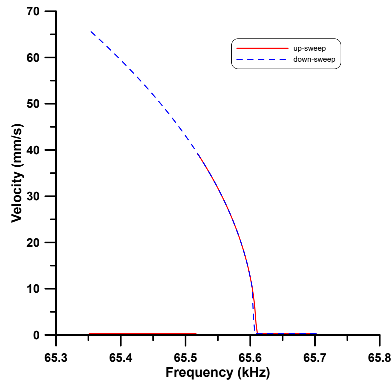

(c)

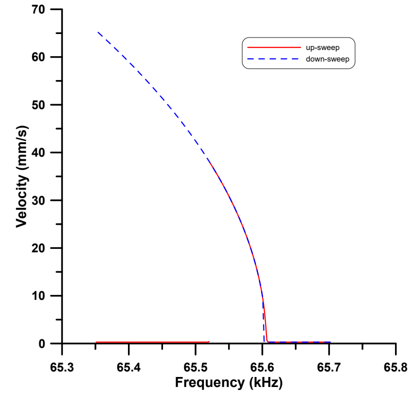

(d)

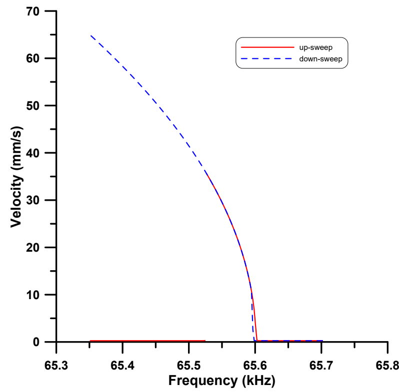

(e)

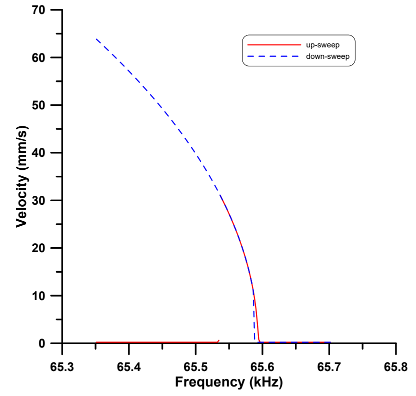

(f)

Figure 4.19: *Model predicted frequency-response curves for the waveforms: (a)* $V_{dc} = 500\,mV$ *and* $V_{ac} = 500\,mV$*, (b)* $V_{dc} = 542\,mV$ *and* $V_{ac} = 400\,mV$*, (c)* $V_{dc} = 550\,mV$ *and* $V_{ac} = 378\,mV$*, (d)* $V_{dc} = 558\,mV$ *and* $V_{ac} = 353\,mV$*, (e)* $V_{dc} = 568\,mV$ *and* $V_{ac} = 320\,mV$*, and (f)* $V_{dc} = 580\,mV$ *and* $V_{ac} = 270\,mV$*.*

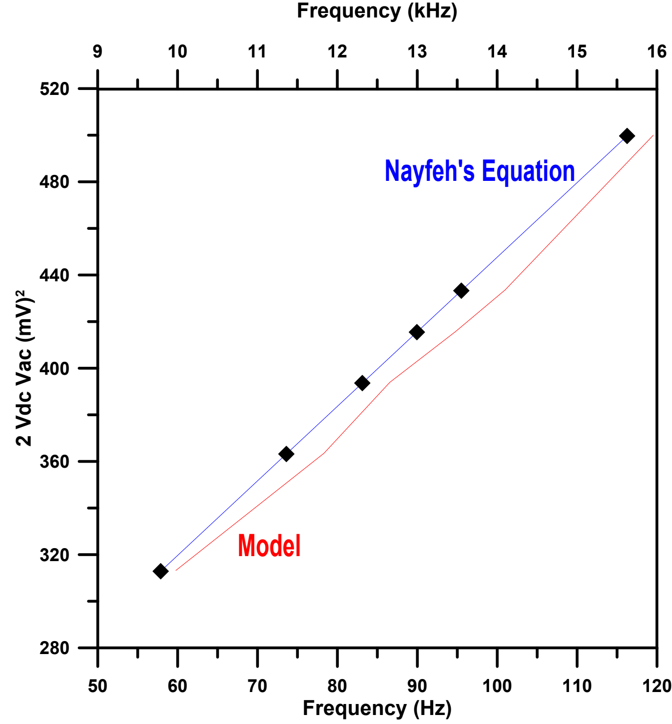

Figure 4.20: *The relationship between the forcing amplitude and the size of the trivial solution instability region.*

Then, Solving the resulting equation Eq. (4.8) for σ, we obtain

$$\sigma_{1,2} = \pm \frac{\sqrt{F^2\Gamma_2^2 - \mu_1^2\omega_{nb}^2}}{\omega_{nb}} \tag{4.9}$$

At the left and right-side edges of the instability region, σ_1 and σ_2, the left and right-hand sides of this inequality are identical. The relationship between the forcing amplitude $(2V_{dc}V_{ac})$ and the size of the trivial solution instability region $(\sigma_2-\sigma_1)$ obtained numerically from our model is shown in Fig. 4.20. However, using Nayfeh's equation, we obtain a large region of instability. The difference in both model need more investigation in the future. The results are a close to linear relationship in agreement with the equation derived above.

Chapter 5

Electrostatic/Electromagnetic MEMS Actuator

Combined microactuators have been used in some applications, such as micromirrors, micropumps, and switches. Implementing such devices with MEMS technology will produce larger strike mirrors and higher resolution displays [65]. In addition, a combined MEMS actuator could be used to produce both piston motion from linear excitation forces and torsional motion from excitation torque [66]. In this chapter, we introduce a novel two DOF MEMS actuator driven by electrostatic and electromagnetic forces. The actuator permits an increased in torsional motion with a low actuation voltage. A full analytical lumped-mass model is developed and the model predicted results are compared to the experimental results to verify the model validity.

5.1 The Actuator

The combined electrostatic/electromagnetic MEMS actuator consists of two substrate electrodes siting underneath a microplate supported by two cantilever beams as shown in Fig. 5.1. It is made of polysilicon using the PolyMUMPs fabrication process. The dimensions of the actuator are summarized in Table 3.1. It's material properties along are listed in Table 3.2.

The microactuator, illustrated in Fig. 5.1, is actuated by an electrostatic excitation that consists of a static voltage V_{dc}, a time varying voltage V_{ac}, and an electromagnetic excitation driven by a Lorentz force. The actuator represents a parallel-plate capacitor

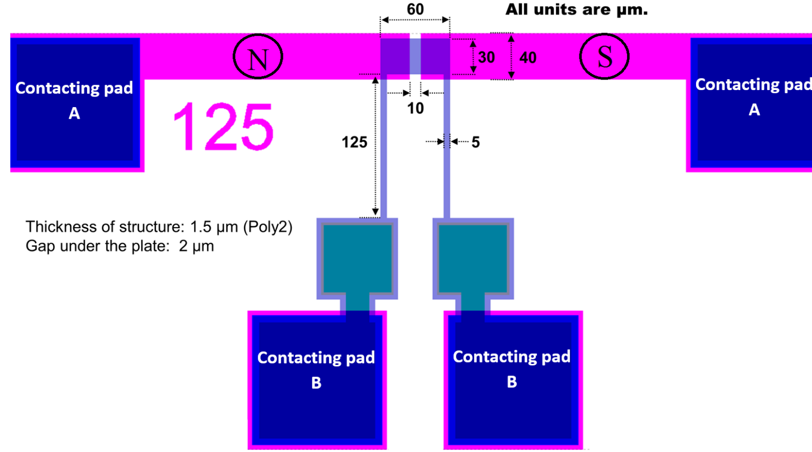

Figure 5.1: *A schematic diagram of the electrostatic/electromagnetic MEMS actuator.*

which has two plates: fixed substrate electrodes, and a movable microplate. This design allows the microplate to move in out-of-plane bending motion using the electrostatic force or in torsional motion using electromagnetic or electrostatic torque.

5.1.1 Actuator Operation Process

The combined electrostatic/electromagnetic actuator is excited electrostatically by two signals that are applied to the bonding pads as shown in Fig. 5.2. The excitation signals on both pads have the same shape and frequency with a phase difference of 180°:

$$\begin{aligned} V_a &= V_{dc} + V_{ac_1} \cos(\Omega t) \\ V_b &= V_{dc} + V_{ac_2} \cos(\Omega t + 180^\circ) \end{aligned} \tag{5.1}$$

where Ω is the excitation frequency in (rad/s). Moreover, when the amplitudes are equal $V_{ac_1} = V_{ac_2}$, the voltage drop between the microplate and the bottom electrodes is equal to V_{dc}. This voltage is used to move the microplate towards the bottom electrodes which results in a bending motion w.

When voltage drop is applied through one substrate electrode only while the other is grounded, the microplate rotates around its own axis under electrostatic torque. This torsional motion is limited by the snap down voltage where the plate's edge closer to the substrate comes into contact with it. To overcome this limitation, an electromagnetic

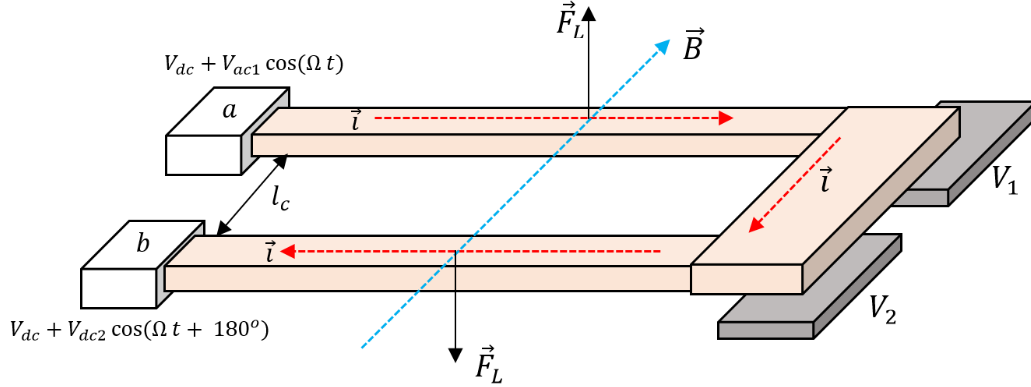

Figure 5.2: *A schematic of the actuation scheme of the electrostatic/electromagnetic actuator. The excitation current $\vec{i}(t)$ passes through the cantilever beams. An external magnetic field $\vec{B}$ crosses the current resulting in Lorentz force $\vec{F}_L$ acting on the beams.*

torque is introduced by the interaction of a current $\vec{i}(t)$ passing in the loop made of the support beams and microplate and an external magnetic field $\vec{B}$ due to the permanent magnets marked by N and S in Fig. 5.1. A Lorentz force appears due to the interaction between the excitation current that passes through the two cantilever beams and the magnetic field:

$$\vec{F}_L = l_b\ \vec{i}(t) \times \vec{B} \tag{5.2}$$

where l_b is the microbeam length.

Because of the symmetry in the design, the Lorentz force pair that are acting on the two microbeams are equal in magnitude but opposite in direction. As a result, an electromagnetic torque acting on the microplate is developed and can be expressed as:

$$\vec{T}_{em} = l_b\ l_c\ \vec{i}(t) \times \vec{B} \tag{5.3}$$

where l_c is the distance between the two cantilever beams. It is assumed that $l_c \approx b_p$. Since the current and magnetic field are designed to maintain a right angle, the electromagnetic torque vector reduces to:

$$T_{em} = l_b l_c i B \tag{5.4}$$

The electromagnetic torque is used to enhance the static and dynamic performance of the actuator's torsional mode. The following analytical model and simulations are based on the actuator that was designed and developed by Park *et al.* [67]. The model is used to investigate and predict the static and dynamic responses of the actuator.

5.2 Analytical Model

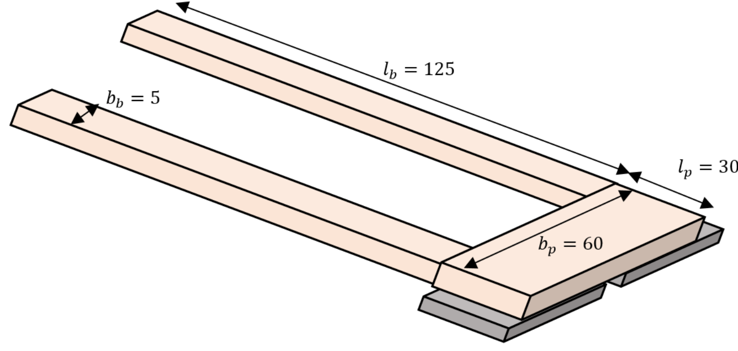

Figure 5.3: *The dimensions of the combined electrostatic/electromagnetic actuator.*

The combined electrostatic/electromagnetic actuator is modeled as a lumped-mass. The microactuator, Fig. 5.3, has a thickness h, and the distance between the lower surface of the microplate and bottom electrodes is denoted by d. The microplate rotates about its own axis when electrostatic or electromagnetic torque is applied. To produce the maximum twist angle β , the microplate has to be actuated electrostatically through one electrode assisted with an external electromagnetic torque. This technique is efficient because it results in low actuation voltage.

The model considers both the transverse deflection w due to the electrostatic force and rotational angle β due to electrostatic and electromagnetic torques while ignoring the microplate bending angle and the fringing electrostatic field. Fig. 5.4 shows a an end view of the combined actuator in the initial position where the applied voltage and external magnetic field are set equal to zero. The governing equations of motion in bending and torsion can be written as

$$m_{eq}\ddot{w} + (c_{vb} + c_{sb})\dot{w} + k_b w = F_{es1} + F_{es2} \tag{5.5}$$

$$J_t\ddot{\beta} + (c_{vt} + c_{st})\ \dot{\beta} + k_t\beta = T_{es1} + T_{es2} + T_{em} \tag{5.6}$$

F_{es1} and F_{es2} represent the electrostatic forces between the movable plate and left and right bottom electrodes, respectively. J_t is the microbeam's polar mass moment of inertia, c_{st} is the torsional squeeze-film damping, k_t is the mechanical torsional stiffness. The torsional viscous damping is defined as

$$c_{vt} = \frac{J_t\omega_{\circ t}}{Q_t}$$

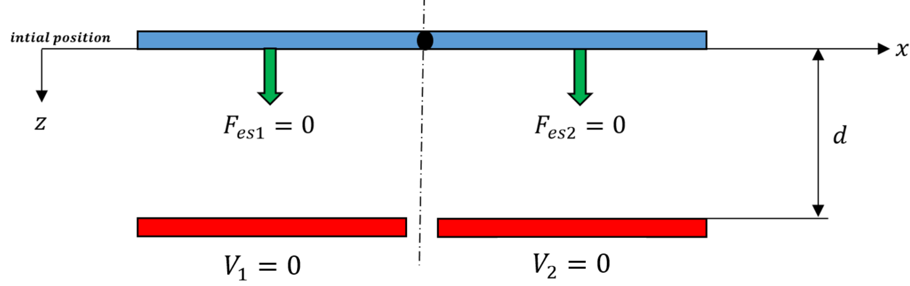

Figure 5.4: *The microplate in the intial position.*

where ω_{nt} is the natural frequency of the actuator's torsional mode and Q_t is its experimentally measured quality factor. T_{es1} and T_{es2} represent the electrostatic torque that is generated by the right and left bottom electrodes, respectively, and T_{em} is the electromagnetic torque. The effective mass m_{eq} and bending stiffness k_b formulas are given in Eqs. (3.14) and (3.17), respectively. The torsional stiffness of the cantilever beams can be written as [60]:

$$k_t = \frac{2GJ}{l_b} \tag{5.7}$$

where G is the shear modulus and J is the beam polar moment of area [60]:

$$J = \frac{b\ h^3}{3}(1 - 0.63\frac{h}{b}) \tag{5.8}$$

When the electrostatic forces that act on the left and right electrodes are equal in the magnitude and the external magnetic field B is zero, the microplate deforms in bending only as shown in Fig. 5.5. This results in a 1-DOF actuator with an effective gap $(d - w)$ similar to that investigated numerically and experimentally in Chapters 3 and 4.

However, when unequal voltages are applied through the left and right electrodes in the presence of an external magnetic field, coupled motions are encountered because electrostatic forces pull the microplate down with a small displacement (piston motion) while the difference between the voltages results in an electrostatic torque and the magnetic field results in an electromagnetic torque. This allows the microplate to rotates around its center axis as shown in Fig. 5.6.

Under these loads, the gap between the lower surface of the microplate and the bottom electrodes can be written as $(d - w + s\ \beta)$, where $s = b_p/2$ is half of the microplate width.

The electrostatic force acting on each half of the microplate is obtained by integrating the electrostatic pressure on a microplate strip dF_{esi} over the area:

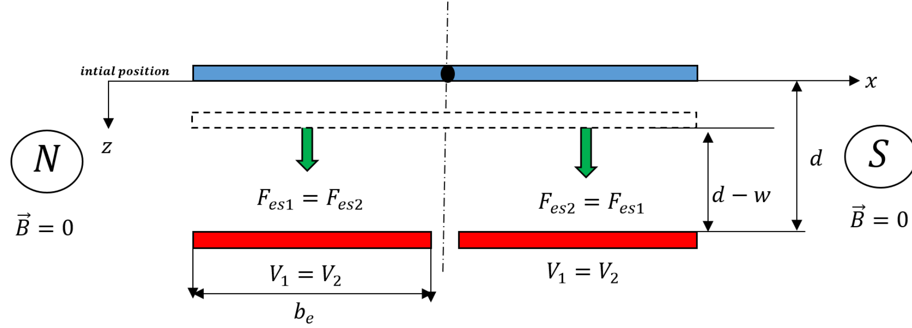

Figure 5.5: *The microplate in piston motion under equal voltages.*

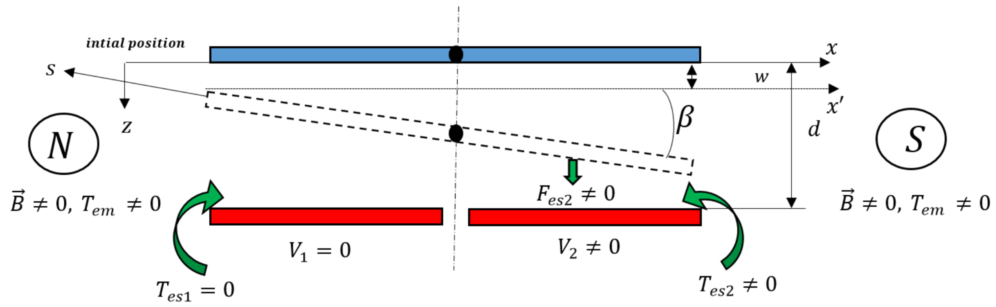

Figure 5.6: *The microplate deflection and rotation due to the electrostatic forces and electrostatic and electromagnetic torques.*

$$F_{es1} = \int_{-\frac{bp}{2}}^{0} dF_{es1} \tag{5.9}$$

$$F_{es2} = \int_{0}^{\frac{bp}{2}} dF_{es2} \tag{5.10}$$

where

$$dF_{es1} = \frac{1}{2}\ \epsilon\ l_p\ \frac{V_1^2}{d(s)^2}\ ds = \frac{1}{2}\ \epsilon\ l_p\ \frac{V_1^2}{(d-w+s\ \ \sin\beta)^2}\ ds \tag{5.11}$$

$$dF_{es2} = \frac{1}{2}\ \epsilon\ l_p\ \frac{V_2^2}{d(s)^2}\ ds = \frac{1}{2}\ \epsilon\ l_p\ \frac{V_2^2}{(d-w+s\ \ \sin\beta)^2}\ ds \tag{5.12}$$

for small twist angles

$$\sin\beta = \beta \tag{5.13}$$

Substituting Eqs. (5.11), (5.12) and (5.13) into Eqs. (5.9) and (5.10), we obtain:

$$F_{es1} = \frac{1}{2}\ \epsilon\ l_p\ V_1^2 \int_{\frac{-b_p}{2}}^{0} \frac{1}{(d-w+s\ \beta)^2} ds \tag{5.14}$$

$$F_{es2} = \frac{1}{2}\ \epsilon\ l_p\ V_2^2 \int_{0}^{\frac{b_p}{2}} \frac{1}{(d-w+s\ \beta)^2} ds \tag{5.15}$$

Integrating Eqs. (5.14) and (5.15) results in:

$$F_{es1} = \frac{1}{2}\ \epsilon\ A_p\ \frac{V_1^2}{(d-w)\ (2d-2w-b_p\ \beta)} \tag{5.16}$$

$$F_{es2} = \frac{1}{2}\ \epsilon\ A_p\ \frac{V_2^2}{(d-w)\ (2d-2w+b_p\ \beta)} \tag{5.17}$$

In addition, the electrostatic torque T_{es1} and T_{es1} are expressed as

$$T_{es1} = \int_{\frac{-b_p}{2}}^{0} s\ dF_{es_1} \tag{5.18}$$

$$T_{es2} = \int_{0}^{\frac{b_p}{2}} s\ dF_{es_2} \tag{5.19}$$

Evaluating the integrals in Eqs. (5.18) and (5.19), the electrostatic torques due to the voltage across both electrodes are obtained:

$$T_{es1} = \frac{\epsilon\ l_p\ V_1^2}{\beta^2}\Big(\frac{-\frac{b_p}{2}\ \beta}{2d-2w-b_p\ \beta} + \ln\frac{d-w}{d-w-\frac{b_p}{2}\ \beta}\Big) \tag{5.20}$$

$$T_{es2} = \frac{\epsilon\ l_p\ V_2^2}{\beta^2}\Big(\frac{-\frac{b_p}{2}\ \beta}{2d-2w+b_p\ \beta} + \ln\frac{d-w+\frac{b_p}{2}\ \beta}{d-w}\Big) \tag{5.21}$$

To write the governing equations motion under electrostatic/electromagnetic excitation, Eqs. (5.16) and (5.17) are substituted into Eq. (5.5) and Eqs. (5.20) and (5.21) are substituted into Eq. (5.6) to obtain:

$$\begin{aligned} m_{eq}\ddot{w} + (c_{vb} + c_{sb})\dot{w} + k_b\ w =& \frac{\epsilon\ A_p V_1^2}{2(d-w)(2d-2w-b_p\beta)} \\ &+ \frac{\epsilon\ A_p V_2^2}{2(d-w)(2d-2w+b_p\beta)} \end{aligned} \tag{5.22}$$

$$\begin{aligned} J_t\ddot{\beta} + (c_{vt} + c_{st})\ \dot{\beta} + k_b\ \beta =& \frac{\epsilon\ l_p\ V_1^2}{\beta^2}\Big(\frac{-\frac{b_p}{2}\ \beta}{2d-2w-b_p\ \beta} + \ln\frac{d-w}{d-w-\frac{b_p}{2}\ \beta}\Big) \\ &+ \frac{\epsilon\ l_p\ V_2^2}{\beta^2}\Big(\frac{-\frac{b_p}{2}\ \beta}{2d-2w+b_p\ \beta} + \ln\frac{d-w+\frac{b_p}{2}\ \beta}{d-w}\Big) \\ &+ l_c\ i\ l_p B \end{aligned} \tag{5.23}$$

For convenience, we introduce the following nondimensional variables

$$\hat{w} = \frac{w}{d}, \qquad \hat{t} = \frac{t}{T}, \qquad \hat{\beta} = \frac{\beta}{\beta_{max}} \tag{5.24}$$

where $T = \sqrt{\frac{m_{eq}}{k_b}}$ is a time scale and $\beta_{max} = \frac{2d}{b_p}$. Consequently,

$$\dot{w} = \frac{\partial w}{\partial t} = \frac{\partial(\hat{w}\ d)}{\partial(\hat{t}\ T)} = \frac{d}{T}\dot{\hat{w}}, \tag{5.25}$$

$$\ddot{w} = \frac{\partial \dot{w}}{\partial t^2} = \frac{\partial(\dot{\hat{w}}\ d)}{\partial(\hat{t}^2\ T^2)} = \frac{d}{T^2}\ddot{\hat{w}}\ , \tag{5.26}$$

$$\dot{\beta} = \frac{\partial \beta}{\partial t} = \frac{\partial(\hat{\beta}\ \beta_{max})}{\partial(\hat{t}\ T)} = \frac{2d}{T\ b_p}\ \dot{\hat{\beta}}\ , \tag{5.27}$$

$$\ddot{\beta} = \frac{\partial \dot{\beta}}{\partial t^2} = \frac{\partial(\dot{\hat{\beta}}\ \beta_{max})}{\partial(\hat{t}^2\ T^2)} = \frac{2d}{T^2\ b_p}\ \ddot{\hat{\beta}} \tag{5.28}$$

Substituting Eqs. (5.25) to (5.28) into Eq. (5.22), we obtain the nondimenstional bending equation of motion:

$$\begin{aligned} m_{eq}\frac{d}{T^2}\ddot{\hat{w}} + (c_{vb} + c_{sb})\frac{d}{T}\dot{\hat{w}} + k_b\ d\hat{w} =& \frac{\epsilon\ A_p V_1^2}{2(d-d\hat{w})(2d-2d\hat{w}-b_p\hat{\beta}\beta_{max})} \\ &+ \frac{\epsilon\ A_p V_2^2}{2(d-d\hat{w})(2d-2d\hat{w}+b_p\hat{\beta}\beta_{max})} \end{aligned} \tag{5.29}$$

Dividing by $\frac{d}{T^2}m_{eq}$ and defining the parameters

$$\mu_1 = c_{vb}\frac{T}{m_{eq}} \quad , \quad \mu_2 = c_{sb}\frac{T}{m_{eq}} \quad , \quad \alpha_4 = \frac{1}{4}\frac{\epsilon\ A_p}{k_{eq}\ d^3} \tag{5.30}$$

we obtain

$$\ddot{\hat{w}} + (\mu_1 + \mu_2)\dot{\hat{w}} + \hat{w} = \frac{\alpha_4 V_1^2}{(1-\hat{w})(1-\hat{w}-\hat{\beta})} + \frac{\alpha_4 V_2^2}{(1-\hat{w})(1-\hat{w}+\hat{\beta})} \tag{5.31}$$

Substituting Eqs. (5.25) to (5.28) into Eq. (5.23), we obtain the nondimensional torsional equation of motion:

$$\begin{aligned} J_t\frac{2d}{T^2\ b_p}\ \ddot{\hat{\beta}} + (c_{vt}+c_{st})\ \frac{2d}{T\ b_p}\ \dot{\hat{\beta}} + k_t\ \frac{2d}{b_p}\ \hat{\beta} = \\ \frac{\epsilon\ l_p\ V_1^2}{\hat{\beta}^2}\Big(\frac{-\frac{b_p}{2}\ \hat{\beta}}{2d-2d\hat{w}-b_p\ \hat{\beta}} + \ln\frac{d-w}{d-d\hat{w}-\frac{b_p}{2}\ \hat{\beta}}\Big) \\ +\frac{\epsilon\ l_p\ V_2^2}{\hat{\beta}^2}\Big(\frac{-\frac{b_p}{2}\ \hat{\beta}}{2d-2d\hat{w}+b_p\ \hat{\beta}} + \ln\frac{d-d\hat{w}+\frac{b_p}{2}\ \hat{\beta}}{d-d\hat{w}}\Big) \\ +l_c\ i\ l_p B \end{aligned} \tag{5.32}$$

Dividing by $J_t\frac{2d}{T^2\ b_p}$ and defining the parameters

$$\begin{gathered} \mu_3 = c_{vt}\ \frac{T}{J_t} \quad , \quad \mu_4 = c_{vt}\ \frac{T}{J_t} \quad , \quad \omega_{ot} = \sqrt{\frac{k_t}{J_t}\frac{m_{eq}}{k_b}} \\ \alpha_5 = \frac{1}{2}\frac{\epsilon\ l_p\ m_{eq}}{J_t\ k_b\ \hat{\beta}^2\ {\beta_{max}}^3} \quad , \quad \alpha_7 = J_t\frac{2d}{T^2\ b_p} \end{gathered}$$

we obtain

$$\begin{aligned} \ddot{\hat{\beta}} + (\mu_3+\mu_4)\ \dot{\hat{\beta}} + \omega_{ot}^2\hat{\beta} = \alpha_5\frac{V_1^2}{\hat{\beta}^2}\Big(\frac{-\hat{\beta}}{1-\hat{w}-\hat{\beta}} + \ln\frac{1-\hat{w}}{1-\hat{w}-\hat{\beta}}\Big) \\ + \alpha_5\frac{V_2^2}{\hat{\beta}^2}\Big(\frac{-\hat{\beta}}{1-\hat{w}+\hat{\beta}} + \ln\frac{1-\hat{w}+\hat{\beta}}{1-\hat{w}}\Big) \\ + \alpha_7 l_c\ i\ l_p B \end{aligned} \tag{5.33}$$

We adopt he model of Sattler *et al.* [68] to represent the torsional squeeze-film damping. This model analytically solves the linearized Reynolds equation and associated pressure

boundary conditions. Assuming a uniform gap between two rigid plates, squeeze-film damping was found proportional to the square of the maximum rotation angle the movable plate rotates taking form:

$$
\begin{aligned}
c_{st} &= \frac{A\ b_p^2}{d^3}\ \frac{(1+\beta)^2}{(1-\beta^2)^2} \\
&= \frac{A\ b_p^2}{d^3}\ \frac{(1+\hat{\beta}\beta_{max})^2}{(1-(\hat{\beta}\beta_{max})^2)^2}
\end{aligned}
\tag{5.34}
$$

For the sake of brevity, we dispense with the over hats rewrite the equation of motion in terms of w and β.

We will investigate the static and dynamic behavior of the electrostatic/electromagnetic actuator. The lumped mass model that was described previously is solved numerically for the static response when actuated by an electrostatic load V_{dc} and a constant electromagnetic torque. The eigenvalue problem is solved in order to find the actuator's first torsional natural frequency under those static loads. Moreover, the dynamic response is investigated under electrostatic and electromagnetic excitation forces and the results are compared to experimental results. This section investigates the following major phenomena in the electrostatic/electromagnetic MEMS actuator:

- The snap-down voltage
- Natural frequencies and the dynamic response
- The actuator's calibration

5.3 Static Analysis

The static torsional angle of the microplate was examined under different electrostatic and electromagnetic torques. The range of torsional electrostatic MEMS actuator is limited by snap-down voltage. At this voltage, the microplate edge lands quickly on the substrate (bottom electrode). To obtain the equilibrium position of the microplate β_s under electrostatic actuation only, dc voltage is set to $V_1 = V_{dc}$ and $V_2 = 0$, the magnetic field is eliminated $B = 0$, and the time-dependent terms in the equation of motion, Eq. (5.33), are set equal to zero. The torsional equilibrium equation is then reduced to:

$$
\omega_{ot}^2 \beta_s = \alpha_5 \frac{V_{dc}}{\beta_s^2}\Big(\frac{-\beta_s}{1-\beta_s} + \ln\frac{1}{1-\beta_s}\Big) \tag{5.35}
$$

where piston motion (bending) has been ignored.

This algebraic equation is solved numerically for the static equilibrium β_s corresponding to V_{dc}. Figure 5.7(a) shows the relationship between the microplate torsion angle and the actuation voltage V_{dc}. It increases nonlinearly with the actuation voltage V_{dc} until the microplate edge touches the substrate. The snap-down voltage, where the actuator losses stability, was calculated as 13.5 V. The microplate achieved a maximum torsion angle of $\beta_s = 0.04°$ at 13.5 V. The model was validated by comparing its predicted results, solid red line in Fig 5.7(a), to the results of FEM simulations shown as blue diamonds $\diamond$ in the figure. It shows good agreement between the lumped-mass model and FEM results.

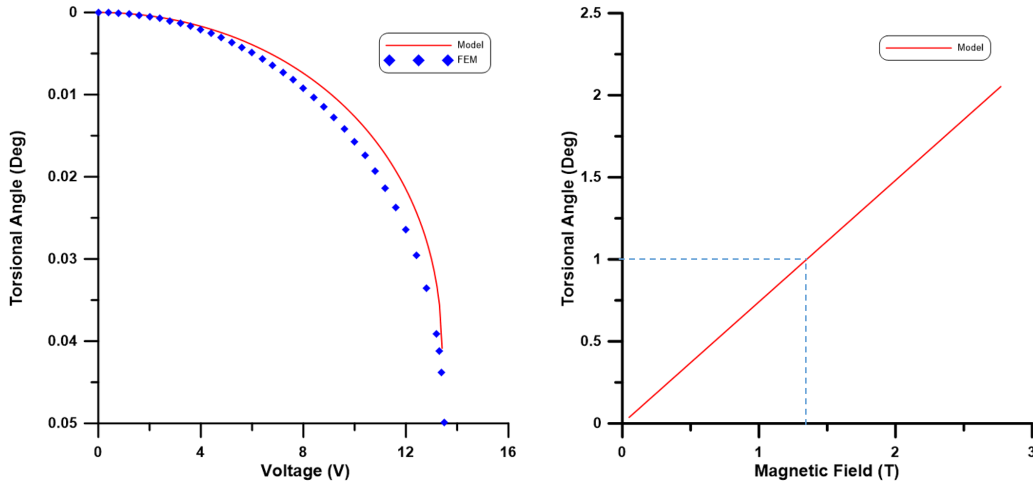

Figure 5.7: *Model predicted (red line) and measured ($\diamond$ symbols) (a) static torsion angle β_s vs. actuation voltage V_{dc} and (b) static torsion angle β_s vs. magnetic field B.*

To compare the static response of the actuator under electrostatic and electromagnetic loads, we subject it to a constant electromagnetic torque only. The voltage and time-varying terms in the equation of motion, Eq. (5.33), are set equal to zero, dc current is set equal to $i = 3.3\,\mathrm{mA}$, and the magnetic field density B is varied from 0 to 3 T. The equilibrium equation, thereby, reduces to:

$$\beta_s = \alpha_7 l_c i \; l_p B \tag{5.36}$$

Figure 5.7(b) shows the relationship between the microplate torsion angle β_s and the magnetic field density B. It increases linearly with the magnetic field. We can achieve a

torsion angle of $\beta_s = 1°$ at 1.4 T as shown in Fig. (5.7)(b). These results indicate that electromagnetic torque is more efficient in obtaining larger torsion angles than electrostatic torque.

5.4 Eigenvalue Analysis

The eigenvalue problem of the combined electrostatic/electromagnetic actuator is solved analytically based on a 1 DOF lumped-element model. This analysis investigates variation in the first torsional natural frequency ω_{nt} under a static load $V_1 = V_{dc}$ supplied through one substrate electrode ($V_2 = 0$). Dropping the damping terms, setting the electromagnetic field equal to zero ($B = 0$), and ignoring the static deflection $w_s = 0$ due to electrostatic force results in torsional equation of motion, Eq. (5.33),to:

$$\ddot{\beta} + \omega_{ot}^2 \beta = \alpha_5 \frac{V_{dc}^2}{\beta^2}\Big(\frac{-\beta}{1-\beta} + \ln\frac{1}{1-\beta}\Big) \tag{5.37}$$

Substituting with the expansion $\beta = \beta - s + \beta_d$, expanding the electrostatic torque around β_d in a Taylor series, ignoring the resulting nonlinear terms, dropping the static part of the electrostatic torque, and , we obtain:

$$\ddot{\beta}_d + \omega_{ot}^2 (\beta_s + \beta_d) = \alpha_5 \frac{V_{dc}^2}{(\beta_s+\beta_d)^2}\Big(\frac{-(\beta_s+\beta_d)}{1-(\beta_s+\beta_d)} + \ln\frac{1}{1-(\beta_s+\beta_d)}\Big) \tag{5.38}$$

Assuming that the boundaries of electrostatic forces and torques are constant and static twisting angle is equal to zero (β_s=0), Eq. (5.39) reduced to

$$\ddot{\beta}_d + \omega_{ot}^2 \beta_d = \alpha_5 \frac{V_{dc}^2}{\beta_d^2}\Big(\frac{-\beta_d}{1-\beta_d} + \ln\frac{1}{1-\beta_d}\Big) \tag{5.39}$$

Substituting the harmonic solution $\beta_d = Ae^{i\omega_{nt}t}$ form into the linearized equation of motion, we obtain the undamped eigenvalue problem:

$$-\omega_{nt}^2 \beta_d + \omega_{ot}^2 \beta_d = -\alpha_5 \frac{V_{dc}^2 \, {b_p}^3 \beta_{max}^3}{12d^3} \beta_d \tag{5.40}$$

Equation. (5.40) can be written as:

$$\omega_{nt}^2 = \omega_{ot}^2 + \alpha_8 \tag{5.41}$$

where

$$\alpha_8 = \frac{V_{dc}^2 \ \epsilon \ A_p \ {b_p}^2}{12 J_t \ k_b \ d^3}$$

The variation of the torsional natural frequency as V_{dc} increases can be expressed as

$$\omega_{nt} = \pm\sqrt{\omega_{ot} + \alpha_8} \tag{5.42}$$

The dimensional torsional natural frequency can be written in Hz units as

$$f_{nt} = \frac{\omega_{nt}}{2\pi T} \tag{5.43}$$

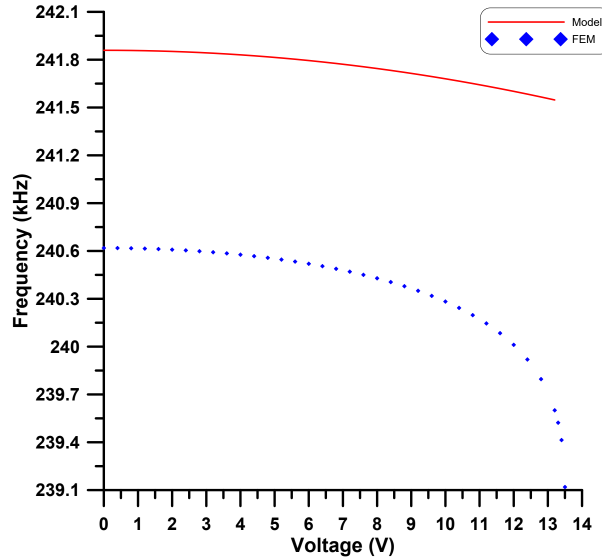

Figure 5.8: *A comparison of the corresponding natural frequency results to the applied voltage that obtained from the lumped-mass model (red line) and FEM (blue $\diamond$ symbols).*

The torsional natural frequency and mode shape of the system is calculated numerically using the FEM package COMSOL 3.3, is found to be 240.7 kHz; however; the model prediction gives a 242 kHz as a natural frequency. The difference in the natural frequency

values is expected because the FEM is a multidegree of freedom model and will capture the natural frequencies more accurately than the single degree of freedom model.

Experimentally, the torsional natural frequency and the mode shape were determined using a laser vibrometer; and the experimental setup is described by Alghamdi [69]. To measure the torsional natural frequency, an impulse signal with $f = 1\,\mathrm{kHz}$ is applied using a function generator. Then, a manual frequency sweep in the frequency range of $[0, 400]\,\mathrm{kHz}$ is used to capture the system's natural frequencies.

The first torsional mode was found experimentally to occur at a frequency of 182 kHz. The difference in the natural frequency values between the experimental and FEM is expected because the uncertainty in the realized dimensions as compared to the nominal dimensions and the absence of damping in the FEM model. This value was used to estimate the support beams width $b_b = 4.4\,\mu\mathrm{m}$ and the structural layer thickness $h_b = 1.15\,\mu\mathrm{m}$ resulting in an effective linear stiffness and mass of $k_{eq} = 0.2305\,\mathrm{N/m}$ and $m_{eq} = 5.5\,\mathrm{ng}$. The capacitive gap remains constant $d = 2.15\,\mu\mathrm{m}$. Figure 5.9 shows the first torsional mode shape that obtained numerically from the FEM model and experimentally using a multi-scan. It also shows a good agreement in the mode shape.

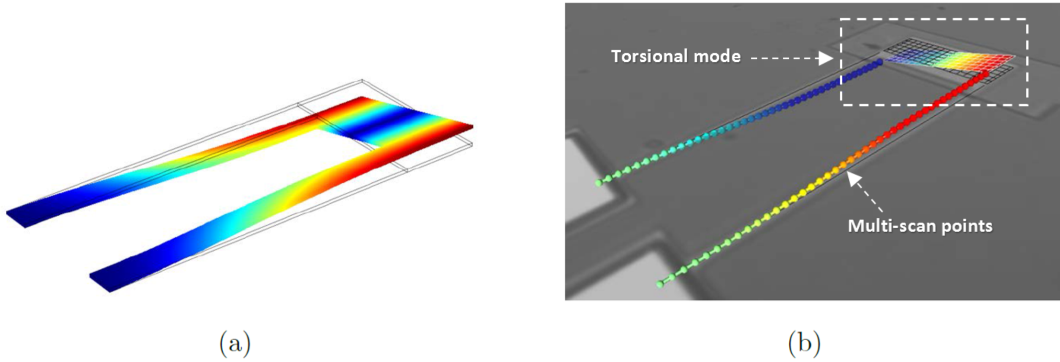

(a) (b)

Figure 5.9: *Comparison of the first torsional mode shape obtained by (a) FEM at* 198 *kHz and (b) experimentally at* 182 *kHz.*

The variation in the torsional angle due to the changing in the static voltage V_{dc} is shown in Fig. 5.8. Both predicted model and FEM resulted in the same snap-down voltage $V_{snap} = 13.5\,\mathrm{V}$.

5.5 Dynamic Analysis

In this section, we investigate the dynamic response of the electrostatic/electromagnetic actuator's first torsional mode. We compare the response under a given electrostatic force in the presence and absence of a magnetic field. The microplate, Fig. 5.2, is excited electrostatically by applying the signals V_a and V_b, Eq. (5.1), to pads a and b, respectively, where the bias voltage is set to $V_{dc} = 0$ and $V_{ac_1} = V_{ac_2} = V_{ac}$. This setup is designed to ground the microplate, thereby applying no electrostatic forces or torque to it. On the other hand, the passage of a current

$$i(t) = \frac{2V_{ac}}{R_p}\cos(\Omega t),$$

where R_p is the path resistance, in the microcantilevers due to the voltage difference between V_a and V_b allows us to apply a purely electromagnetic torque to the actuator. This torque is regulated by the magnitude of the magnetic field density B.

The actuator can be operated in a forced mode, where the excitation frequency Ω is away from the resonant frequency, or in resonant mode where the two frequencies are close to each other $\Omega \approx \omega_{\text{ot}}$ to maximize response. Resonant mode actuation is adopted to enhance the actuator's stroke size. During the test, the signal frequency is set equal to the first torsional natural frequency $f = 182\,\text{kHz}$ and $V_{ac} = 2.25\,\text{V}$. The dynamic response is measured experimentally at the edge of the microplate in the absence and presence of a magnetic field, $B = 0\,\text{mT}$ and $B = 27.8\,\text{mT}$, using a laser Doppler vibrometer. The quality factor of the actuator response at the first torsional frequency was estimated from the experimental measurements as $Q_t = 1.47$. This value is adopted in the model numerical simulation.

The FFT of the microplate edge velocity $\dot{w}$ is represented by the blue diamond symbols in Fig. 5.10. The FFT of the numerically predicted velocity $\dot{w}$ is represented by a red line. It is obtained by integrating Eqs. (5.31) and (5.33) for 8000 excitation periods ($8000T_s$) and retaining the time-history for the last 30 periods only. To match the model predicted edge velocity to that measured experimentally at resonance in the absence of the magnetic field (0.34 mm/s), a background magnetic field of $B = 0.003\,\text{mT}$ was added to the model. This value represents the level of uncertainty in the actuator dimensions and the function generator signal parameters. In the presence of a magnetic field ($B = 27.8\,\text{mT}$), peak edge velocity at resonance was 27 times that under background magnetic field (9.38 mm/s). The agreement between the moel and experimental results validated our dynamic model, Eq.(5.33).

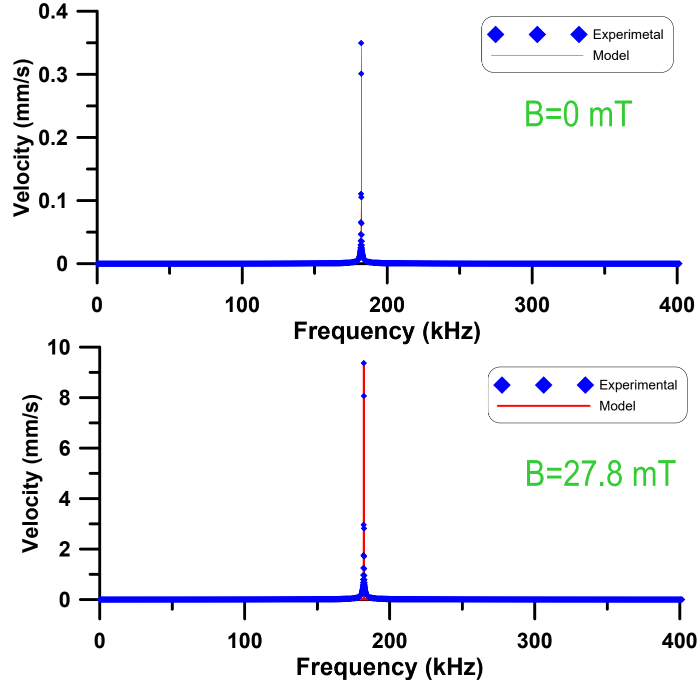

Figure 5.10: *The FFTs of the measured (◇ symbols) and the model predicted edge velocity at the edge (red line) in (a) the absence ($B = 0\,mT$) and (b) presence ($B = 27.8\,mT$) of an external magnetic field where $f = 182\,kHz$.*

5.6 Actuator Calibration

The electrostatic/electromagnetic actuator was placed inside a custom-made test chamber $(10.6 \times 6.3 \times 1.8)\,\text{cm}^3$. Two permanent magnets were attached to opposite walls of the chamber as shown in Fig. 5.11(a), such that their North and South poles are facing each other. The actuator chip carrier is mounted to a breadboarded and placed inside the chamber. The excitation signals V_a and V_b are delivered to bonding pads a and b through the breadboard and chip carrier.

A Hall effect sensor, Allegro MicroSystems LLC A1360 [70], is mounted to the breadboard next to the chip carrier to measure the magnetic field density between the two

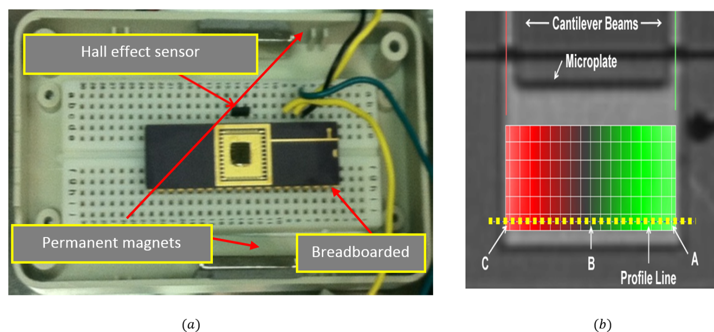

Figure 5.11: *(a) The electrostatic/electromagnetic actuator mounted inside the test chamber. (b) A vibrometer multi-scan grid showing point A where edge displacement and velocity are measured.*

permanent magnets. In this experiment, the magnetic field is set to $B = 64\,\text{mT}$, the excitation signals are set to $V_{ac_1} = V_{ac_2} = 2.5\,\text{V}$, $V_{dc} = 0$ and the excitation frequency to $f = 182\,\text{kHz}$. This setup results in the passage of a current between pads a and b measured as $i = 3.3\,\text{mA}$. A laser Doppler vibrometer is used to obtain the displacement and velocity of the microplate edge, point A in Fig. 5.11(b). A procedure similar to that described above was used to obtain the model predicted FFT. The close agreement seen in Fig. 5.12 between the experimental (blue diamond symbols) and model predicted (red lines) FFTs throughout the frequency spectrum indicates that the model can capture the actuator dynamic response under combined electrostatic and electromagnetic actuation accurately.

The static pull-in voltage of the actuator was experimentally measured at 6.9 V and numerically calculated to be 7 V. Based on this value, we defined six operating points for the actuator at $V_{dc} = 1, 2, 3, 4, 5$, and 6 V. In each case, the actuator was excited by the external magnetic field of $B = 64\,\text{mT}$ and the harmonic signals V_a and V_b with $V_{ac_1} = V_{ac_2} = 2.5\,\text{V}$, $V_{dc} = 0$ and $f = 182\,\text{kHz}$. FFTs for the measured velocity of point A are shown in Fig. 5.12.

The increase in the electrostatic field strength with V_{dc} decreases the distance between the microplate and bottom electrode. As a result, squeeze-film increases leading the model to over predict the actuator response for larger V_{dc} values as shown in Fig. 5.13. However the peak velocity values observed at the natural frequency are similar for the model and experiment as shown in the following Table.

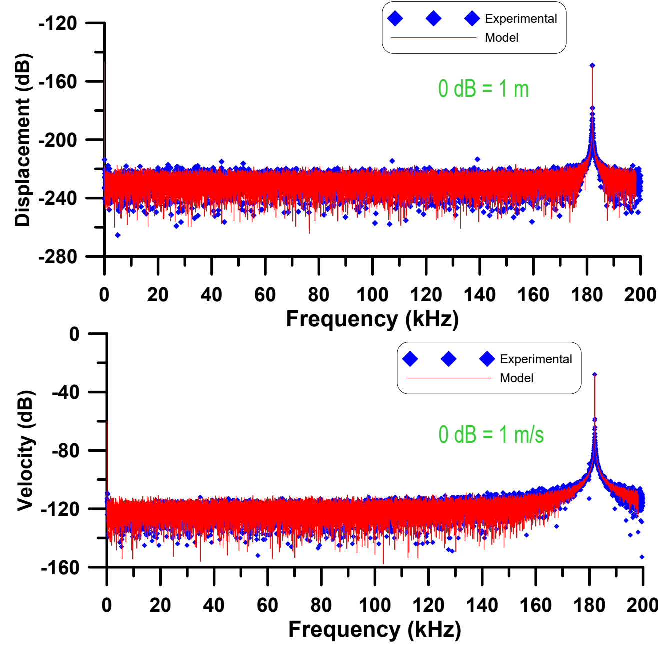

Figure 5.12: *The measured (◇ symbols) and the predicted (red lines) FFTs of point A displacement and velocity. The actuator is excited electrostatically by* $V_{ac_1} = V_{ac_2} = 2.5\ V$, $V_{dc} = 0$ *and electromagnetically by* $i = 3.3\,mA$ *and* $B = 64\,mT$ *at a frequency of* $f = 182\,kHz$.

Table 5.1: Peak magnitudes of the model predicted and experimentally measured velocity for (a) $V_{dc} = 1\,\text{V}$, (b) $V_{dc} = 2\,\text{V}$, (c) $V_{dc} = 3\,\text{V}$, (d) $V_{dc} = 4\,\text{V}$, (e) $V_{dc} = 5\,\text{V}$ and (f) $V_{dc} = 6\,\text{V}$.

Test	Experiment	Model
a	-28.06	-27.78
b	-27.87	-27.68
c	-27.96	-27.67
d	-26.84	-27.65
e	-29.23	-27.63
f	-23.22	-27.62

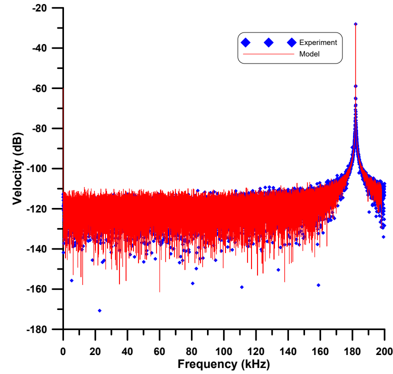

(a)

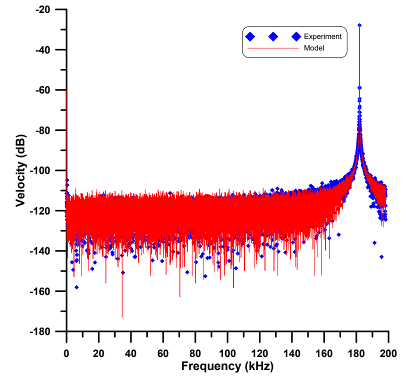

(b)

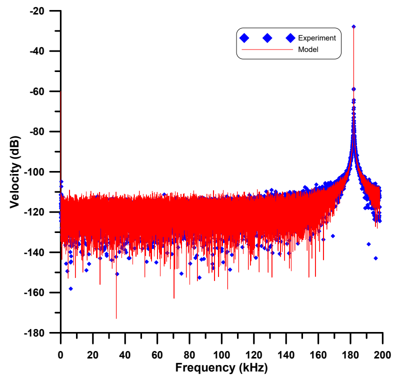

(c)

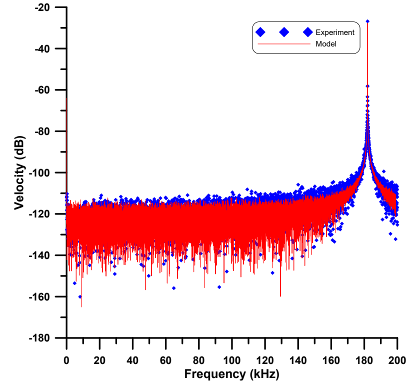

(d)

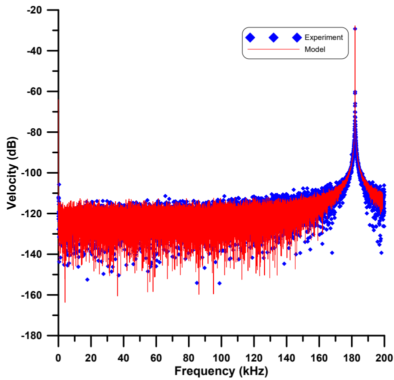

(e)

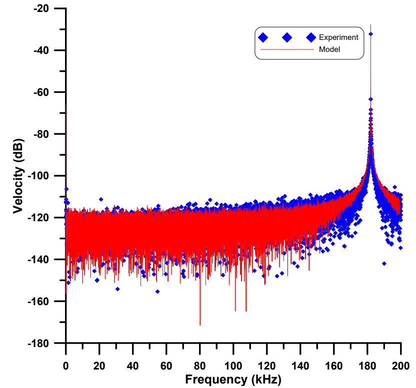

(f)

Figure 5.13: *The experimental and model predicted FFTs for* $B = 64\,mT$, $i = 3.3\,mA$, $V_{ac_1} = V_{ac_2} = 2.5\ V$, *and* $f = 182\,kHz$. *The bias voltage is set set (a)* $V_{dc} = 1\ V$, *(b)* $V_{dc} = 2\ V$, *(c)* $V_{dc} = 3\ V$, *(d)* $V_{dc} = 4\ V$, *(e)* $V_{dc} = 5\ V$ *and (f)* $V_{dc} = 6\ V$.

Chapter 6

Conclusions and Future Work

We summarize and discuss the most important results in this work which are: the effect of squeeze-film damping on electrostatic MEMS actuators, a nonlinear parameter identification technique for electrostatic MEMS actuators, and a novel combined electrostatic/electromagnetic actuator.

6.1 Conclusions

We developed a mathematical model for an electrostatic MEMS actuator and utilized it to study the effects of squeeze-film damping and multi-frequency excitation as well as the inclination angle of the micro-actuator. The model showed that, using electrostatic force results in a significant response at the higher frequency component $\propto \frac{1}{2}{V_{ac}}^2$ as the dynamic load increases.

A nonlinear parameter identification technique for electrostatic MEMS actuators has been developed. It can identify the lumped system parameters of the actuator from the experimentally obtained FFTs of its responses in primary, superharmonic, or subharmonic resonances. Our results show that a generalized Duffing oscillator model in combination with process and measurement noise can capture accurately the motions and resonances of electrostatic actuators. It is necessary to include process noise in the model to capture the resonant (large-amplitude) response of the actuator and measurement noise to capture small-amplitude motions (away from resonance).

The FFTs of the measured velocity were obtained using a Laser Doppler vibrometer. All experiments were conducted in soft vacuum to eliminate the effect of squeeze-film damping

and, thereby, elevate the actuator's quality factor. The spectral density of measurement noise in the experimental FFTs matched well with that in the model predicted FFTs, which shows the model fidelity. In addition, our parameter identification method was able to estimate the spectral density of process noise, which is difficult to measure experimentally.

While our parameter identification technique is equally applicable to experimental FFTs obtained from primary, superharmonic, or subharmonic excitations, and the Duffing oscillator model was able to reproduce the actuator response across all three cases, we found limitations in their applicability to secondary resonances. Specifically, the model was not able to fully recreate the forced response at $\frac{1}{2}\omega_{nb}$ in the case of superharmonic resonance. It was also unable to identify the mechanism responsible for the appearance of harmonics at integer multiples of $\frac{1}{2}\omega_{nb}$ in the case of subharmonic resonance. The subharmonic activation threshold was defined numerically in order to find the accurate forcing level that can be utilized to activate subharmonic resonance experimentally. In deed, the model needs further work to include flicker noise which should enable it to capture more accurately the actuator's low-frequency response. Moreover, squeeze-film damping was found to has a significant effect on the overall performance of the actuator.

We compared numerically and experimentally a novel combined electrostatic /electromagnetic actuator. It utilizes an electrostatic force associated with an electromagnetic force driven by a Lorentz force to examine the static torsional motion and to investigate its dynamic response when excited at the torsional resonant frequency $f_{nt} = 182\,\text{kHz}$. The results show that electromagnetic excitation is more efficient than electrostatic actuation. Specifically, the maximum torsion angle obtained under electromagnetic actuation is $1°$ which is more than 20 times the maximum angle obtained under electrostatic actuation ($0.04°$). The underlying reason is that under electrostatic actuation the actuator moves towards the bottom electrode as it rotates in torsion. This piston motion reduces the space available for the mirror torsional motion. On the other hand, electromagnetic actuation does not induce piston motions leaving the space between the mirror and the substrate for use by torsional motions only. Moreover, we validated the lumped mass model of the combined electrostatic electromagnetic actuator by comparing its dynamic results to experimental measurements at resonance. The results show that using electrostatic excitation in addition to electromagnetic excitation results in a significant increase in the dynamic response of the actuator.

6.2 Future Work

The developed mathematical model of the electrostatic MEMS actuator should be extended to consider nonlinear damping in order to capture the dynamic response accurately. Also, the stability and the performance of the combined electrostatic/electromagnetic actuator has to be investigated in depth.

Bibliography

[1] Senturia, S. D. (2007). Microsystem design. Springer Science & Business Media.

[2] Kaajakari, V. (2009). Practical MEMS: Design of microsystems, accelerometers, gyroscopes, RF MEMS, optical MEMS, and microfluidic systems. Las Vegas, NV: Small Gear Publishing.

[3] Judy, J. W. (2001). Microelectromechanical systems (MEMS): fabrication, design and applications. Smart materials and Structures, 10(6), 1115.

[4] Bell, D. J., Lu, T. J., Fleck, N. A., & Spearing, S. M. (2005). MEMS actuators and sensors: observations on their performance and selection for purpose. Journal of Micromechanics and Microengineering, 15(7), S153.

[5] Wu, M. C., Solgaard, O., & Ford, J. E. (2006). Optical MEMS for lightwave communication. Lightwave Technology, Journal of, 24(12), 4433-4454.

[6] Younis, M. I. (2011). MEMS linear and nonlinear statics and dynamics (Vol. 20). Springer Science & Business Media.

[7] Saadon, S., & Sidek, O. (2011). A review of vibration-based MEMS piezoelectric energy harvesters. energy conversion and management, 52(1), 500-504.

[8] Renaud, M., Karakaya, K., Sterken, T., Fiorini, P., Van Hoof, C., & Puers, R. (2008). Fabrication, modelling and characterization of MEMS piezoelectric vibration harvesters. Sensors and Actuators A: Physical, 145, 380-386.

[9] Polla, D. L., & Francis, L. F. (1998). Processing and characterization of piezoelectric materials and integration into microelectromechanical systems. Annual review of materials science, 28(1), 563-597.

[10] Wu, J., Fedder, G. K., & Carley, L. R. (2004). A low-noise low-offset capacitive sensing amplifier for a 50-g/ Hz monolithic CMOS MEMS accelerometer. Solid-State Circuits, IEEE Journal of, 39(5), 722-730.

[11] Singh, J., Gan, T., Agarwal, A., & Liw, S. (2005). 3D free space thermally actuated micromirror device. Sensors and Actuators A: Physical, 123, 468-475.

[12] Huang, Q. A., & Lee, N. K. S. (1999). Analysis and design of polysilicon thermal flexure actuator. Journal of Micromechanics and Microengineering, 9(1), 64.

[13] Zhang, W. M., Yan, H., Peng, Z. K., & Meng, G. (2014). Electrostatic pull-in instability in MEMS/NEMS: A review. Sensors and Actuators A: Physical, 214, 187-218.

[14] Lizhoung, X., & Xiaoli, J. (2007). Electromechanical coupled nonlinear dynamics for microbeams, Arch. Applied Mechanics, 77, 485-502.

[15] Alsaleem, F. M., Younis, M. I., & Ouakad, H. M. (2009). On the nonlinear resonances and dynamic pull-in of electrostatically actuated resonators. Journal of Micromechanics and Microengineering, 19(4), 045013.

[16] Zhang, Y., & Zhao, Y. P. (2006). Numerical and analytical study on the pull-in instability of micro-structure under electrostatic loading. Sensors and Actuators A: Physical, 127(2), 366-380.

[17] Chaterjee, S., & Pohit, G. (2009). A large deflection model for the pull-in analysis of electrostatically actuated microcantilever beams. Journal of sound and vibration, 322(4), 969-986.

[18] Moeenfard, H., Darvishian, A., & Ahmadian, M. T. (2013). Analytical modeling of the effects of electrostatic actuation and casimir force on the pull-in instability and static behavior of torsional nano/micro actuators. International Journal of Modern Physics B, 27(06), 1350008.

[19] He, S., Mrad, R. B., & Chong, J. (2011). Repulsive-force out-of-plane large stroke translation micro electrostatic actuator. Journal of Micromechanics and Microengineering, 21(7), 075002.

[20] Towfighian, S., He, S., & Mrad, R. B. (2014, August). A Low Voltage Electrostatic Micro Actuator for Large Out-of-Plane Displacement. In ASME 2014 International Design Engineering Technical Conferences and Computers and Information in Engineering Conference (pp. V004T09A015-V004T09A015). American Society of Mechanical Engineers.

[21] Hu, F., Wang, W., & Yao, J. (2011). An electrostatic MEMS spring actuator with large stroke and out-of-plane actuation. Journal of Micromechanics and Microengineering, 21(11), 115029.

[22] Ren, H., Wang, W., Tao, F., & Yao, J. (2013). A bi-directional out-of-plane actuator by electrostatic force. Micromachines, 4(4), 431-443.

[23] Moreira, E. E., Alves, F. S., Dias, R. A., Costa, M., Fonseca, H., Cabral, J., & Rocha, L. A. (2015, January). Bi-directional extended range parallel plate electrostatic actuator based on feedback linearization. In Micro Electro Mechanical Systems (MEMS), 2015 28th IEEE International Conference on (pp. 1036-1039). IEEE.

[24] Ren, H., Tao, F., Wang, W., & Yao, J. (2011). An out-of-plane electrostatic actuator based on the lever principle. Journal of Micromechanics and Microengineering, 21(4), 045019.

[25] Trivedi, R. R., Bhushan, A., Joglekar, M. M., Pawaskar, D. N., & Shimpi, R. P. (2015). Enhancement of static and dynamic travel range of electrostatically actuated microbeams using hybrid simulated annealing. International Journal of Mechanical Sciences, 98, 93-110.

[26] Ma, C. W., Lee, F. W., Liao, H. H., Kuo, W. C., & Yang, Y. J. (2015). Low-Actuation Voltage MEMS Digital-to-Analog Converter with Parylene Spring Structures. Sensors, 15(9), 21567-21580.

[27] Park, S., Khater, M., & Abdel-Rahman, E. (2013, August). Low Voltage Electrostatic Actuation for MEMS Actuator Using frequency Modulation. In ASME 2013 International Design Engineering Technical Conferences and Computers and Information in Engineering Conference (pp. V001T09A015-V001T09A015). American Society of Mechanical Engineers.

[28] Hu, F., Li, Z., Qian, Y., Yao, J., Xiong, X., Niu, J., & Peng, Z. (2012). A multi-electrode and pre-deformed bilayer spring structure electrostatic attractive MEMS actuator with large stroke at low actuation voltage. Journal of Micromechanics and Microengineering, 22(9), 095023.

[29] Chuang, W. C., Lee, H. L., Chang, P. Z., & Hu, Y. C. (2010). Review on the modeling of electrostatic MEMS. Sensors, 10(6), 6149-6171.

[30] Oh, K. W., & Ahn, C. H. (2006). A review of microvalves. Journal of micromechanics and microengineering, 16(5), R13.

[31] Nisar, A., Afzulpurkar, N., Mahaisavariya, B., & Tuantranont, A. (2008). MEMS-based micropumps in drug delivery and biomedical applications. Sensors and Actuators B: Chemical, 130(2), 917-942.

[32] Nayfeh, A. H., & Mook, D. T. (2008). Nonlinear oscillations. John Wiley & Sons.

[33] Younis, M. I., & Nayfeh, A. H. (2003). A study of the nonlinear response of a resonant microbeam to an electric actuation. Nonlinear Dynamics, 31(1), 91-117.

[34] Abdel-Rahman, E., & Nayfeh, A., (2003). Secondary resonances of electrically actuated resonant microsensors. Journal of Micromechanics and Microenginering, 13, pp. 491-501.

[35] Younis, M. I., & Alsaleem, F. (2009). Exploration of new concepts for mass detection in electrostatically-actuated structures based on nonlinear phenomena. Journal of computational and nonlinear dynamics, 4(2), 021010.

[36] Najar, F., Nayfeh, A. H., Abdel-Rahman, E. M., Choura, S., & El-Borgi, S. (2010). Nonlinear Analysis of MEMS Electrostatic Microactuators: Primary and Secondary Resonances of the First Mode. Journal of Vibration and Control, 16(9), 1321-1349.

[37] Han, J., Zhang, Q., & Wang, W. (2015). Static bifurcation and primary resonance analysis of a MEMS resonator actuated by two symmetrical electrodes. Nonlinear Dynamics, 80(3), 1585-1599.

[38] Alkharabsheh, S. A., & Younis, M. I. (2013). Dynamics of MEMS arches of flexible supports. Microelectromechanical Systems, Journal of, 22(1), 216-224.

[39] Ekici, H. O., & Boyaci, H. (2007). Effects of non-ideal boundary conditions on vibrations of microbeams. Journal of Vibration and Control, 13(9-10), 1369-1378.

[40] Yan, X., Qi, M., Wu, X., Wang, P., Pu, J., & Lin, L. (2014). Electrostatic cantilever resonators under a double-sided pullpull drive scheme. Journal of Micromechanics and Microengineering, 24(3), 035004.

[41] Razavi, B., (2002). Design of Analog CMOS Integrated Circuits. Tata McGraw-Hill, pp. 201-239.

[42] Pettai, R. (1984). Noise in receiving systems. Wiley.

[43] Hooge, F. N. (1994). 1/f noise sources. Electron Devices, IEEE Transactions on, 41(11), 1926-1935.

[44] Kay, A. (2012). Operational amplifier noise: techniques and tips for analyzing and reducing noise. Elsevier.

[45] Ahn, C. H., Kim, Y. J., & Allen, M. G. (1993). A planar variable reluctance magnetic micromotor with fully integrated stator and coils. Microelectromechanical Systems, Journal of, 2(4), 165-173.

[46] Guckel, H. (1998). High-aspect-ratio micromachining via deep X-ray lithography. Proceedings of the IEEE, 86(8), 1586-1593.

[47] Ko, J. S., Lee, M. L., Lee, D. S., Choi, C. A., & Kim, Y. T. (2002). Development and application of a laterally driven electromagnetic microactuator. Applied physics letters, 81(3), 547-549.

[48] Lagorce, L. K., Brand, O., & Allen, M. G. (1999). Magnetic microactuators based on polymer magnets. Microelectromechanical Systems, Journal of, 8(1), 2-9.

[49] Cleland, A. N., & Roukes, M. L. (1996). Fabrication of high frequency nanometer scale mechanical resonators from bulk Si crystals. Applied Physics Letters, 69(18), 2653-2655.

[50] Cugat, O., Delamare, J., & Reyne, G. (2003). Magnetic micro-actuators and systems (MAGMAS). Magnetics, IEEE Transactions on, 39(6), 3607-3612.

[51] Sze, S. M. (Ed.). (1994). Semiconductor sensors (Vol. 55). New York: Wiley.

[52] Chang, C., Tsai, M., Liu, Y., Sun, C., & Fang, W. (2013, January). Development of multi-axes CMOS-MEMS resonant magnetic sensor using Lorentz and electromagnetic forces. In Micro Electro Mechanical Systems (MEMS), 2013 IEEE 26th International Conference on (pp. 193-196). IEEE. Chicago

[53] Sun, C. M., Wu, C. L., Wang, C., Chang, C. I., Yip, M. C., & Fang, W. (2012). Implementation of complementary metaloxidesemiconductor microelectromechanical systems lorentz force two axis angular actuator. Japanese Journal of Applied Physics, 51(6S), 06FL09. Chicago

[54] Koester, D., Cowen, A., Mahadevan, R., Stonefield, M., & Hardy, B. (2003). PolyMUMPs design handbook. MEMSCAP Inc.

[55] Miyajima, H., Asaoka, N., Isokawa, T., Ogata, M., Aoki, Y., Imai, M., & Matsumoto, K. (2003). A MEMS electromagnetic optical scanner for a commercial confocal laser scanning microscope. Journal of Microelectromechanical Systems, 12(3), 243-251.

[56] Cho, I. J., Yun, K. S., Lee, H. K., Yoon, J. B., & Yoon, E. (2002, January). A low-voltage two-axis electromagnetically actuated micromirror with bulk silicon mirror plates and torsion bars. In Micro Electro Mechanical Systems, 2002. The Fifteenth IEEE International Conference on (pp. 540-543). IEEE. Chicago

[57] Cho, I. J., &Yoon, E. (2009). A low-voltage three-axis electromagnetically actuated micromirror for fine alignment among optical devices. Journal of Micromechanics and Microengineering, 19(8), 085007.

[58] Ahn, S. H., & Kim, Y. K. (2004). Silicon scanning mirror of two DOF with compensation current routing. Journal of Micromechanics and Microengineering, 14(11), 1455

[59] Lv, X., Wei, W., Mao, X., Yang, J., & Yang, F. (2015). A novel MEMS actuator with large lateral stroke driven by Lorentz force. Journal of Micromechanics and Microengineering, 25(2), 025009. Chicago.

[60] Pilkey, W. D. (1993). Formulas for stress, strain, and structural matrices. John Wiley & Sons, Inc.

[61] Bao, M., & Yang, H. (2007). Squeeze film air damping in MEMS. Sensors and Actuators A: Physical, 136(1), 3-27.

[62] Polytec Inc., OFV-5000 Vibrometer Controller user manual, www.polytec.com.

[63] Khater, M. E., Vummidi, K., Abdel-Rahman, E. M., Nayfeh, A. H., & Raman, S. (2011). Dynamic actuation methods for capacitive MEMS shunt switches. Journal of Micromechanics and Microengineering, 21(3), 035009.

[64] Nayfeh, A. H. (1983). The response of single degree of freedom systems with quadratic and cubic non-linearities to a subharmonic excitation. Journal of Sound and Vibration, 89(4), 457-470.

[65] Rebeiz, G. M. (2004). RF MEMS: theory, design, and technology. John Wiley & Sons.

[66] Moeenfard, H., Darvishian, A., & Ahmadian, M. T. (2013). A coupled bending-torsion model for electrostatically actuated torsional nano/micro-actuators with considering influence of van der Waals force. Acta Mechanica, 224(8), 1791-1800.

[67] Park, S., Al-Ghamdi, M. S., Khater, M., Abdel-Rahman, E., & Yavuz, M. (2014, August). Adjustable Sensitivity MEMS Magnetic Sensor. In ASME 2014 International

Design Engineering Technical Conferences and Computers and Information in Engineering Conference (pp. V004T09A016-V004T09A016). American Society of Mechanical Engineers.

[68] Sattler, R., Pltz, F., Fattinger, G., & Wachutka, G. (2002). Modeling of an electrostatic torsional actuator: demonstrated with an RF MEMS switch. Sensors and Actuators A: Physical, 97, 337-346.

[69] Alghamdi, M. (2015). Inertial MEMS Sensors.

[70] A. M. LLC, "Hall effect sensor," www.allegromicro.com/datasheets/A1360-1-2- Data sheet.pdf.